AD-A189 516 HIGH-TEMPERATURE METAL MATRIX COMPOSITES(U) CARNEGIE MELLON UNIV PITTSBURGH PA DEPT OF METALLURGICAL ENGI A W THOMPSON ET AL 30 NOV 87 AFOSR-TR-88-0089 1/2

UNCLASSIFIED F49620-87-C-0017 F/G 11/4 NL

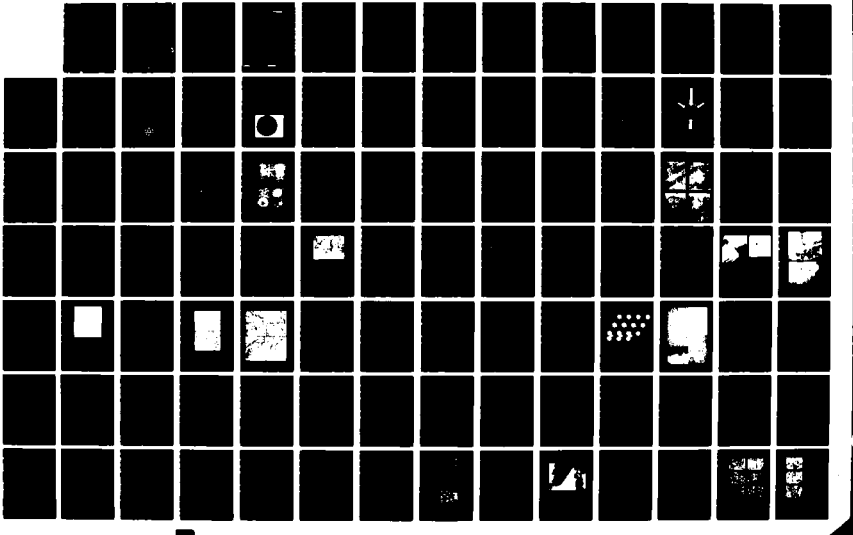

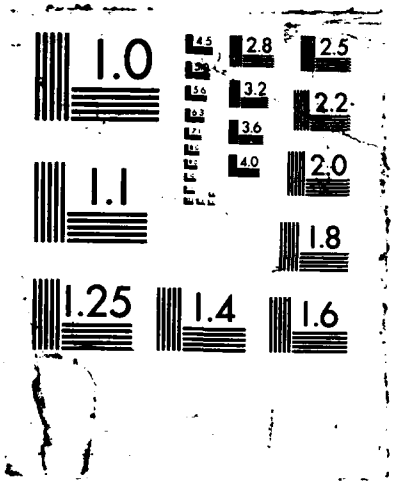
1.0
1.1
1.25
1.4
1.6
1.8
2.0
2.2
2.5
2.8
3.2
3.6
4.0
4.5

AFOSR-TR- 88-0089

HIGH-TEMPERATURE METAL MATRIX COMPOSITES

ANNUAL REPORT

AIR FORCE OFFICE OF SCIENTIFIC RESEARCH

Contract No. F49620-87-C-0017

November 15, 1986 - September 30, 1987

CARNEGIE MELLON UNIVERSITY

Pittsburgh, PA 15213

Principal Investigator, A. W. Thompson

and

University of California, Berkeley
Clemson University

November 30, 1987

HIGH-TEMPERATURE METAL MATRIX COMPOSITES

ANNUAL REPORT

AIR FORCE OFFICE OF SCIENTIFIC RESEARCH

Contract No. F49620-87-C-0017

November 15, 1986 - September 30, 1987

CARNEGIE MELLON UNIVERSITY

Pittsburgh, PA 15213

Principal Investigator, A. W. Thompson

and

University of California, Berkeley
Clemson University

November 30, 1987

SECURITY CLASSIFICATION OF THIS PAGE

REPORT DOCUMENTATION PAGE

1a. REPORT SECURITY CLASSIFICATION Unclassified	1b. RESTRICTIVE MARKINGS
2a. SECURITY CLASSIFICATION AUTHORITY	3. DISTRIBUTION / AVAILABILITY OF REPORT [redacted]ublic release, distribution unlimited
2b. DECLASSIFICATION / DOWNGRADING SCHEDULE	
4. PERFORMING ORGANIZATION REPORT NUMBER(S)	5. MONITORING ORGANIZATION REPORT NUMBER(S) AFOSR-TR- 88-0089
6a. NAME OF PERFORMING ORGANIZATION Dept. of Metallurgical Eng'g. and Materials Science 6b. OFFICE SYMBOL (If applicable)	7a. NAME OF MONITORING ORGANIZATION AFOSR
6c. ADDRESS (City, State, and ZIP Code) Carnegie Mellon University Pittsburgh, PA 15213	7b. ADDRESS (City, State, and ZIP Code) Bldg 410 Bolling AFB, DC 20332-6448
8a. NAME OF FUNDING / SPONSORING ORGANIZATION Air Force Office of Sci. Res. 8b. OFFICE SYMBOL (If applicable) NE	9. PROCUREMENT INSTRUMENT IDENTIFICATION NUMBER F49620-87-C-0017
8c. ADDRESS (City, State, and ZIP Code) Bldg 410 Bolling AFB, DC 20332-6448	10. SOURCE OF FUNDING NUMBERS PROGRAM ELEMENT NO. 61102F; PROJECT NO. 2306; TASK NO. A3; WORK UNIT ACCESSION NO.

11. TITLE (Include Security Classification)

High-temperature Metal Matrix Composites

12. PERSONAL AUTHOR(S)

A.W. Thompson and those listed in table of contents

13a. TYPE OF REPORT	13b. TIME COVERED	14. DATE OF REPORT (Year, Month, Day)	15. PAGE COUNT
Annual report	FROM 11-15-86 TO 9-30-87	1987 November 30	125

16. SUPPLEMENTARY NOTATION

17. COSATI CODES		
FIELD	GROUP	SUB-GROUP

18. SUBJECT TERMS (Continue on reverse if necessary and identify by block number)

High-temperature metal-matrix composites, interfaces, composite processing, aluminides, ~~Ti~~-aluminides, fatigue, creep, toughness, atomic resolution

19. ABSTRACT (Continue on reverse if necessary and identify by block number)

The Annual Report for Year 1 of the University Research Initiative grant at Carnegie Mellon University on High-temperature Metal Matrix Structural Composites contains sections on processing, characterization, and mechanical properties. These are further divided into reports from individual tasks on powder blending and consolidation, composite performance, structure and composition of composite interfaces, fatigue crack growth, creep, and fracture behavior.

20. DISTRIBUTION / AVAILABILITY OF ABSTRACT	21. ABSTRACT SECURITY CLASSIFICATION
☐ UNCLASSIFIED/UNLIMITED ☐ SAME AS RPT ☐ DTIC USERS	Unclassified
22a. NAME OF RESPONSIBLE INDIVIDUAL [redacted] Rosenstein	22b. TELEPHONE (Include Area Code) [redacted]767-4933
	22c. OFFICE SYMBOL NE

DD FORM 1473, 84 MAR 83 APR edition may be used until exhausted. All other editions are obsolete.

SECURITY CLASSIFICATION OF THIS PAGE

TABLE OF CONTENTS

SUMMARY

This first Annual Report for the University Research Initiative program at Carnegie Mellon University, including research efforts at Clemson University and the University of California (UC), Berkeley, contains summary reports from each of six task areas. These are listed below by Task title and Task Investigator(s). The individual sections in the body of the report follow in this same order. The tasks are additionally grouped as Processing (Tasks 1 and 2), Characterization (Task 3), and Mechanical Properties (Tasks 4, 5 and 6), with Task 2 being conducted at Clemson University and Task 4 at UC Berkeley.

Task 1. Experimental Study of Processing of Composites. H.R. Piehler, H. Henein.
Task 2. Modeling of Consolidation and Deformation Processing of Composites. H. J. Rack.
Task 3. Structure and Composition of Interfaces in Composites. J.M. Howe.
Task 4. Toughness and Fatigue of Metal Matrix Composites. R.O. Ritchie.
Task 5. Micromechanisms of High-temperature Composite Behavior. A.W. Thompson.
Task 6. Thermal and Mechanical History Effects on Composite Properties. W.M. Garrison.

The Processing area comprises two reports. Powder blending studies by Henein and Parent are addressing the problem of uniformity of blending, particularly in the presence of different shape and physical properties of constituent powders (e.g. matrix and reinforcement powders). This study includes development of models for the process. Preliminary indications are that the primary variables (for a rotary blender) will be rotational speed, particle size ratio, particle density ratio, and absolute (blender) drum size. The characteristics of the gas atmosphere inside the blender may also be of importance. Piehler's project, in coordination and conjunction with Henein's project comprising Task 1, has been preparing model composites to examine deformation processing effects. The cooperative research work being done in cooperation with Alcoa Laboratories is also a promising area. The development of an apparatus to combine multi-axial shear with hydrostatic compaction is near completion. The work by Rack emphasizes fiber-matrix interactions during processing, a potentially limiting factor in fiber-matrix compatibility, and also matrix behavior, especially precipitation and coarsening, during processing. For the former topic, surface modifications to the reinforcement phase(s) are being studied to increase compatibility for otherwise-promising systems. The latter topic addresses the well-known fact that aging kinetics are generally quite different in reinforced, compared to unreinforced, matrices. Understanding of both problems is essential for successful processing.

The single task on Characterization, by Howe, is using a combination of electron microscopy techniques to study composite interfaces. The techniques include analytical electron microscopy (AEM), high-voltage electron microscopy (HVEM), and atomic-resolution microscopy (ARM). Results to date have been accomplished for both aluminum-alloy matrices (as model systems) and for titanium aluminide matrices. The aluminum work has concentrated on the 2124 alloy matrix with SiC whisker reinforcement, in which interfacial structure and deformation behavior have beer studied, and on an 1100 alloy matrix with SiC whiskers, in which residual stress effects have been examined. Interfacial structure has also been studied in a Ti-48% Al alloy (called gamma) as a first step in understanding the matrix of aluminide composites. Additional work is underway in the Ti-24% Al-11% Nb alloy (called alpha-2), both with and without SiC fiber reinforcement.

In the Mechanical Properties area, Ritchie has examined the role of SiC particles in the growth of fatigue cracks in aluminum alloy-SiC composites. The role played by SiC depends on the scale of the particle size distribution. Coarse distributions, in particular, enhance crack growth resistance at low crack driving force by assisting development of crack closure. At high crack driving forces, however, composites exhibit more rapid fatigue cracking than do monolithic specimens of the matrix alloy. The studies of Thompson (with co-investigator Williams) are focussing on micromechanisms of creep, fatigue and creep rupture in metal matrix composites. It remains unclear whether the desirable properties of reinforcement-matrix bonds from the perspective of toughness and low-temperature ductility will be desirable under conditions of creep or

high-temperature deformation. This is particularly true if the existence of a "threshold stress" in creep is to be exploited in optimizing high-temperature properties. Garrison's work indicates that (as shown in a companion program sponsored by AFOSR) fracture in an aluminum-SiC composite can initiate by fracture of the SiC particles, and fracture can also initiate by cracking of grain boundaries near the SiC. However, the appearance of "interfacial" separation of SiC from the matrix actually occurs within the matrix near the SiC particle, not in the interface itself. This corresponds to a bond strength between reinforcement and matrix which exceeds the fracture strength of the composite.

STATEMENT OF WORK

The program in progress is an integrated study of composite materials having metal, ceramic or intermetallic matrices with particulate or fiber reinforcements, produced under controlled and understandable conditions, characterized in detail, emphasizing interface structure and composition, and with measurement and modeling of a broad range of mechanical properties, at ambient and elevated temperature.

- Task 1. Develop experimental capability with triaxial forging; conduct powder blending experiments and apply to compaction/forging experiments; determine experimental fiber rotation and breakage for comparison to Task 2 results; capture experimental understanding in frame-based expert system.

- Task 2. Conduct extension of existing finite element code to accommodate compaction of powder; include porous flow effects, friction effects, and fiber rotation and breakage; verify experimentally.

- Task 3. Characterize structure, composition, and bonding of interfaces between metal, ceramic, or intermetallic matrix and reinforcements, at ambient and elevated temperature, as functions of processing history from Tasks 1 and 2; determine residual stresses and deformation micromechanisms in composites.

- Task 4. Identify extrinsic toughening mechanisms in fatigue and fracture of composite materials, at ambient and elevated temperature; develop micromechanical models for intrinsic and extrinsic contributions to cracking resistance, in cooperation with Tasks 5 and 6.

- Task 5. Conduct creep, fatigue, stress rupture and creep-fatigue evaluations on metal and intermetallic matrix composites, under conditions of varying stress, strain amplitude and temperature; identify micromechanisms of failure; integrate results into behavior models with Tasks 4 and 6.

- Task 6. Examine effects of thermal and mechanical history on mechanical performance of metal and intermetallic matrix composites, through testing at varying temperature and service stress conditions; characterize micromechanisms of deformation and fracture as a function of exposure history; develop model descriptions of performance with Tasks 4 and 5.

In addition to these task-specific efforts, there will be several other objectives of work which involve integration among tasks. Some are shown above explicitly; others are listed below.

- Determine interrelationships among composite processing parameters, composite microstructure (including interfacial characteristics), and mechanical behavior, at ambient and elevated temperature (all tasks).

- Identify and model fundamental micromechanisms of mechanical behavior, at ambient and elevated temperature, in composite materials (Tasks 4-6).

SECTION 1

PROCESSING

TASK 1 : Powder Blending

Blending Issues in Metal-Matrix Composite Formation

J.O. Gerald Parent and Hani Henein

Introduction

The processing history of a composite will have a significant effect on the final properties of the material. One aspect of the powder processing route involves blending of the metal matrix and reinforcement powders prior to the consolidation step. The ideal blending step would result in an even distribution of the reinforcement material throughout the metal powder mass, as well as the means to maintain this distribution into the consolidation operation. To date, however, the mechanisms governing the blending of fine powders, especially where significant differences in material properties between the constituent powders exist, have not been closely examined. In order to be able to achieve a reproducible blend of the powders, the conditions under which proper blending occur must be fully understood.

The aim of this research, then, is to provide a fundamental understanding of the factors governing the quality of a blended powder mass. The operating conditions for a rotary mixer which lead to the best final product will be established, as well as the detailed reasons for which changes in these conditions bring about changes in the final outcome. Efforts at providing models for the process will also be pursued, with the goal of providing a means by which the operating conditions of large units may be predetermined to provide for the best blend prior to compaction.

Previous Work

Both axial and radial segregation have been shown to occur during the operation of rotary mixers [1-3]. Studies of these phenomena have primarily been performed with large particulate systems, and the specific case of segregation in powders has generally been neglected. These large scale studies have, however, provided an indication of the factors which are of importance in determining the segregative behavior of a particulate bed during rotary motion. These are:

Rotational Speed - Changes in the rotational speed will cause variations in the ratio of the centrifugal to gravitational forces experienced by the particulate bed. Depending on the specific value of the ratio and the bed motion at a specific rotational speed, segregation may either be enhanced or minimized. Within the regime of speed where segregation is observed, the rate of segregation increases with an increase in rotational speed.

Size ratio - Increases in the difference between the particle size will enhance segregation. There appears to be a minimum size difference for segregation to occur, however. For a ratio of value less than 1.2, the particles can essentially be considered to be of the same size and thus segregation does not occur. Beyond this value, however, the smaller particles can fit into the voids between the larger ones and segregation can proceed. For typical metal-matrix/ceramic reinforcement combinations (130 μm metal, 35 μm ceramic) the size ratio is in the range of 3.5:1, thus segregation would be expected to occur.

Particle density ratio - In this case the denser particles, due to the higher gravitational forces they experience, can force their way between the less dense material,

forming a segregated region much in the same way as in the case of extreme size differences. Evidence exists that indicates that this effect is secondary when size diferences exist. For a typical titanium/ceramic system (ρ_{metal} = 4.5 - 4.7 g/cm3, $\rho_{ceramic}$ = 3.2 g/cm3) the density ratio is of the order of 1.5:1. This suggests that the size difference between the powder will be of greater importance than the density differences.

Absolute drum size - Larger drum sizes result in increases in the ratio of the centrifugal to the rotational forces, causing an increase in the rates of segregation observed.

For the specific case of powder blending, these effects have also been observed, although the mixing considered has been solely that of monosized, differently colored particles. In addition to these, recent investigations [4,5] have shown that the gas atmosphere present within the drum can drastically affect the mixing experienced by the powder mass. An equation for determining whether the gas will have any effect on the mixing has been developed, given by

$$N_g = \frac{\rho_d d_p^2 g}{\mu U_A}$$

where N_g = gas particle interaction number, ρ_d = particle density, d_p = mean particle size, g = acceleration due to gravity, μ = gas viscosity and U_A = typical operational speed. For values of N_g << 100, the gas atmosphere will have a significant effect on the character of the bed depth and its flow characteristics. It can be seen from the form of the equation that the gas interaction number is affected by a variety of parameters, notably the speed of the drum, the gas viscosity and, related to the viscosity, the gas pressure. Values of N_g for a variety of gas viscosities and particle diameter size are shown in the plot below.

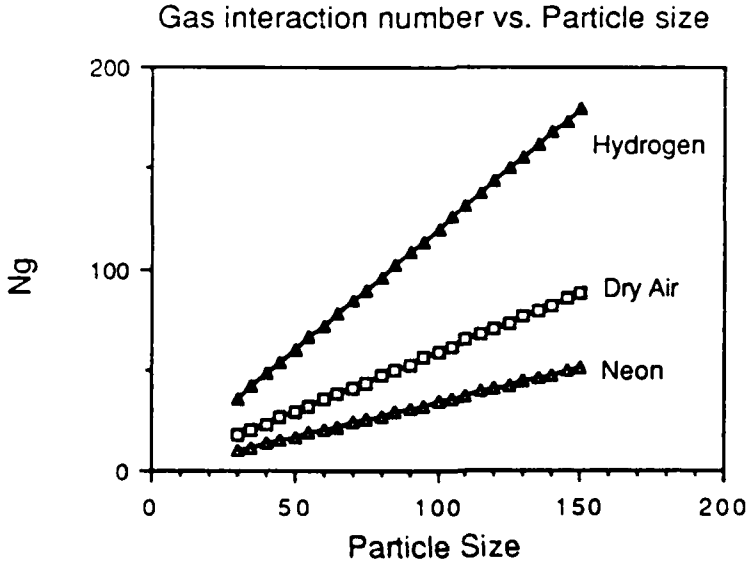

For high values of U_A, μ and gas pressure, the powder bed becomes fluidized and flows very easily. This improves mixing and therefore raises the potential for serious problems with segregation. Conversely, low values for these variables results in a very static powder mass, which may be beneficial in minimizing segregation.

An additional factor to be considered is the interaction between the particles as a result of electrostatic attraction and van der Waals forces. In the case of the metal particles, due to their relatively large size, it seems likely that these forces will be less important than those interactions promoted by the gas atmosphere. For the ceramic powders, however, the possibility for attraction exists and in the case where clustering occurs, the ideal distribution will not be achieved.

Obviously, the exact nature of the relationship between these parameters for the particular case of interest is one which remains undefined. If the production of a consistently well-blended precursor is to be achieved, the interaction of these various effects must be completely understood.

Experimental Design and Projected Timetable

At present, the precise nature of the experiments to be conducted has not been established. There remains some concern as to the exact means by which a good mixture may be quantified in the case of fine powders. Initial experiments will therefore be conducted in order to establish the best means for characterizing the mixture. Traditional methods of mixture analysis have relied on sampling of the bed using some type of thief, although this raises questions regarding the representative nature of the sampling technique. Also, it is unclear as to whether or not the bed is significantly disturbed upon insertion of the thief. Some visual observations at the onset, possibly combined with high-speed photography techniques, may help to identify the best means for bed characterization. In addition, these preliminary studies will help to identify which of the variables mentioned in the previous section are of greatest importance in determining the quality of the mixture. With these ideas in mind, the program of study can then be specifically designed.

The equipment is thus being designed with the following broad goals:

- Cylinders will be built with three separate i.d's, with removable liners to facilitate the installation of modifications to the internal cross-section (lifters).
- Variable and controllable speed for the rotating cylinders.
- Variable gas atmosphere in the cylinder, controlled during the actual runs. Both the type of gas and the operating pressure will be changeable.
- Interchangeable clear and solid end-plates will be provided for all drum sizes to allow for visual examination of the blending process as well as a variety of sampling schemes.

The actual studies in this task will likely not begin before the new year. This is to allow time for completion of the design of the blender as well as the literature review and preliminary experiments. A reasonable timetable for the period remaining in this calendar year is presented below.

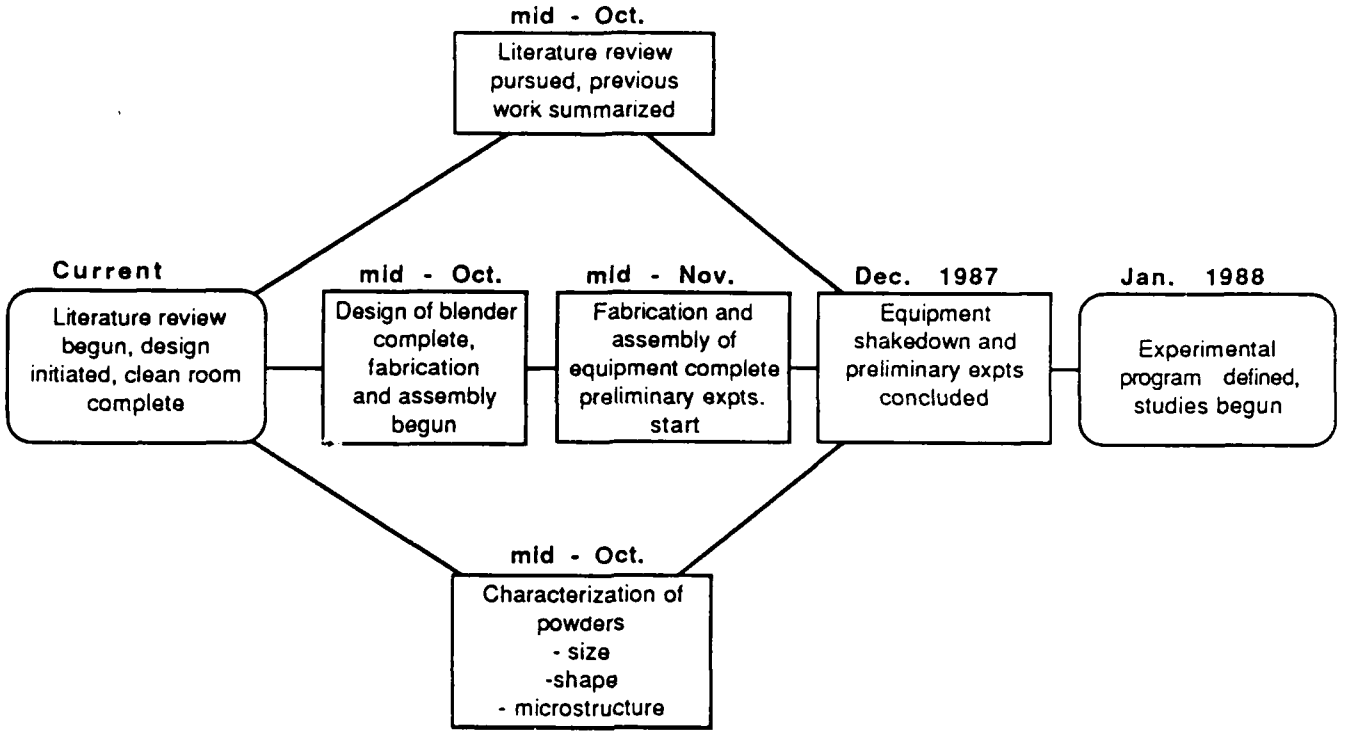

Materials and Equipment

The following is a list of the resources expected to be required for the project. Items in italics are those which have yet to be acquired or built.

Clean Room (contents are included in the specific descriptions below)

Particle characterization
- standard sieves plus RoTap sieve shaker
- Microtrac® particle size analyzer
- microdensitometer (image analysis system)
- riffler (sample separation for size analysis)
- optical and electron microscopy facilities

Blending unit
- *rotary design - three separate i.d.'s*
- *atmosphere control (pressure and type, during experimental run)*
- variable speed motor
- *removable inserts (lifter modifications)*

Powder materials
- Ti-6Al-4V, mostly tank sweepings (-35 mesh)
- some other alloys, strain-energized materials
- *reinforcements*
- *titanium aluminides*

References

1. Henein H., Brimacombe J.K. and Watkinson A.P., *Met Trans. B*, 16B (1985), pp. 763-774

2. Nityanand N., Manley B. and Henein H., *Met Trans B*, 17B (1986), pp. 247-257

3. Roseman B. and Donald M.B., *Brit. Chem. Eng.*, 7(11) (1962), pp. 823-827

4. Rietema K., *Powder Technology*, 37 (1984), pp. 5-23

5. Cottaar W., Heynen A. and Rietema K., *Powder Technology*, 46 (1986), pp. 219-225

First-Year Progress Report for the Project

Deformation Processing of Composites

Henry R. Piehler
Daniel M. Watkins

Deformation Processing Laboratory
Department of Metallurgical Engineering & Materials Science
Carnegie Mellon University
Pittsburgh, Pennsylvania 152213-3890

Introduction

This project is designed to develop a fundamental understanding of the deformation processing of short-fiber reinforced composites for high temperature applications. This fundamental knowledge of composite deformation processing will enhance the selection, fabrication, and performance of these materials and provide a link between two other projects in this initiative: the blending research at Carnegie Mellon and the continuum mechanics based research at Clemson.

The basic methodology used in the present study is illustrated schematically in Figure 1 below.

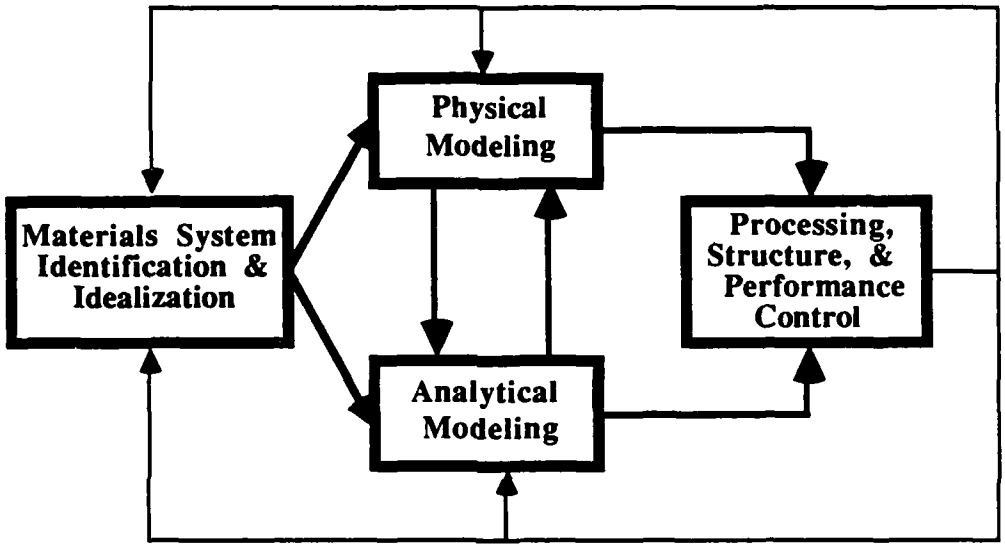

Figure 1.
Methodology Used in Deformation Processing of Composites

The ultimate goal is to achieve deformation processing, structure, and performance control for short-fiber high temperature composites. This goal is being accomplished by a synergistic use of physical and analytical modeling of simple composite geometries that capture the essential features of the composite systems of interest.

The composite geometry used most extensively to date is the seven-filament configuration shown in Figure 2 below.

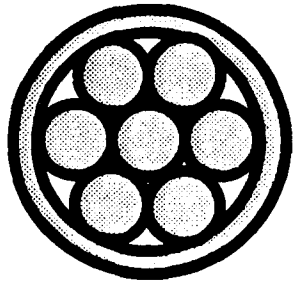

Figure 2.
Basic Geometry Used in Compaction Studies: Seven Filaments Encapsulated in a Cylinder

This fundamental geometry has been used successfully in the past to predict the experimentally observed onset of instability in a continuous, metal-metal composite given the volume fractions and the uniform elongations of the filaments and matrix [1,2]. The seven-filament array can also be fabricated using filaments of differing materials or reinforcement fibers. For example, this seven-filament array can be used to address a fundamental issue in hot isostatic compaction of powders: the relative contributions of deformation and diffusional processes to densification and their subsequent effect on properties. The basic assumption is that consolidation by deformation would scale with filament diameter while consolidation by diffusional processes clearly would not. Hence HIPing seven-filament arrays of varying filament diameters should provide direct evidence of the relative roles of deformation and diffusional processes operative during consolidation. Observations from physical modeling will also provide valuable insights to direct the development of an analytical model. This will further enhance our predictive undertanding the operation and consequences of the HIPing process beyond that provided by Ashby [3]. Furthermore, the densified seven-filament samples provide for a convenient assessment of the influences of the various compaction mechanisms on the resultant mechanical properties of the compact. For example, the integrity of the interfaces produced by HIPing can be conveniently evaluated using torsion tests on the compacted samples.

The use of pure isostatic compaction to study the deformation processing of composites is severely limited in comparison to most commercially viable deformation processes (e.g., extrusion) which involve a shear or deviatoric stress in addition to a hydrostatic component. This deficiency associated with pure isostatic compaction has been previously addressed by Koerner [4] in his studies of the cold compaction of metal powders. Koerner developed and used a triaxial compaction apparatus similar to that used in soil mechanics testing. The triaxial stress states and processing paths identified by Koerner are shown schematically in Figure 3.

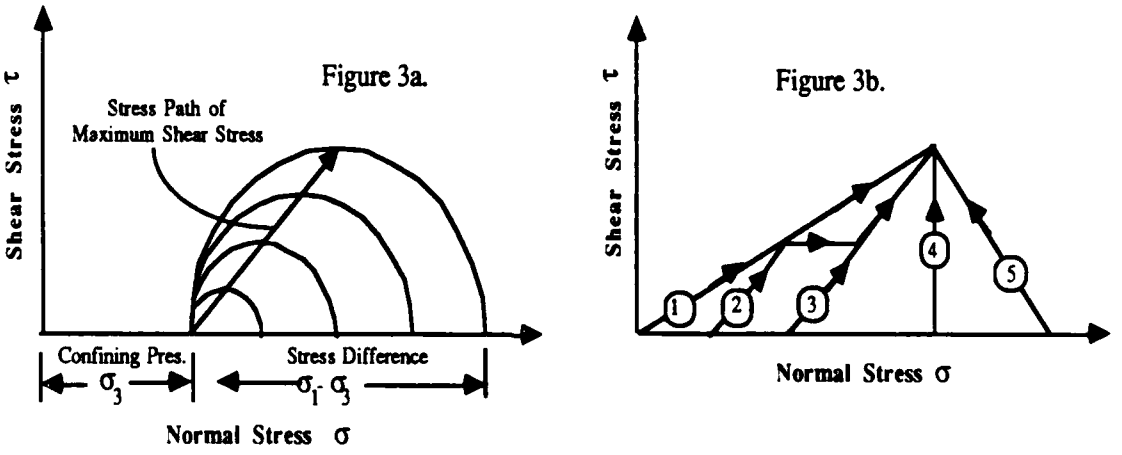

Figure 3.
Triaxial Stress States and Deformation Paths used by Koerner [4].
(Compression is positive.)

A shear stress is induced whenever the axial stress, σ_1, is different from the confining (or isostatic) pressure, σ_3. Figure 3b. illustrates different paths to arrive at the same

final combination of shear stress and isostatic pressure. Koerner's apparatus is shown schematically in Figure A-5 (Figure 5 in Appendix A). Two of Koerner's significant findings are shown in Figure A-7. The first is that, at a constant level of compacted density, the tranverse rupture strength after compaction increases with the level of shear stress imposed during compaction. The second is that, for a constant hydrostatic component of stress, increasing the level of shear superimposed during compaction increases the level of density achieved. These results are consistent with the recent sinterforging experiments of Raj [5], who also imposed a triaxial stress during compaction but was unable to control the levels of shear and hydrostatic stress independently. (See Figures A-10) Another important of Raj's results is that the bulk densification behavior of the composite matrix can be altered by the presence of the reinforcing constituents (Figure A-10). These reinforcement-induced changes in the nature of the matrix consolidation can also be conveniently studied using the seven-filament configuration described previously and the hot triaxial compaction apparatus described in the next section.

Progress to Date

The two principal areas of progress to date are: 1) the use of the seven-filament geometry to study the hot isostatic compaction of pure aluminum and Ti-6Al-4V filaments of varying diameters and 2) the design of a hot triaxial compaction unit.

The initial studies of HIPing seven-filament arrays of Aluminum wires have been completed and the results published [6]. Our principal finding, as expected, is that densification at constant temperature and pressure is a function of filament diameter. Some preliminary results from this study are shown in Figure A-16. Because of surface oxidation problems associated with Al and a declining interest in its use as a matrix material, subsequent consolidation efforts involved Ti-6Al-4V filaments. A preliminary result from these latest HIPing studies is shown in Figure 4.

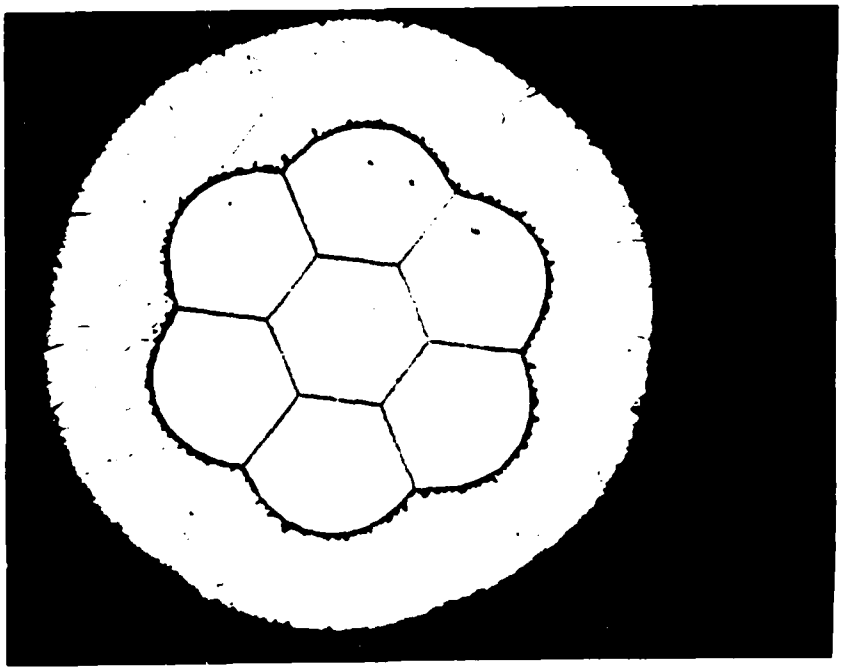

Figure 4.
Hot Isostatically Compacted Ti-6Al-4V Seven-Filament Array (64x)

These Ti-6Al-4V filaments were compacted in a CP titanium tube at 750° C and a pressure of 15,000 psi. The difference in flow stress of the Ti-6Al-4V filaments and the CP titanium tube is apparent in Figure 1a. The boundaries touching the central filament are all straight while the boundaries at the outer CP Ti interface remained essentially circular. A second set of HIPing experiments has just been completed using Ti-6Al-4V filaments of various diameters, some of which contained SiC fibers in their intersticies. (SCS-6 fibers obtained from Avco.) All HIPing in this project to date has been done at the Alcoa Research Laboratories, who have graciously made their HIPing equipment available to us prior to the completion of the hot triaxial compaction apparatus described below.

The triaxial stress/temperature paths attainable using hot triaxial compaction are illustrated schematically in Figure 5 below.

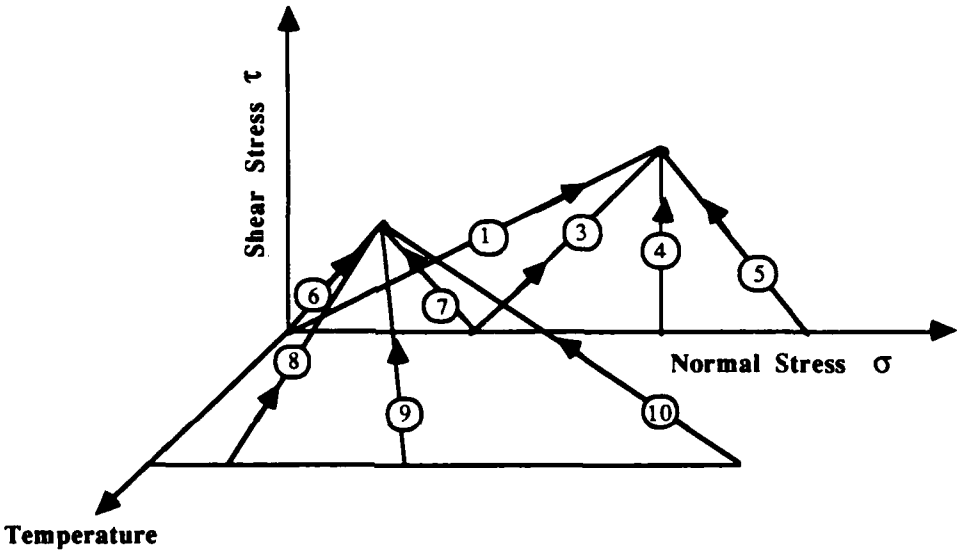

Figure 5.
Triaxial Stress/Temperature Paths Obtainable Using Hot Triaxial Compaction

Processing paths 1-5 are those identified by Koerner and illustrated in Figure 3b. Paths 6-10 involve coupling between shear stress, normal stress, and temperature and can only be imposed using an apparatus such as we have developed.

The acronym for our MultiAxial Shear + Hydrostatic CompactER is **M*A*S+H*E*R I**. This apparatus was designed together with personnel from Conaway, Inc., who are fabricating the equipment. The basic HIPing unit is already completed and the triaxial force module will be completed in March. Schematic drawings of this unit, which also has the capability of superimposing a tensile force during compaction, are shown in Figures A 12-14. The basic unit has the capability of rapid pressurization to 60,000 psi and can attain a temperature of 2000° C. The limits under triaxial conditions are an axial compressive force of 10,000 lb, an axial tensile force of 5,000 lb, and a maximum operating temperature of 1200° C. In the study the fundamentals of deformation processsing of composites, this equipment offers unique capabilities which are available nowhere else in the world.

Future Research Plans

We plan to continue our compaction studies of seven-filament arrays of Ti-6Al-4V and SiC using both HIPing and hot triaxial compaction. We have also located a source for Ti_3Al fibers and plan to use these in our seven-filament studies as well, both monolithically and in combination with SiC (SCS-6) fibers. The next year will largely be devoted to scoping experiments using these materials, both to provide insights into the relationship between composite processing and performance and to provide guidance for developing continuum models for these deformation processes and perhaps for the performance of the compacted samples as well. Room temperature torsion testing will be the primary mode of initial performance evaluation. Deformed and undeformed samples will also be made available for high resolution TEM interface studies (Howe).We plan to conduct our modeling efforts in cooperation with the Alcoa Research Laboratories. The first analytical modeling goal will be to develop an accurate predictive capability for the shape of the seven-filament pore geometry as a function of degree of densification by deformation only. This will be the first step in isolating and characterizing the contributions to densification by deformation as separate from diffusional processes.

We will also initiate experimental and theoretical studies of fiber orientation during and after consolidation. Model systems containing two filaments of different preselected spatial orientations in powder matrices will be subject to a range of stress states and consolidation parameters. Guidance for the selection of representative two-filament orientations will hopefully be forthcoming from the mixing studies at Carnegie Mellon (Henein). The two-filament compaction data and models, plus any deformation-induced damage associated with particular two-filament configurations and triaxial stress/temperature paths, will also provide information for the continuum-based forging models being developed at Clemson (Rack). Candidate materials for this two-filament study include SiC fibers and Ti-6Al-4V powders.

While considerable effort will be expended on these seven-filament and two-filament/powder matrix controlled consolidation studies, substantial efforts will focus on upgrading control system software tto achieve the maximum operational capabilities of **M*A*S+H*E*R I**. As a result, this equipment will not only continue to be an vital piece of apparatus in this project but will also be equally valuable in other research and educational activities.

References

1. Piehler, H.R., "Plastic Deformation and Failure of Silver-Steel Filamentry Composites,"Trans. TMS-AIME, Vol. 233, pp 12-16, 1965.

2. Garmong, G. and R.B. Thompson, "A Theory for the Mechanical Properties of Metal-Matrix Composites at Ultimate Loading," Met. Trans., Vol. 4, pp 863-873, 1973.

3. Helle, A.S., Easterling, K.E., and Ashby, M.F., "Hot Isostatic Pressing Diagrams: New Developments," Acta Metal., Vol. 33, No. 12, pp 2163-2174, 1985.

4. Koerner, R.M., "Triaxial Stress State Compaction of Powders," Powder Metallurgy Processing, New Techniques and Applications, H.A. Kuhn and A. Lawley, ed., Academic Press, N.Y., pp.33-50, 1978.

5. Raj, R., "Enhancement of Strength through Sinter Forging," J. Am. Ceram. Soc., 70 [7], pp 514-520, 1987.

6. Yoshida, K., Steyer, T.E., Watkins, D., Piehler H., "HIP Consolidation of Seven Filament Arrays of Aluminum Wires," Physical Modeling of Metalworking Processes," Editors: Erman, E. and Semiatin, S.L., TMS Publications, 1987.

APPENDIX A

Deformation Processing of Composites

Henry R. Piehler

J. O. Gérald Parent, Graduate Student

Daniel M. Watkins, Graduate Student

Todd E. Steyer, Senior Undergaduate Student

Michael Khuni, Technician

October 9, 1987

Figure A-1

OUTLINE OF PRESENTATION

- RATIONALE FOR PROJECT METHODOLOGY

  Selection of Model Geometries

  Design of Deformation Processing Equipment

- SUMMARY OF RESULTS TO DATE

  Shear + Hydrostatic Compaction (Koerner, Raj)

  HIP Consolidation of 7-Filament Al Arrays

- COMBINED SHEAR+HYDROSTATIC COMPACTER

- FUTURE EFFORTS

- RELATED STUDIES

Figure A-2

METHODOLOGY USED IN DEFORMATION PROCESSING STUDIES

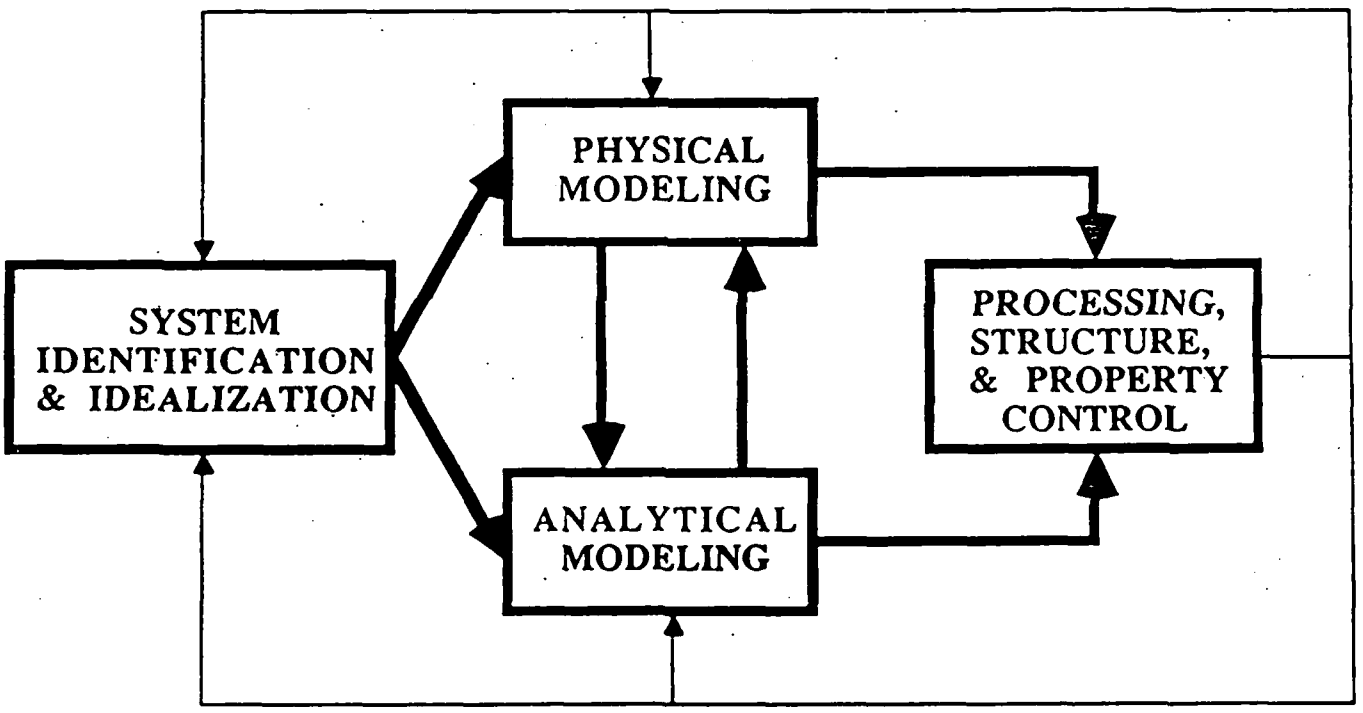

Figure A-3

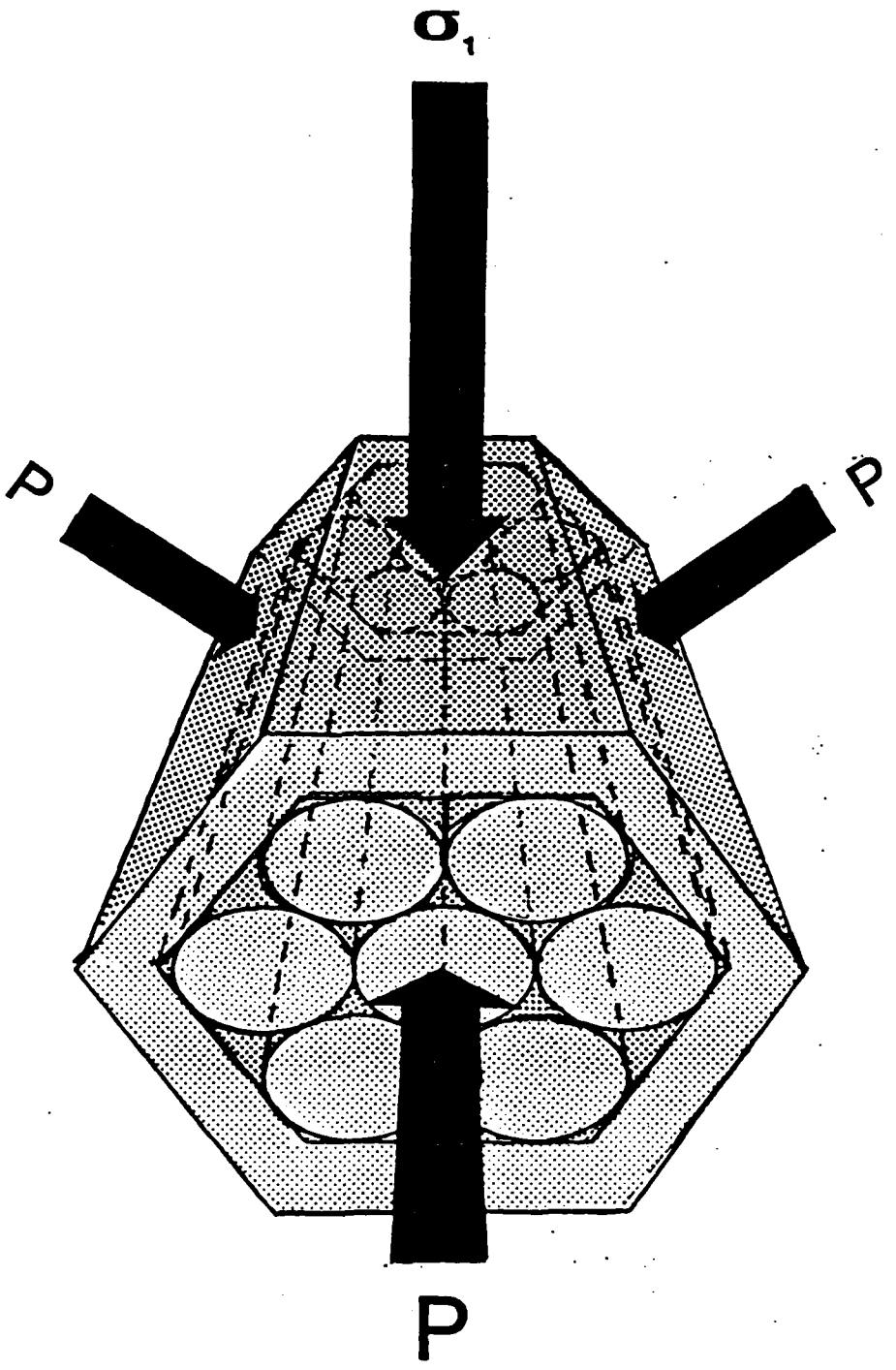

Figure A-4

DEFORMATION PROCESSING CONDITIONS

- **Elevated Temperatures**
- **High Strain Rates**
- **Multiaxial Stress and Strain States**
- **Spatial Stress and Strain Gradients**

Figure A-5

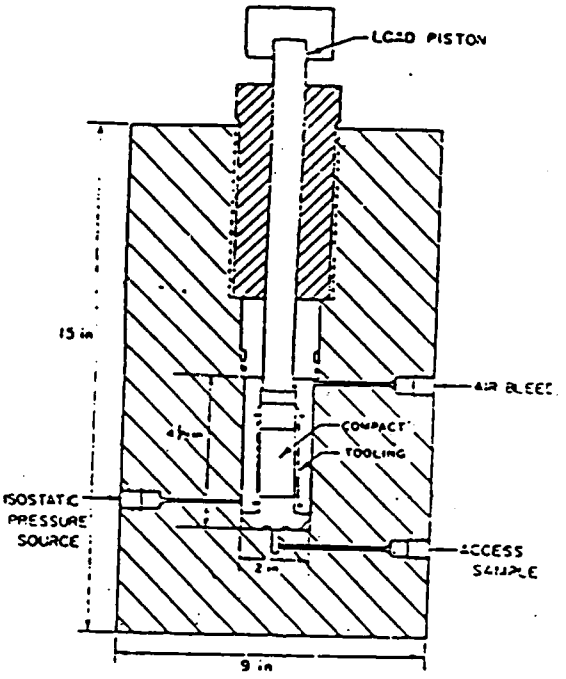

Triaxial Compaction Unit (Koerner)

Figure A-6

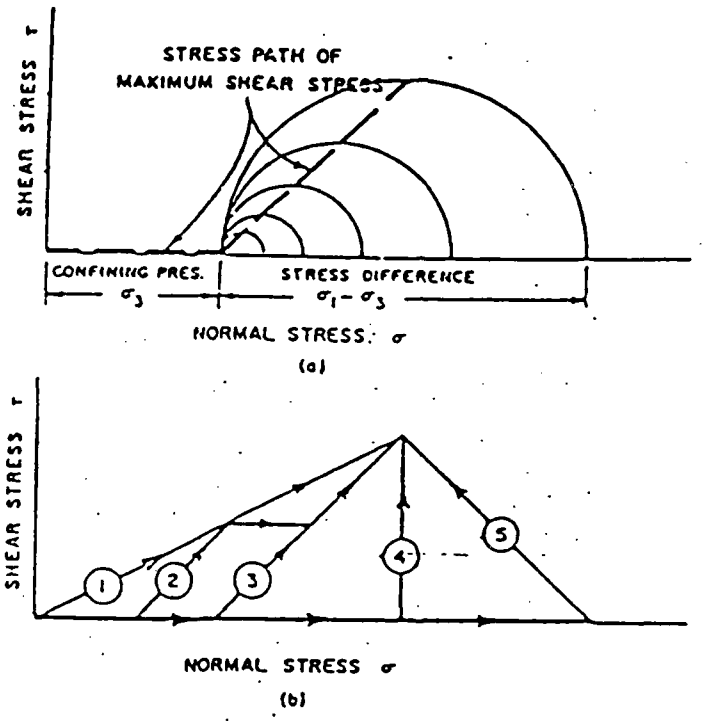

Triaxial Stress Paths as Outlined by Koerner

Figure A-7

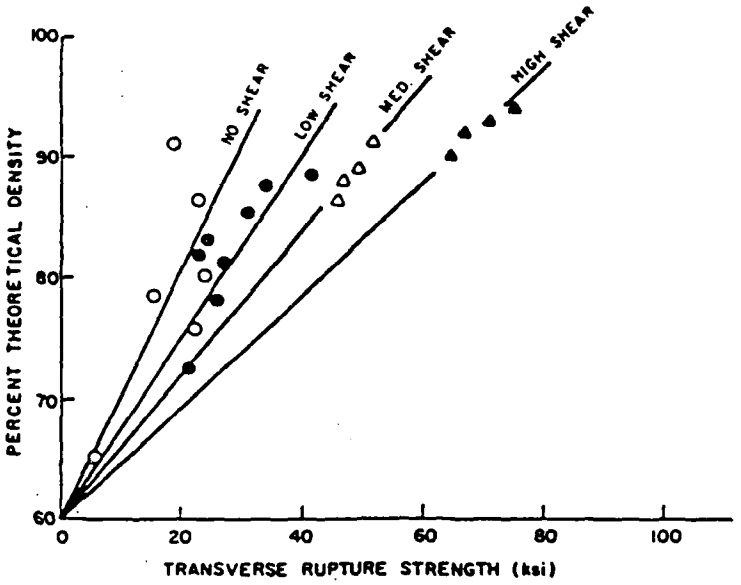

Fig. 10 Density versus transverse rupture strength for isostatically and triaxially compacted iron powder compacts showing the influence of shear stress: ○, no shear (isostatic); ●, low shear (0–17 ksi); △, medium shear (17–24 ksi); ▲, high shear (34–50 ksi). (1 ksi = 6.9 MPa.)

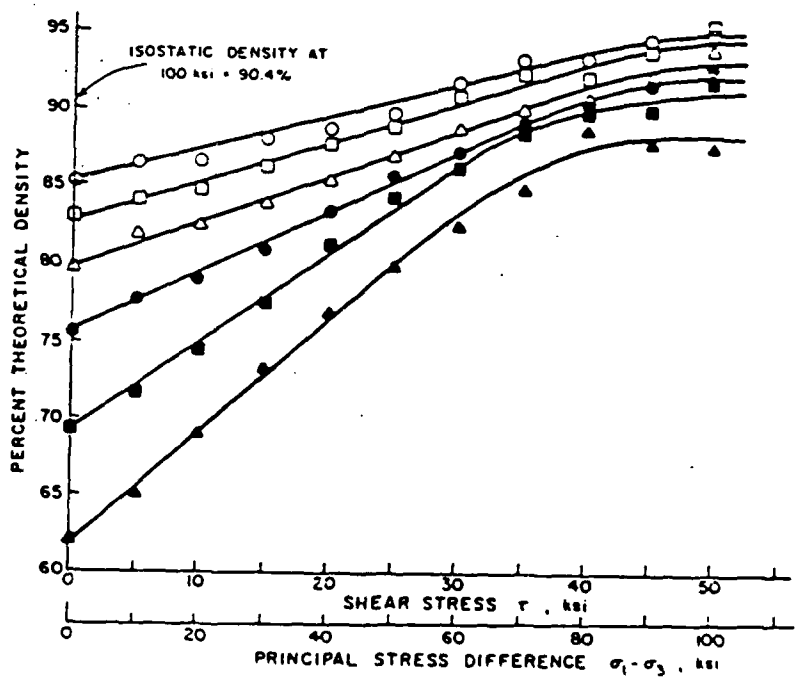

Fig. 7 Triaxial compaction response curves showing density increase under increasing shear stresses at various confining pressures. Confining pressure (ksi). ○, 60; □, 50; △, 40; ●, 30; ■, 20; ▲, 12. (1 ksi = 6.9 MPa.)

Koerner's Results

Figure A-8

D-337

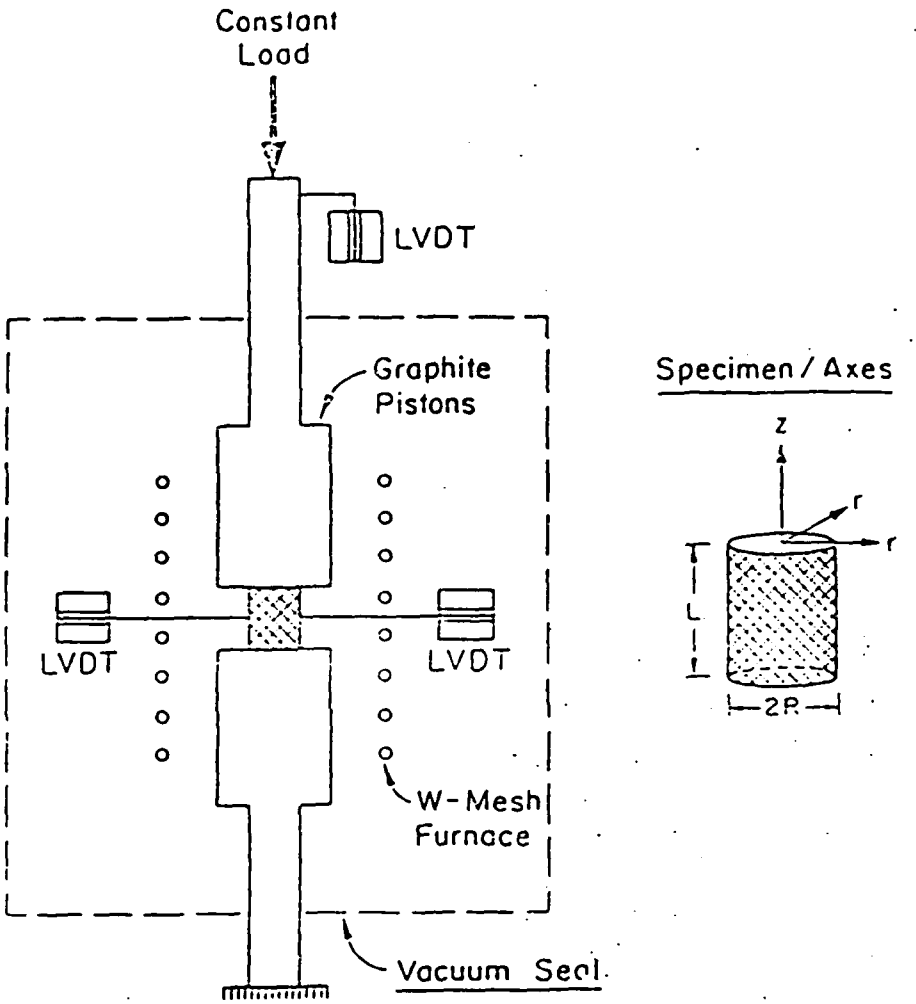

Fig. 1 A schematic of the apparatus used in the sinter forging experiments. The radial strain was obtained from the average measurement from the two transverse LVDTs. The load was applied axially. The third LVDT provided the axial strain.

Figure A-9

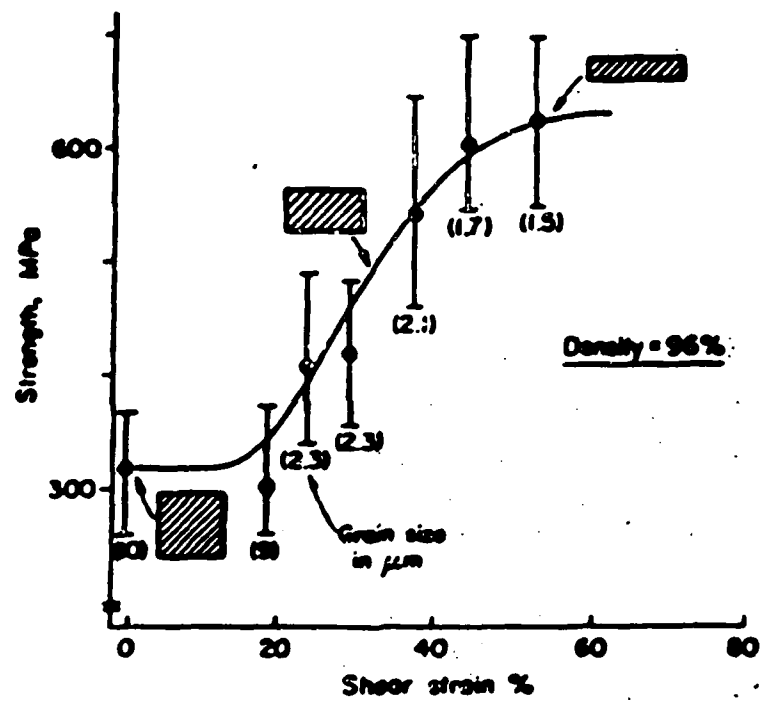

Fig. 5. Influence of shear strain on strength of sinter-forged and free-sintered alumina. All specimens had the same final density (96%) but had been subjected to different amounts of shear strain.

Figure A-10

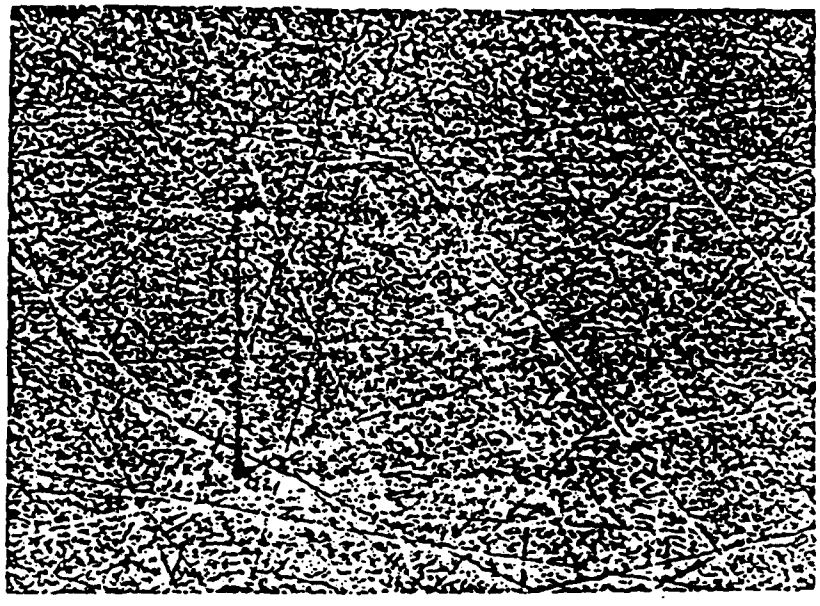

(a)

10.0μm

(b)

Fig #9

Secondary Electron Micrograph of Polished Unetched Sections. (a) Pure TiO_2. (b) Composite with .03 volume fraction Al_2O_3 agglomerates. Both sintered at 1273K for 200 minutes. Note the dramatic effect of even a small fraction of non densifying phase on the densification behavior.

Figure A-11

MultiAxial Shear + Hydrostatic compactER I

M*A*S+H*E*R I

Figure 4-12

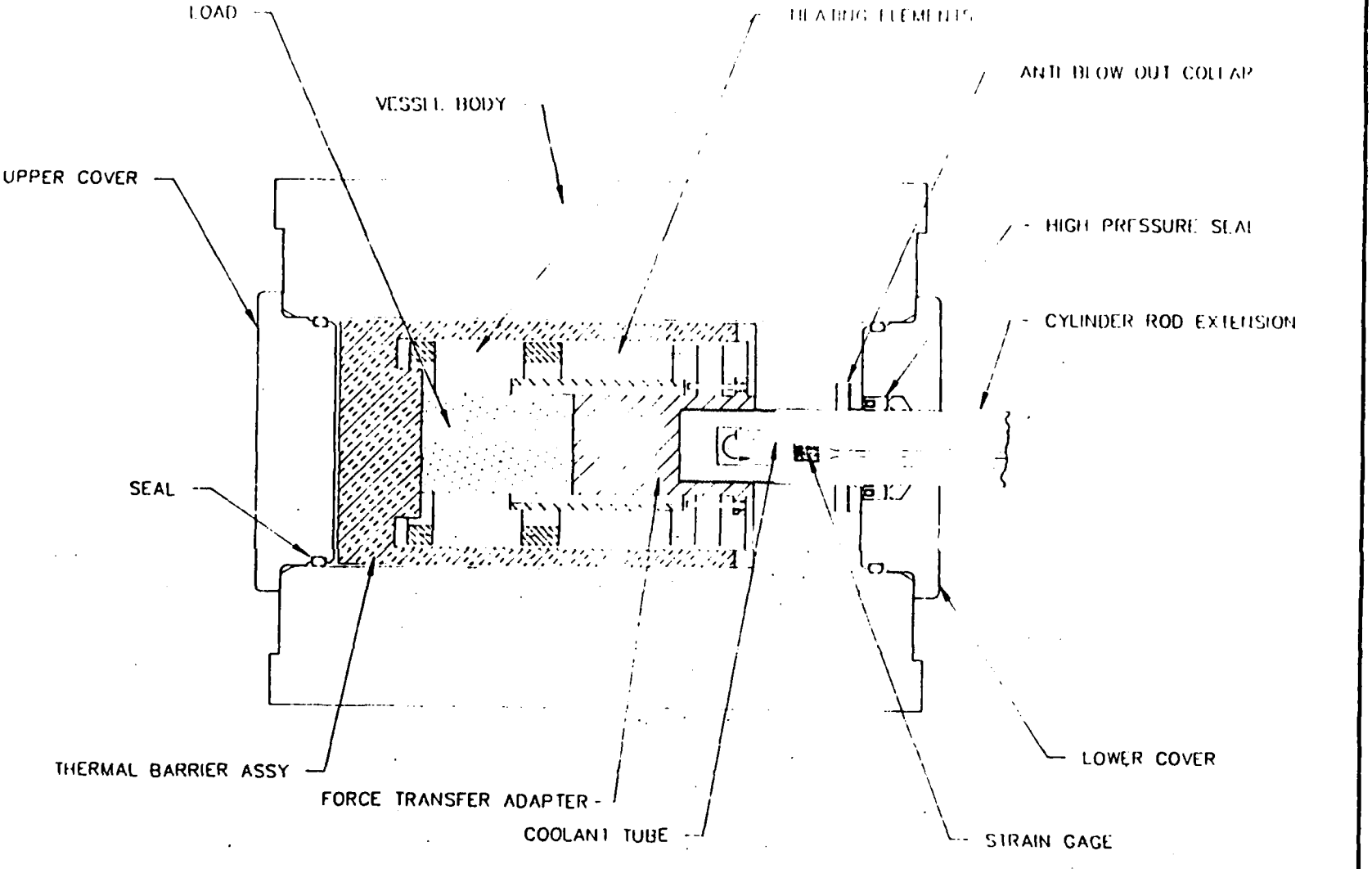
LOAD
HEATING ELEMENTS
ANTI BLOW OUT COLLAR
VESSEL BODY
UPPER COVER
HIGH PRESSURE SEAL
CYLINDER ROD EXTENSION
SEAL
THERMAL BARRIER ASSY
FORCE TRANSFER ADAPTER
COOLANT TUBE
LOWER COVER
STRAIN GAGE
TITLE
FURNACE ASSEMBLY

Figure A-13

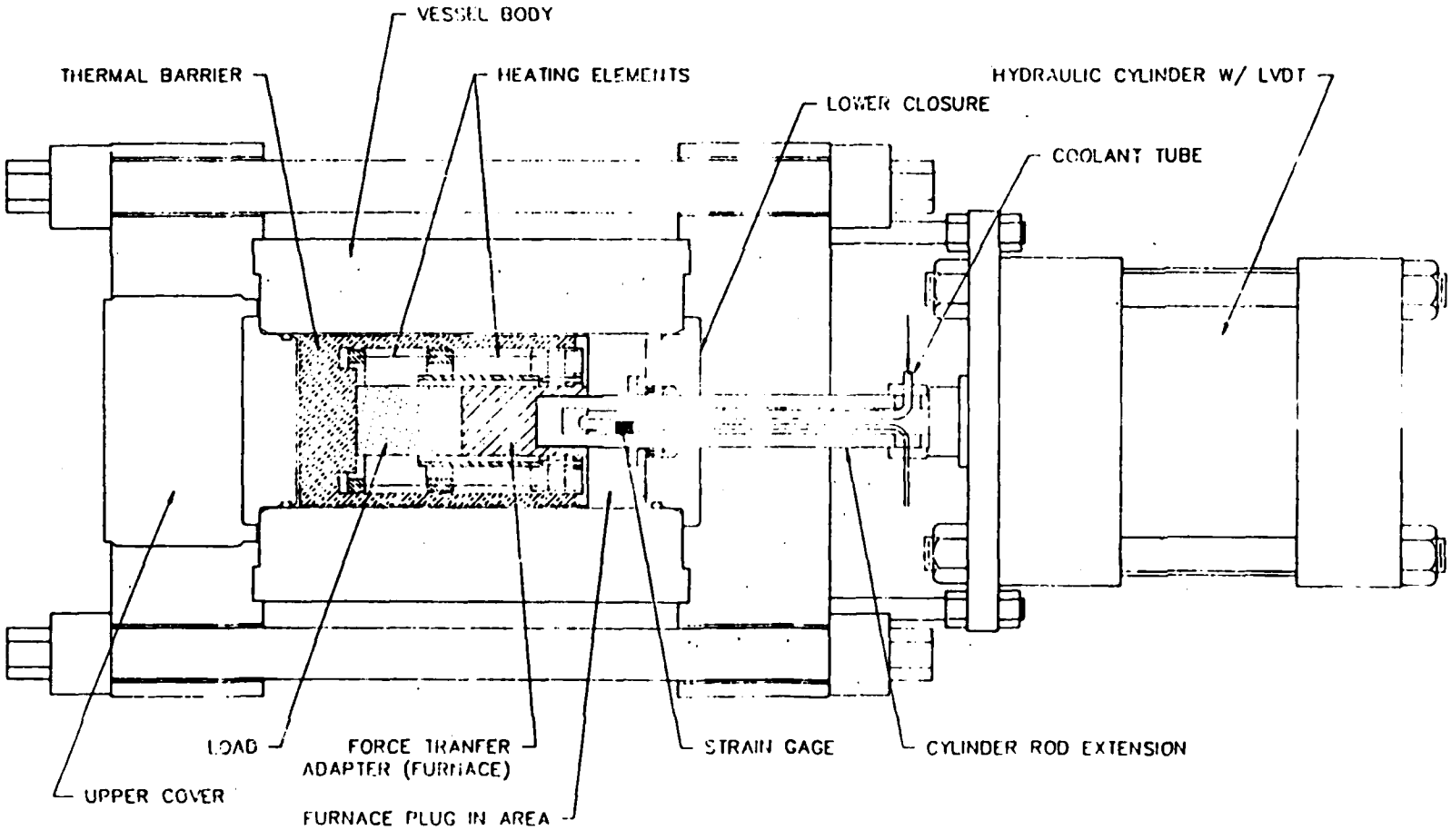
VESSEL BODY
THERMAL BARRIER
HEATING ELEMENTS
HYDRAULIC CYLINDER W/ LVDT
LOWER CLOSURE
COOLANT TUBE
LOAD
FORCE TRANFER ADAPTER (FURNACE)
STRAIN GAGE
CYLINDER ROD EXTENSION
UPPER COVER
FURNACE PLUG IN AREA

Figure A-14

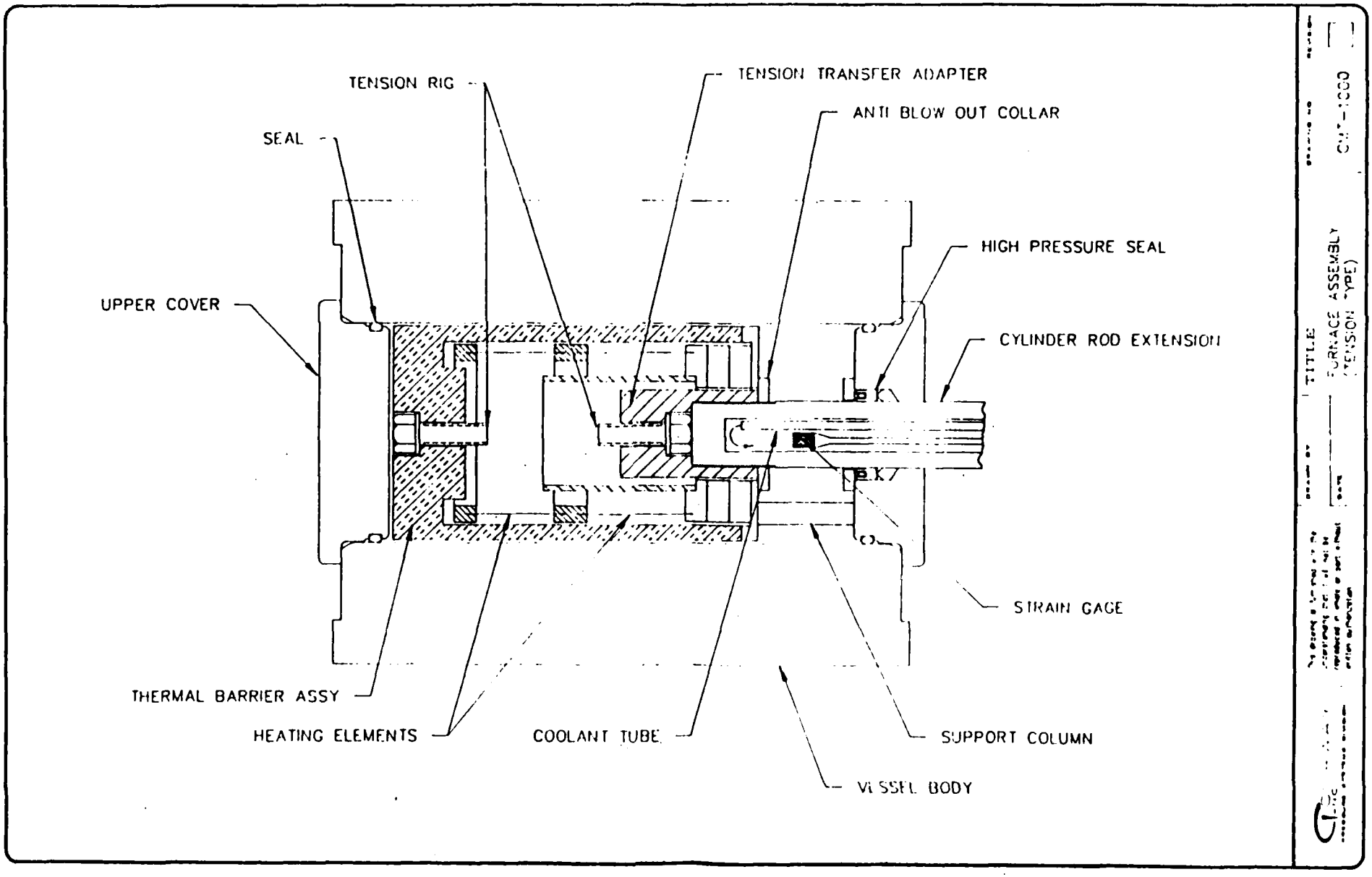
TENSION RIG
TENSION TRANSFER ADAPTER
ANTI BLOW OUT COLLAR
SEAL
HIGH PRESSURE SEAL
UPPER COVER
CYLINDER ROD EXTENSION
STRAIN GAGE
THERMAL BARRIER ASSY
HEATING ELEMENTS
COOLANT TUBE
SUPPORT COLUMN
VESSEL BODY
TITLE
FURNACE ASSEMBLY
(EXTENSION TYPE)

Figure A-15

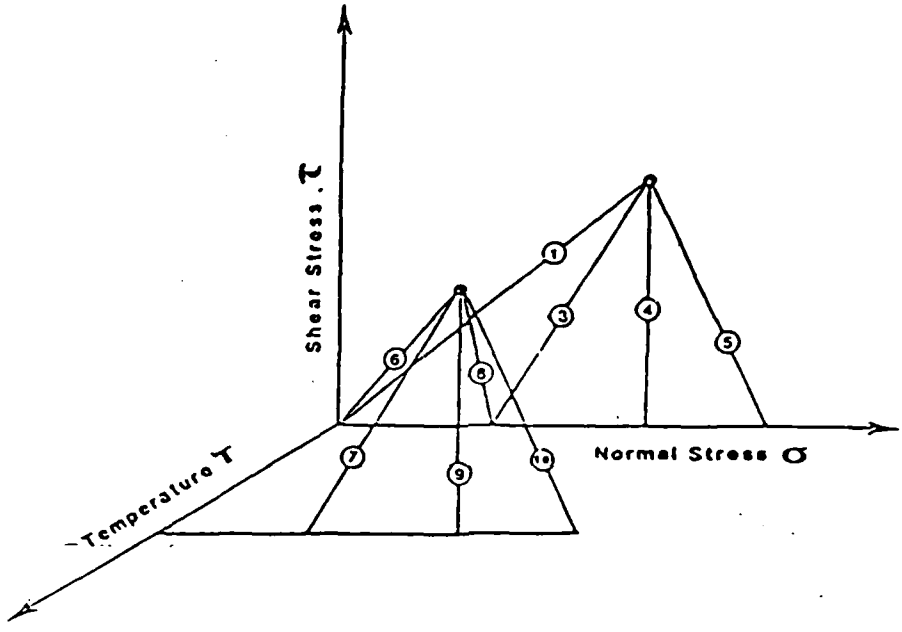

Composite Consolidation Using Various Triaxial Stress States & Temperatures.

Figure A-16

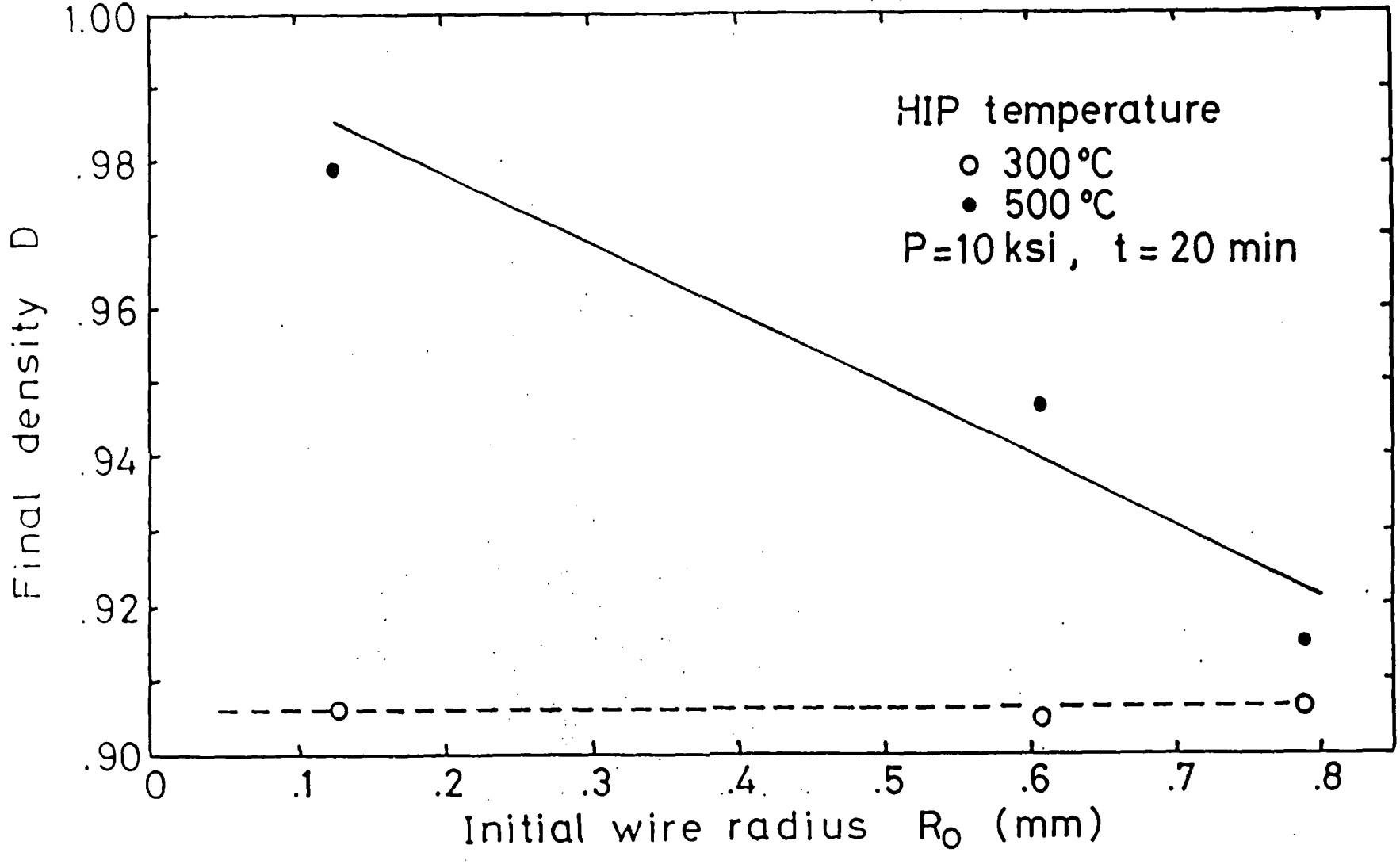

Fig. 5 The effects of temperature and size on the final density of HIP

Figure A-17

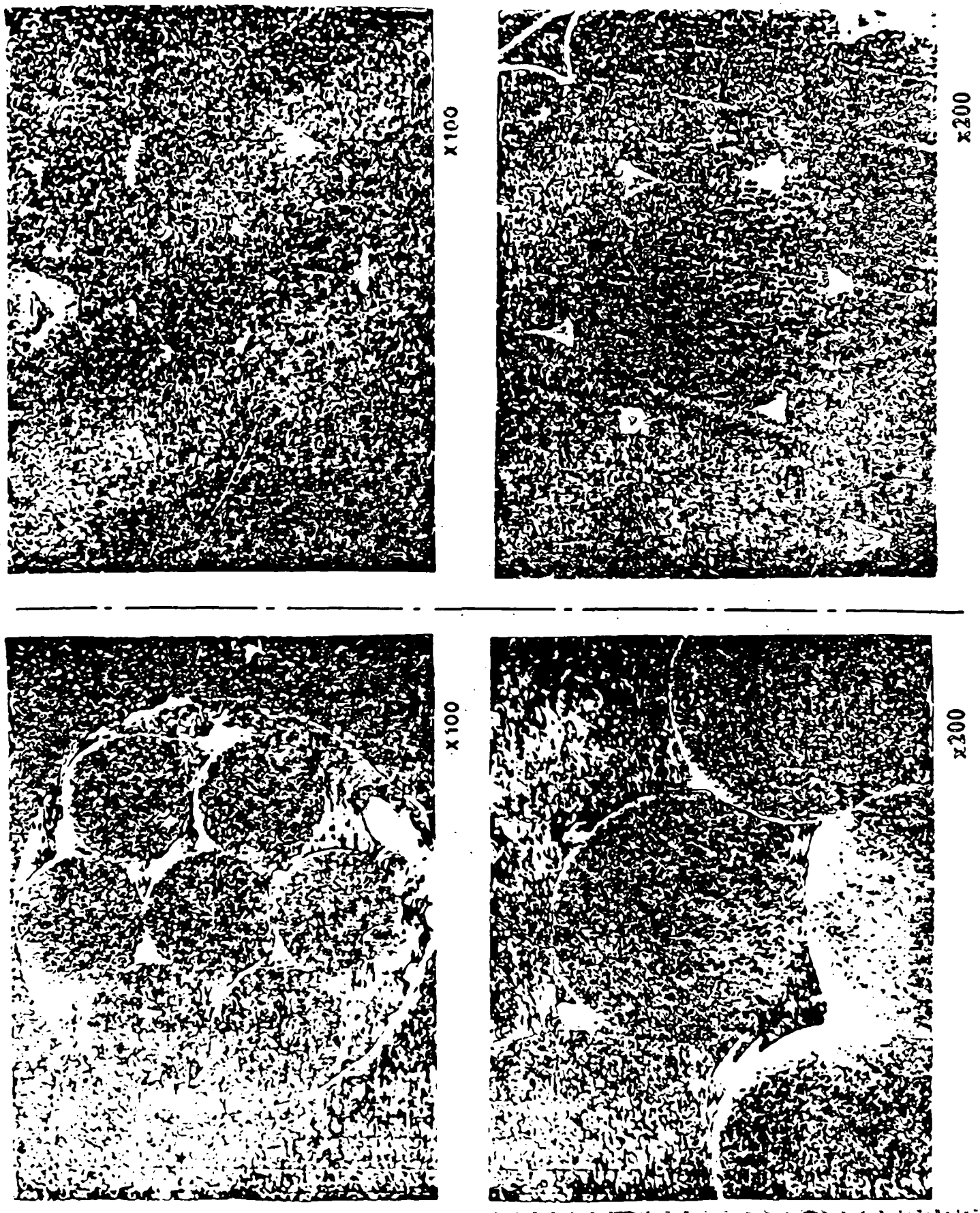

TASK 2

FIRST ANNUAL PROGRESS REPORT

E. Wachtel, J. P. Clement and H. J. Rack

Materials Engineering Activity
Department of Mechanical Engineering
Clemson University
Clemson, South Carolina

November, 1987

The principal objective of this task, being undertaken at Clemson University, is to achieve a fundamental understanding of the factors controlling the elevated temperature flow behavior of metal and ceramic matrix composites. Materials of interest include composites consisting of a ceramic reinforcement, e.g., TiB_2, SiC, or graphite, in a metal or ceramic matrix, e.g., titanium aluminides, nickel-base super alloys, niobium aluminides, and aluminum oxides.

The high temperature deformation behavior of these systems is being approached through a detailed examination of their time-temperature-strain rate dependent flow behavior. Microstructural observations include examination of reinforcement-matrix interfacial reactions, matrix precipitation and coarsening, both prior and subsequent to straining.

ELEVATED TEMPERATURE MACROSCOPIC FLOW BEHAVIOR

This sub-task examines the time-temperature-strain rate dependent macroscopic flow behavior of fiber reinforced composites. Figure 1 shows a block diagram of the high temperature closed-loop servo-hydraulic system currently on order to support this sub-task. This system has several unique features which will allow direct determination of the strain-flow stress behavior of composites over a wide range of temperatures and strain rates. System specifications include:

- Operating temperatures: ambient to 2000° C
- True strain rates: 10^{-7} to 5 sec^{-1}
- Environments: 10^{-5} torr (2000° C), inert (Ar), low pressure H_2
- Sample cooling: direct gas quenching from deformation temperature
- Sample configurations: tensile, compression, fatigue, creep-fatigue, crack growth, bend

Both mechanical and laser(non-contacting) extensometers are under development to allow determination of strains to 2000° C. All software development, i.e., control algorithms and plotting subroutines, has been completed, with delivery of the elevated temperature test system presently scheduled for February 1988.

Initially, the high temperature plastic flow behavior of α_2 and γ titanium aluminide matrices and TiB_2 containing composites will be examined. Subsequent extension of this investigation to NiAl, Ni_3Al and Nb-aluminide matrices and composites is contemplated.

FIBER-MATRIX INTERACTIONS

Selection of appropriate ceramic reinforcements for elevated temperature composites has historically been limited by fiber-matrix interactions. These interactions have been examined for almost twenty years, with the kinetics of layer growth having been found to obey a parabolic rate law, with the thickness, x, of the reaction layer being described as a function of the exposure time, t, by,

$$x = K t^{-n} \exp(-Q/RT)$$

where, for titanium-based composites, n, the parabolic index equals 2 for either α or $\alpha+\beta$ titanium matrices [1], and 3 for β matrices [2], K is a constant whose value depends upon the matrix composition and crystal structure and includes diffusional pre-exponential terms, Q is the activation energy which depends upon whether α or β constitute the

predominant matrix phase, R is the gas constant and T is the absolute temperature.

Table 1 shows that the details of reaction layer growth in titanium- based composites are sensitive to both fiber pre-treatment and fiber chemistry. For example, SiC/Ti results indicate that this composite is sensitive to fiber pre-treatment. The introduction of a C-rich layer on the SiC fiber drastically reduces the initial rate of layer growth in SiC reinforced Ti composites [5]. Once this C-rich region is consummed by layer growth the rate of growth returns to that of the uncoated fiber [6]. This sensitivity makes direct comparisons between composites difficult. Indeed, Tressler et al. [10] suggest that reactivity with a Ti-40A matrix should be rated in the order from highest to lowest, SiC-Al_2O_3-B, while Kennedy and Geschind [11] suggest Al_2O_3-B-SiC for a similar Ti-70A matrix.

The primary goals of this sub-task are to (a) characterize the extent of fiber-matrix interactions observed in titanium aluminide composites and (b) consider the effect of tailored interfaces, as achieved through fiber surface modification, on fiber-matrix interaction and high temperature mechanical properties.

Surface modification techniques being explored emphasize coating by sol-gel transitions of metal (Zr, Si, Cu and Al) hydrous oxides. Initial results indicate that an effective coating will require strict control of solution pH and molarity. In addition, substrate surface topology will be extremely important. For example, Figure 2 shows what effect surface roughness has on coating uniformity, with enhanced hydrous oxide particle nucleation being associated with surface imperfections. These observations are in excellent agreement with the recent results of Katzman [13] who reported that successful SiO_2 coating of graphite fibers required their pre-treatment with amorphous carbon. It appears that this amorphous coating effectively "heals" the graphite surface, decreasing the probability for heterogeneous nucleation of unwanted discrete hydrous oxide particles.

Further studies are currently underway to establish (a)the nature and kinetics of bond formation in this coating process and (b)the subsequent reaction of the hydrous oxide with selected fiber substrates. Once established, these tailored interfaces will be incorporated into model composite systems to assess their viability at high temperatures.

MATRIX PRECIPITATION AND COARSENING

High temperature structural alloys typically contain several precipitate phases introduced to increase strength, control grain size, etc. It is well known that the distribution of these phases may be sensitive to prior thermomechanical treatment. For example, Figure 3 shows a TTT diagram for INCONEL 718, a precipitation strengthened nickel-base superalloy, wherein the distribution of δ Ni_3Nb is sensitive to prior thermomechanical history [15]. Indeed, it is now well accepted that the distribution and size of any phase whose presence can be influenced by heterogeneous nucleation, for example, at grain boundaries or dislocations, will be sensitive to prior thermomechanical history, i.e., the distribution of potential hetero- geneous nucleation sites.

Recent studies have also shown that precipitation phenomena observed in metal matrix composites may be quite different from unreinforced alloys [16,17]. Furthermore the degree of sensitivity appears to be a function of fiber length to diameter ratio, that is the precipitation kinetics in particulate reinforced composites are similar to unreinforced alloys [18], while precipitation kinetics in whisker reinforced alloys are dissimilar [16]. Preliminary observations suggest that this sensitivity may be related to the presence of dislocation networks in whisker reinforced metal matrix composites and their absence in particulate reinforced materials. While it has been hypothesized that the this dislocation network is formed during cooling from the solution treatment temperature as a result of differences in thermal coefficient of expansion between the ceramic reinforcement and the metal matrix, it is not clear why this network should be observed in whisker reinforced

alloys and be absent in particulate composites.

The primary objective of this sub-task will be to extend these investigations of the effect of the presence of a ceramic reinforcement on precipitation hardening to high temperture structural materials. Currently these studies are focused on TiC reinforced INCONEL 718. The aging kinetics of ingot, powder and TiC reinforced INCONEL 718 having identical thermo- mechanical history are being examined.

REFERENCES

1. A. G. Metcalf, "Physical Chemical Aspects of the Interface", Composite Materials, ed. A. G. Metcalf, Academic Press, New York, 1974, Vol. 1, pp. 67-123.

2. L. S. Guzei, E. M. Sokolovovskaya, L. L. Tschunichina, V. I. Shulepov and T. A. Tshemleva, "The Interaction Between Titanium Alloys and SiC- Fibers", Titanium '80, Science and Technology, ed. H. Kimura and O. Izumi, AIME, Warrendale, Pa., 1980, pp. 2301-2308.

3. A. G. Metcalfe and M. J. Klein, "Compatible Alloys for Titanium Matrix Composites", Titanium Science and Technology, ed. R. I. Jaffee and H. M. Burte, Plenum Press, New York, 1973, pp. 2285-2298.

4. H. J. Dudek, R. Leucht and G. Ziegler, "Auger Electron Spectroscopy of the Interface of SiC Fiber Reinforced Titanium Alloys", Titanium Science and Technology, ed. G. Lutering, U. Zwicker and W. Bunk, Deutsche Gesellschaft fur Metallkunde, Munich, FRG, 1985, pp. 1773-1780.

5. T. E. Steelman, R. H. Lorenz, G. R. Martin and R. P. Robelotto, Silicon Carbide/Titanium Material and Process Fundamentals, AFWAL-TR-82-4036, May, 1982.

6. C. G. *Rhodes* and R. A. Spurling, "Fiber-Matrix Reaction Zone Growth Kinetics in SiC-Reinforced Ti-6Al-4V as Studied by *Transmission* Electron Microscopy", Recent Advances in Composites in the United States and Japan, ed., J. R. Vinson and M. Taya, ASTM STP 864, ASTM, Philadelphia, Pa., 1985, pp. 585-599.

7. E. P. Zironi and H. Poppa, "Micro-area Auger Analysis of a SiC/Ti Fibre Composite", Jn. of Materials Science, Vol. 16, 1981, PP. 3115- 3121.

8. H. J. Dudek, L. A. Larsen and R. Browning, "Study of the Fiber/Matrix Interface in a SiC Reinforced Titanium Alloy Using a High Resolution Field Emission Auger Microprobe", Surface and Interface Analysis, Vol. 6, 1984, pp. 274-278.

9. R. E. Tressler, T. L. Moore and R. L. Crane, "Reactivity and Interface Characteristics of Titanium-Alumina Composites", Jn. of Materials Science, Vol. 8, 1973, pp. 151-161.

10. R. E. Tressler and T. E. Moore, " Mechanical Property and Interface Reaction Studies in Titanium-Alumina Composites", Metals Engineering Quarterly, Vol. 11, 1971, pp. 16-21.

11. J. Kennedy and G. Geschwind, "Interfacial Reactions in Potebtial Titanium Matrix Composites", Titanium Science and Technology, ed. R. I. Jaffee and H. M. Burte, Plenum Press, New York, 1973, pp. 2299-2312.

12. J. Kennedy, "Reaction Zones in Ti/W Composites", Jn. of Materials Science, Vol. 8, 1973, pp. 291-294.

13. H. A. Katzman, "Fibre Coatings for the Fabrication of Graphite-Reinforced Magnesium Composites", Jn. of Materials Science, Vol. 22, 1987, pp. 144-148.

14. J. W. Brooks and P. J. Bridges, "Long Term Stability of INCONEL Alloy 718 for Turbine Disc Applications", High Temperature Alloys for Gas Turbines and Other Applications 1986, ed. W. Betz, R. Brunetaud, D. Coutsouradis, H. Fischmeister, T. B. Gibbons, I. Kvernes,

Y. Lindblom, J. B. Marriott and D. B. Meadowcroft, D. Reidel Publ. Co., Dordrecht, Holland, 1986, pp. 1431-1440.

15. J. F. Barker, D. D. Krueger and D. R. Chang, "Thermomechanical Processing of INCONEL 718 and its Effect on Properties", Advanced High-Temperature Alloys: Processing and Properties, ed. S. Allen, R. M. Pelloux and R. Widmer, ASM, Metals Park, Ohio, 1986, pp. 125-137.

16. H. J. Rack and J. W. Mullins, "Tensile and Notch Tensile Behavior of SiC$_w$ Reinforced 2124 Aluminum", High Strength Powder Aluminum Alloys: II, ed., G. J. Hildeman and M. J. Koczak, AIME, Warrendale, PA, 1986, pp. 155-171.

17. H. J. Rack, "Age Hardening Behavior of SiC whisker Reinforced 6061 Aluminum", Proc. Sixth International Conference on Composite Materials, Vol. 2, ed., F. L. Matthews, N. C. R. Buskell, J. M. Hodgkinson and J. Morton, Elsevier Applied Science, London, 1987, pp. 382-389.

18. D. Lloyd, ALCAN International, Private Communication, 1987.

TABLE 1

System	Max. Reaction Temp. (°C)/Time(h)	Reaction Products	Ref.
SiC/Ti-6Al-4V	1000/(a)	Ti_5Si_3(TiC)/TiC	4
SiC/Ti-6Al-4V	955/10	(a)	5
SiC(SCS-6)/Ti-6Al-4V	900/100	TiC, Ti_5Si_3/TiC(Ti_5Si_3)/Ti_5Si_3	6
SiC /Ti	1150/8	TiC	7
SiC/Ti-6Al-4V	950/1	TiC/Ti_5Si_3	8
Al_2O_3/Ti		Ti_3Al/TiO-type $(Ti,Al)_2O_3$	9
/Ti-6Al-4V		"	9, 10
/Ti-8Al-1V-1Mo	926/70	"	9
/Ti-6Al-2Sn-4Zr-2Mo	926/70	"	9
/70A, 75A	1000/100	(Ti_3Al/Ti_2Al/TiAl)	11
B/Ti-40A	1038/7000	TiB_2	3
/Ti-75A		"	
B/Ti-Si, Sn, Cu, Cr, Al, Mo, Zr, V (b)	760/100	"	
Borsic/Ti-6Al-4V	955/10	(a)	5
B_4C-B/Ti-6Al-4V	955/10	(a)	5
W/Ti-75A	1000/100	Ti-W Eutectoid	11
/Ti-75A	930/		12
C/Ti-70A	(a)	TiC	11

(a) NG-Not reported
(b) Exact composition not given

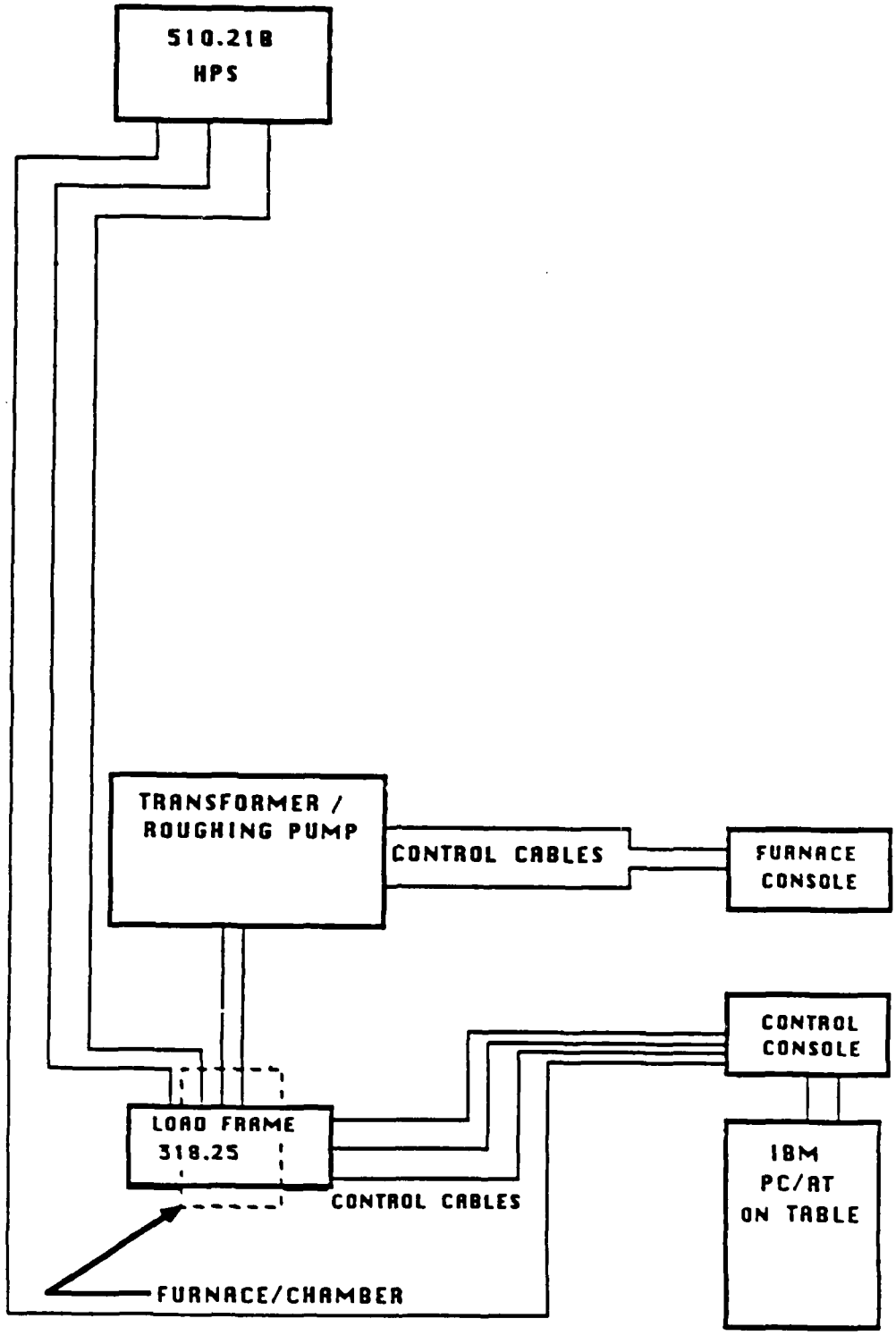

Figure 1: Block Diagram of High Temperature Closed-Loop System.

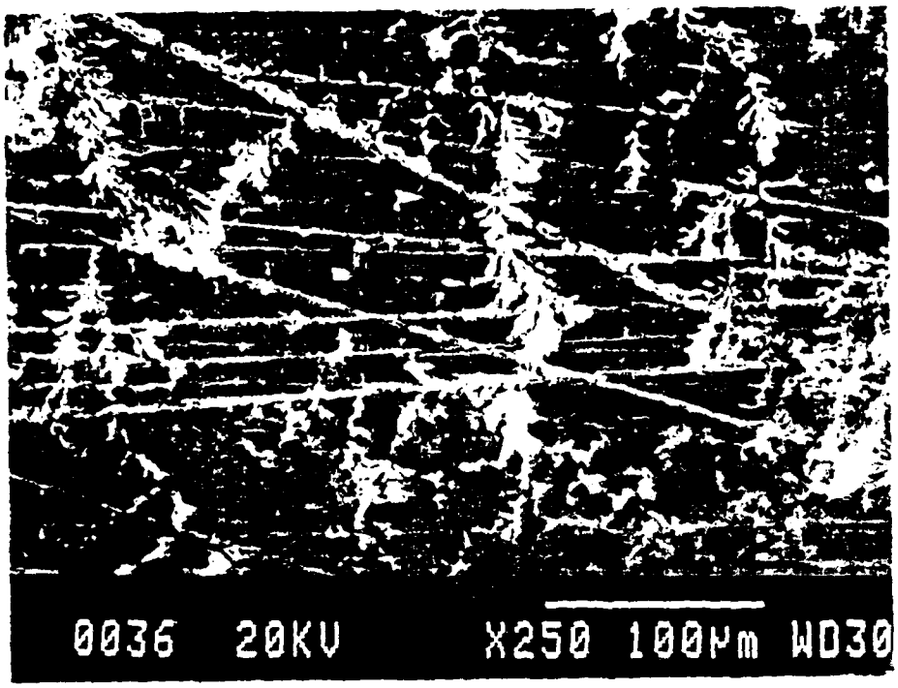

Figure 2. Surface topology for hydrous ZrO_2-coated SiO_2 glass.

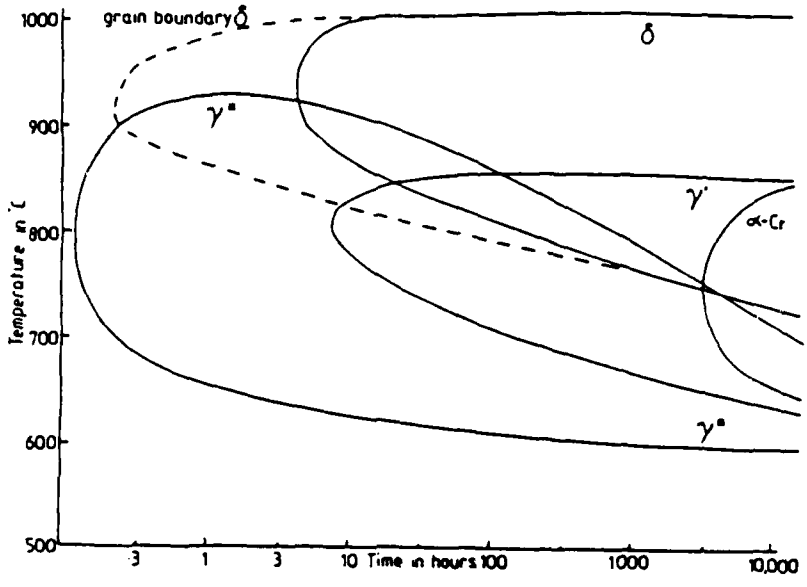

Figure 3: Time-Temperature-Transformation Diagram for INCONEL 718.

SECTION 2

CHARACTERIZATION

Interfacial Structure and Stability in Metal and Intermetallic-Matrix Composites

James M. Howe, Principal Investigator

Objectives

The purpose of this research is to determine the role of the matrix/reinforcement interface on the ambient and elevated-temperature behavior of metal-matrix and intermetallic-matrix composites. These results are expected to provide: 1) a fundamental understanding of interfacial structure and behavior between dissimilar materials, 2) a fundamental understanding of the role of interfaces on the mechanical behavior and high-temperature stability of composites, and 3) sufficient microstructural information to optimize composite performance.

Approach

A combination of analytical electron microscopy (AEM), high-voltage electron microscopy (HVEM) *in situ* studies and atomic-resolution microscopy (ARM) are being use to determine:

- The dislocation structures and sources present at the matrix/reinforcement interfaces and their effect on nearby matrix phases and deformation behavior,
- Details of atomic bonding across matrix/reinforcement interfaces and their relation to interfacial strength and deformation behavior,
- The stress distribution in the matrix around reinforcements,
- High-temperature microstructural changes which occur during composite processing and service.

- The growth kinetics, structure, crystallography and interfacial structure of reaction products that form at matrix/reinforcement interfaces as a function of processing and service.

Research Results from Year 1

The first year of this program concentrated on developing an understanding of interfacial structures and stresses associated with SiC_w in AA2124 and AA1100 alloy matrices. There were several reasons for this: 1) some interfacial work has been performed on Al-matrix systems and many effects such as interfacial structure, stresses, dislocations, etc. have been identified to be important to the composite properties although the detailed mechanisms and reasons for these effects are still not well characterized or understood, 2) the fabrication technology of these composites is fairly well established and a variety of materials are readily available, and 3) the simplicity of the Al alloy matrix materials compared to intermetallic matrices makes them a good starting point from which to develop techniques for examination and establish a fundamental knowledge base before progressing on to more complicated higher-temperature systems.

One graduate student, a post-doctoral research associate and one part-time graduate student were hired for the program this year. The emphasis of each of these researchers during Year 1 is indicated in the flow chart in Fig. 1. The post doctoral research associate Dr. G. Mahon established procedures for preparing Al-alloy composites, started detailed microstructural investigations of the internal structure of SiC_w, the interfacial structure between SiC_w and the AA2124 matrix, and the effect of dislocations formed during heat treatment on nearby matrix precipitates and deformation behavior. The graduate student S. Rozeveld also participated in developing sample preparation techniques, investigated heat treatments for minimizing dislocation production during cooling from elevated temperatures in order to study residual elastic stresses around the reinforcement particles, developed computer programs for calculating electron diffraction patterns from faulted SiC_w, and also developed the samples and techniques for performing *in situ* tensile deformation studies of these composites in the scanning electron microscope (SEM). The part-time graduate student Rodney Strychor has been involved with heat treatment and sample preparation for performing APM on interphase boundaries in TiAl-base alloys. Results from these studies are summarized below.

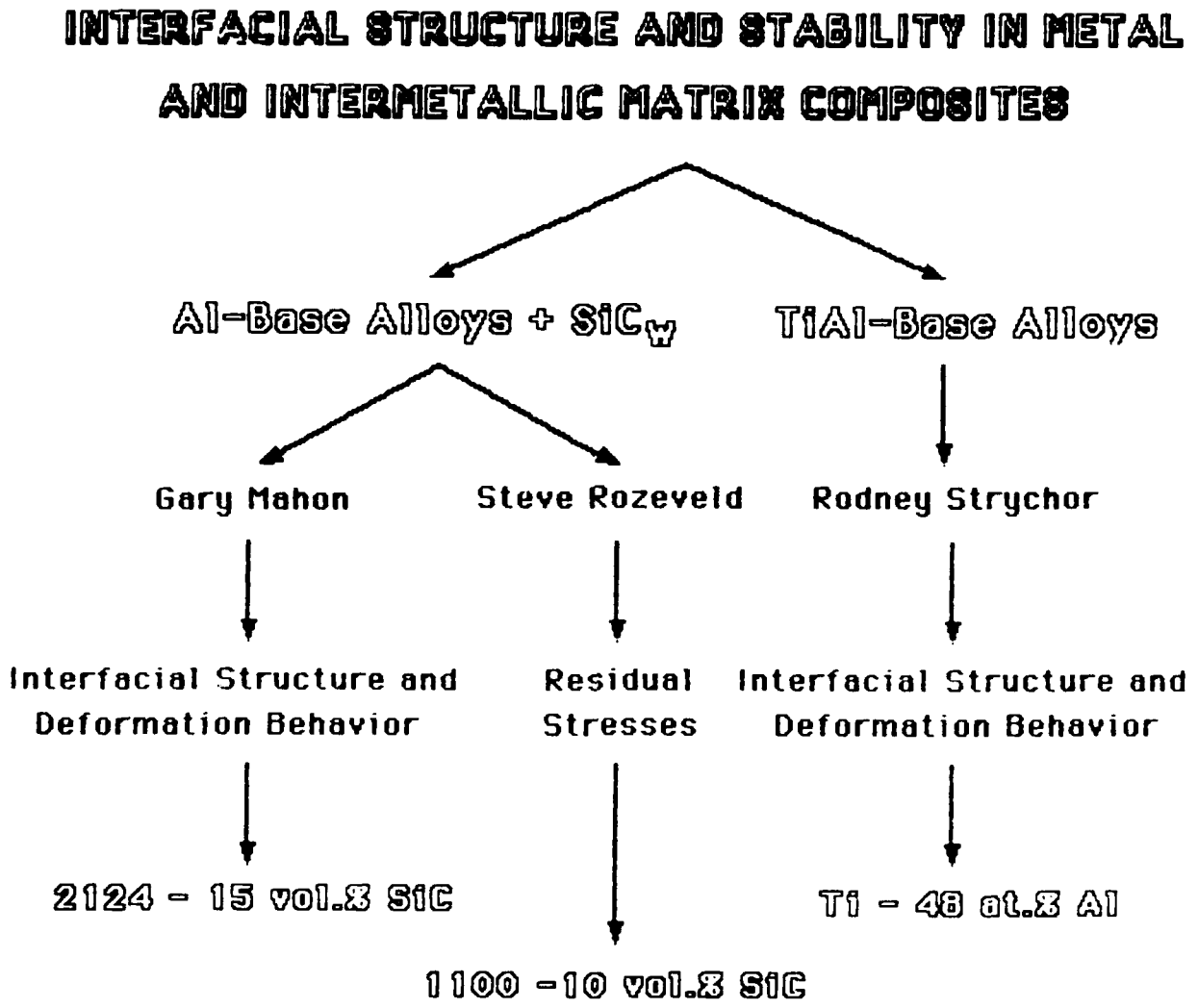

Figure 1. Organization of interfaces program during Year 1.

Internal and Interfacial Structures of SiC_w in AA2124 Alloy

The purpose of this research is to understand the internal and interfacial structures of composites and their effects on composite behavior at as fundamental level as possible. Figure 2(a) shows the end of a SiC_w in AA2124 alloy viewed perpendicular to the long axis of the fiber by transmission electron microscopy (TEM). It is clear from the image that the fiber is heavily faulted, and by comparing the corresponding electron diffraction pattern in Fig. 2(b) with calculated patterns based on various cubic, hexagonal and rhombohedral polytypes, the fiber was determined to be β-SiC. This is a zinc-blende structure containing a high density of microtwins on the $(1\bar{1}1)$ planes, as illustrated by the calculated electron diffraction pattern for this structure in a [011] zone axis in Fig. 2(c), which may be compared with the experimental pattern in Fig. 2(b). Several other investigators have incorrectly identified these fibers as hexagonal α-SiC. It is also interesting to note that the high density of microtwins produces serrated fiber sides, particularly evident along the lower edge of the fiber at A in Fig. 2(a).

Two arrows in Fig. 2(a) identify particular corners at the fiber end, which is somewhat rounded rather than flat with square corners as often assumed, and these corners are shown in a different perspective in Fig. 3. In Fig. 3 the fiber has been tilted so that the end is viewed at an angle and the same corners are again indicated by arrows. It is important to note that a number of dislocations appear to have been emitted from the fiber during quenching, presumably due to thermal mismatch, and particularly, that these emitted dislocations terminate at the rather sharp corners indicated by the arrows. This provides direct evidence that very local features in the interface such as sharp corners are preferred sites for dislocation generation. Such behavior has been proposed but never verified experimentally. Sharp corners and discontinuities may also be preferred sites for dislocation generation during deformation of the composites, although this remains to be confirmed.

Another feature apparent in Fig. 3 is that several helical dislocations appear to terminate at the matrix/reinforcement interface. These helical dislocations are produced by condensation of quenched-in vacancies on screw dislocations, and their termination at the interface again indicates that the interface is a source of dislocations even at relatively high temperatures. Furthermore, it is interesting to note that the radii of many of the helical loops decrease as the interface is approached. Since the

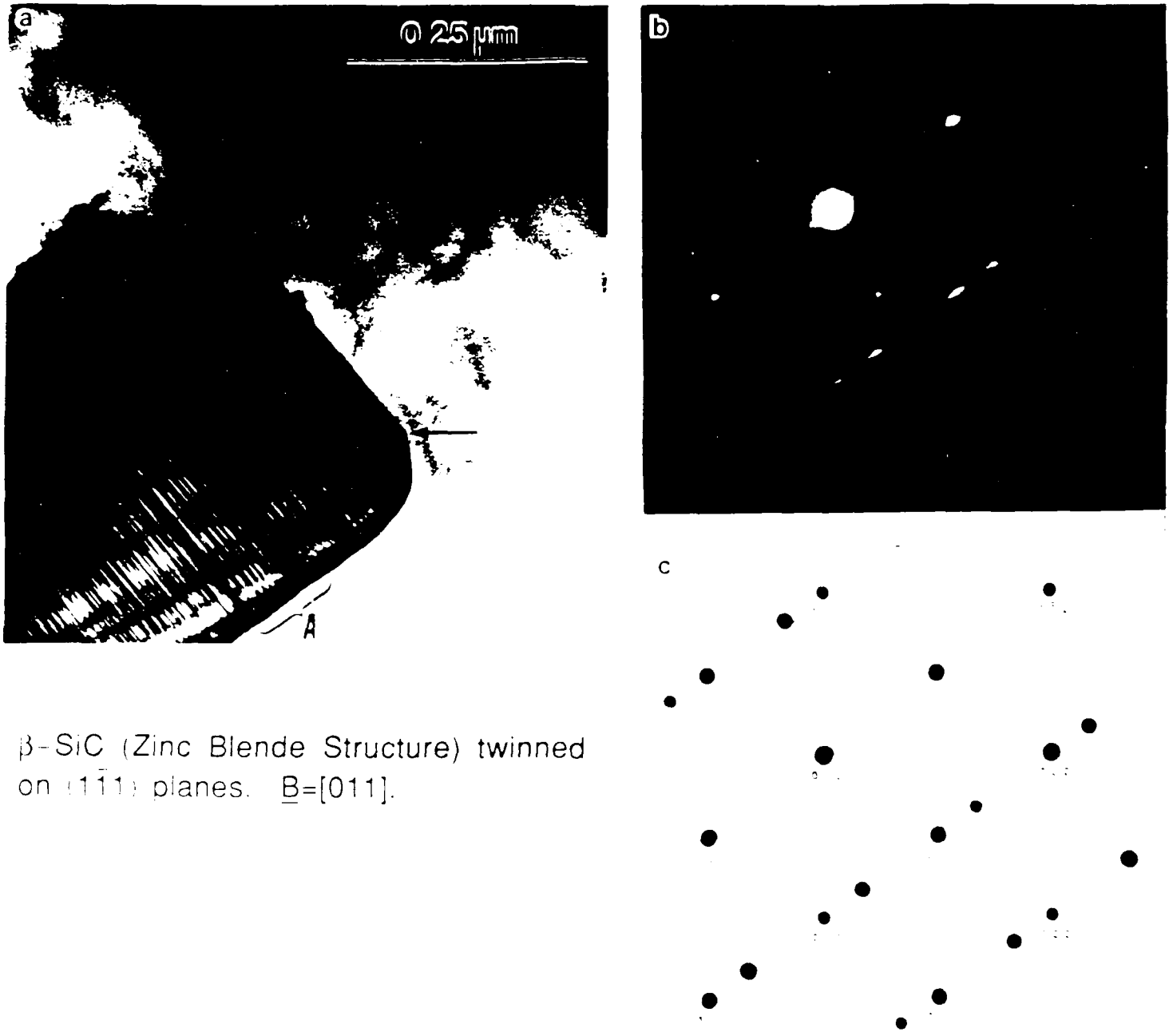

β-SiC (Zinc Blende Structure) twinned on $(1\bar{1}1)$ planes. $\underline{B}$=[011].

Figure 2 : [illegible] TEM image of SiCw in as-quenched AA2124 [illegible] selected-aperture diffraction pattern, and (c) calculated [illegible] twinned [illegible] structure.

Figure 3. (a) Weak-beam dark field TEM image, and (b) bright-field TEM image of SiC$_w$ in Fig. 2(a) tilted to view fiber end.

radius of a loop in a dislocation helix increases with increasing vacancy supersaturation, this behavior indicates that the interface is a sink for vacancies. Since precipitation in AA2124 alloy is strongly dependent on the vacancy supersaturation, it is likely that vacancy depletion at the interface may have a major effect on subsequent precipitation reactions, and the dislocations generated at the interface will also have a major effect on the strength and deformation behavior locally around the fibers.

Figure 4 shows similar helical dislocations associated with a Mn-containing dispersoid in the base AA2124 alloy. Again these helices terminate at the matrix/particle interface, often at particle corners and with decreasing radii and these similarities to the SiCw suggests that the SiC fibers in many ways resemble the Mn-containing intermetallic particles that are commonly found in Al alloys, and are likely to have similar effects on precipitation reactions in the matrix.

In Situ Deformation Studies

Flat tensile specimens of the SiCw + AA2124 composite were produced with the fiber axis parallel to the tensile axis, as sketched in Fig 5, and the specimens were ruled so that measurments of strain could be determined locally on the samples. The purpose of observing the deformation behavior of this material *in situ* was to try to answer the following questions:

- Where does fracture initiate locally with respect to the fiber, at the sides or ends?
- What strain is required for nucleation of voids at the interface?
- What microscopic features of the fiber interface correlate with nucleation?
- What strain would be optimum for examining the role of the interface on deformation?

The results from these *in situ* studies did not answer several of these questions but instead provided some unexpected and interesting results Essentially, almost no evidence of void formation was apparent at the matrix/fiber interfaces until fracture occurred, and then voids were only apparent near the fracture surface. Near this surface, a considerable amount of both particle cracking and matrix/reinforcemnet decohesion at

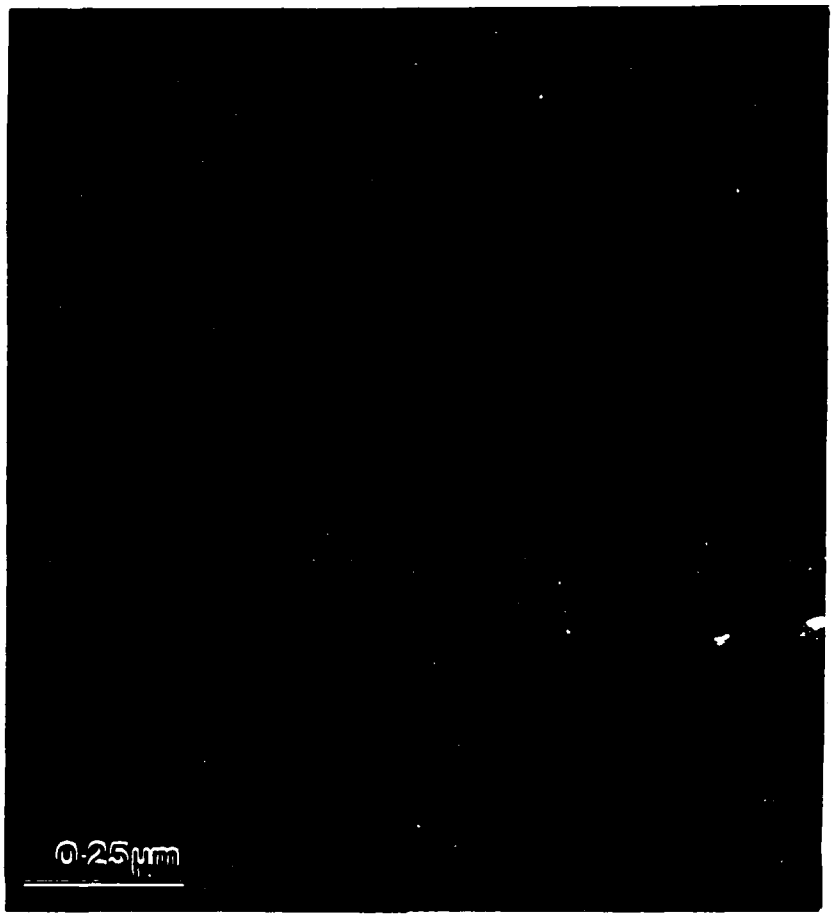

Figure 4. Helical dislocations emanating from a Mn-containing particle in AA2124 base alloy.

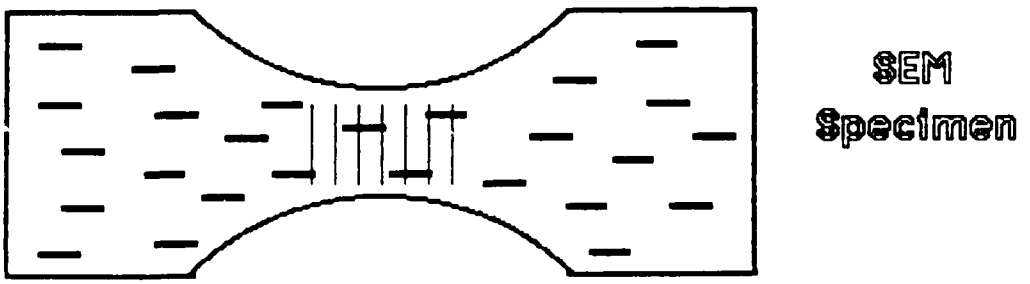

Figure 5. Sketch of SiCw SEM tensile specimen with fibers indicated as heavy lines and grid marks as light lines

the fiber ends was evident, as shown for an aged sample in Fig. 6. However, the ratio of particle cracking to fiber decohesion appeared to vary with heat treatment, as illustrated by the SEM micrographs in Fig. 7.

Figures 7(a) and (b) show the fracture morphology of a naturally-aged sample, and a considerable amount of fiber pull-out or decohesion is evident on the fracture surface. In the artificially-aged sample shown in Figs. 7(c) and (d), there is not much evidence of fiber decohesion, suggesting that the interfacial bond is stronger after aging. This was also evident in the load (stress)-strain curves for these two samples, shown in Fig. 8. The aged sample displayed a smooth stress-strain curve with continual work hardening to fracture, while the naturally aged sample displayed significant load drops during straining, as though the matrix/fiber interfaces were separating and relieving the load. These are preliminary results and further investigation of the role of the interfaces, matrix deformation mode and strain aging need to be performed to fully understand these differences in mechanical behavior.

Residual Stress Measurements

The purpose of this research is to provide accurate local measurements of the elastic stresses around reinforcements in order to compare the magnitude of the stresses with theoretical calculations and to determine the effects of such stresses on composite performance. This study was initially hampered by the unavailability of a low volume-fraction large-grained AA1100 + SiC_W material, so that stress measurements could not be performed around isolated fibers without superimposed effects from adjacent fibers or grains. Additionally, annealing and quenching from the annealing temperature inevitably produced dislocations which severely complicated local determination of elastic stresses by convergent-beam electron diffraction (CBED). These problems were recently overcome by acquiring a cast AA1100 + SiC_W composite containing relatively large isolated SiC particles in large matrix grains, as well as developing a low-temperstue annealing cycle which provides sufficient thermal energy for annihilation of dislocations while maintaining a high enough temperature to produce significant thermal mismatch between the matrix and reinforcement during cooling to room temperature. Computer programs for simulating higher-order Laue zone (HOLZ) lines in CBED patterns for local lattice parameter measurements have been acquired and adapted to a computer in our department, and programs for calculating the elastic stresses around the fibers, including different elastic constants and

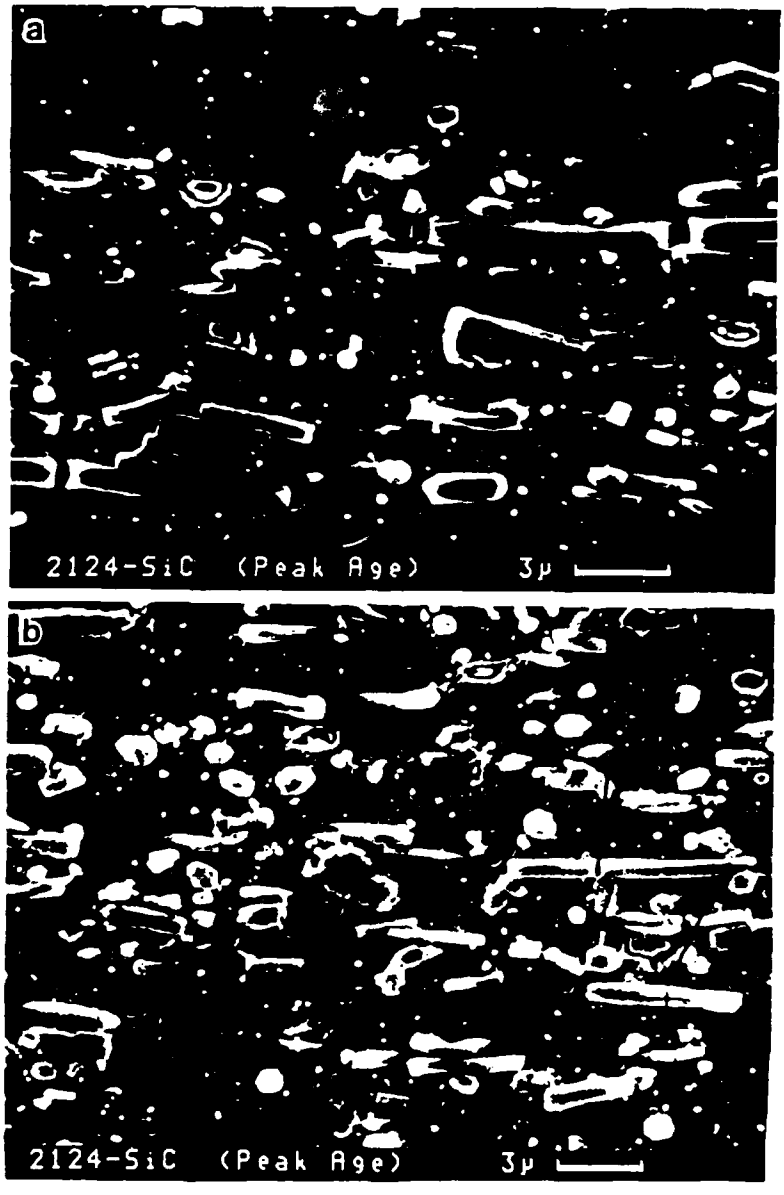

Figure 6. (a-b) SEM images of fiber cracking and decohesion (arrows) on the surfaces of SEM tensile samples

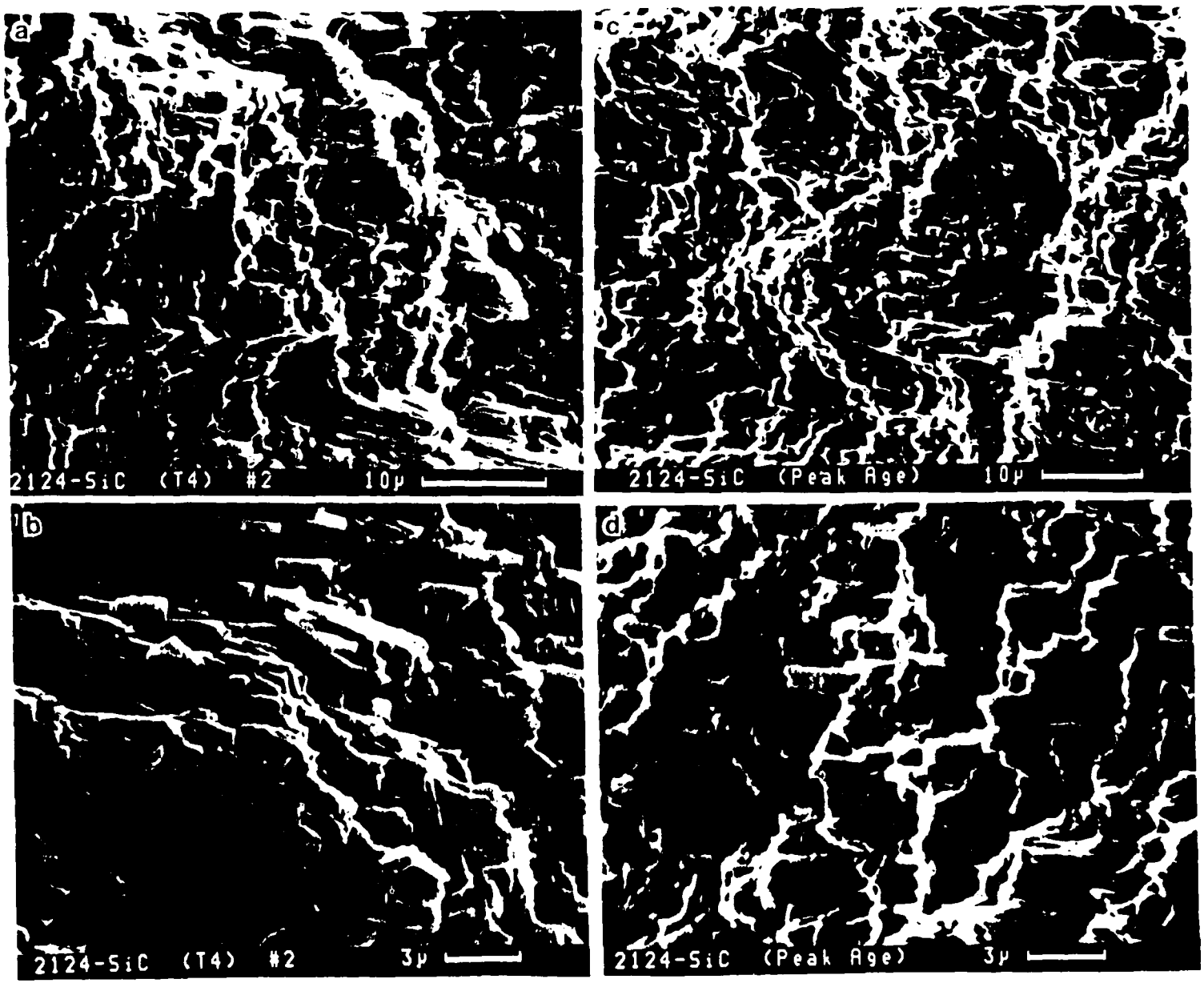

Figure 7. (a-d) SEM images of fracture surfaces from *in situ* tensile specimens of naturally and artificially-aged composites

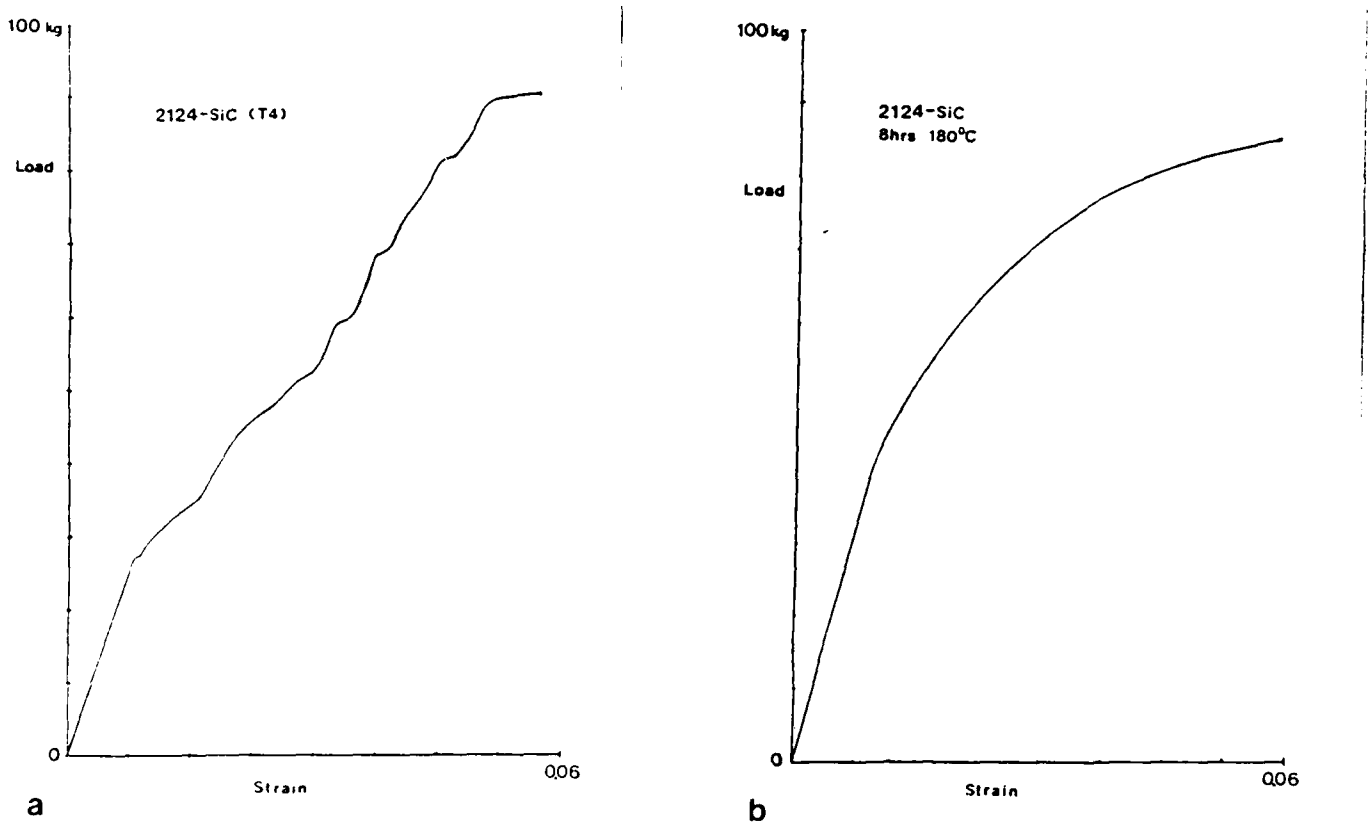

Figure 8. Stress-strain curve for (a) naturally aged (T4), and (b) artificailly-aged (T6) composites.

anisotropic elasticity, are also being developed for comparison with the experimental measurements.

Research Plans for Year 2

It is evident from the results of Year 1 that topics 1, 3 and 4 in the Approach section have been invesigated significantly in two Al + SiC_w systems. Although investigation of topics 2 and 5 are possible in these composites, they are probably better performed on model systems and/or Ti-base alloys, as discussed in more detail below.

In response to the AFOSR's desire to perform fundamental studies of interfacial structure in composites which are to be used for high-temperature applications, a major portion of the effort in this program is being directed to examine interfacial structures in both Ti_3Al (α_2) and TiAl (γ) -base alloys (Fig. 9), with and without continuous AVCO SCS6 (SiC) fibers. At the same time, investigations are continuing in a few areas of Al + SiC_w composites which are previously unexplored, but appear to be critical for developing a fundamental understanding of interfacial reactions and their effects on the mechanical properties of composites. These research areas are explained below, beginning with continued research in Al + SiC_w materials and followed by new research in Ti_3Al and TiAl matrix composites with SCS6 continuous fibers.

Al + SiC_w Composites

Two areas in which considerable progress has been made during Year 1 and in which we are now in a position to determine some new and fundamental information about interfaces in composites are: 1) the effects of interfacial structure on dislocation generation under cyclic thermal exposure and deformation, and 2) measurement of residual stresses around SiC fibers. In order to address these topics we plan to:

- Perform TEM investigations of under, peak and over-aged samples of AA2124 + SiC_w which have been deformed 3% in tension, in order to correlate the effects of interfacial structure on the dislocation configurations in the matrix.

- Cyclicly cool samples such as the one shown in Fig. 3 between room temperature (~25°C) and liquid nitrogen temperature (~-190°C) *in situ* in

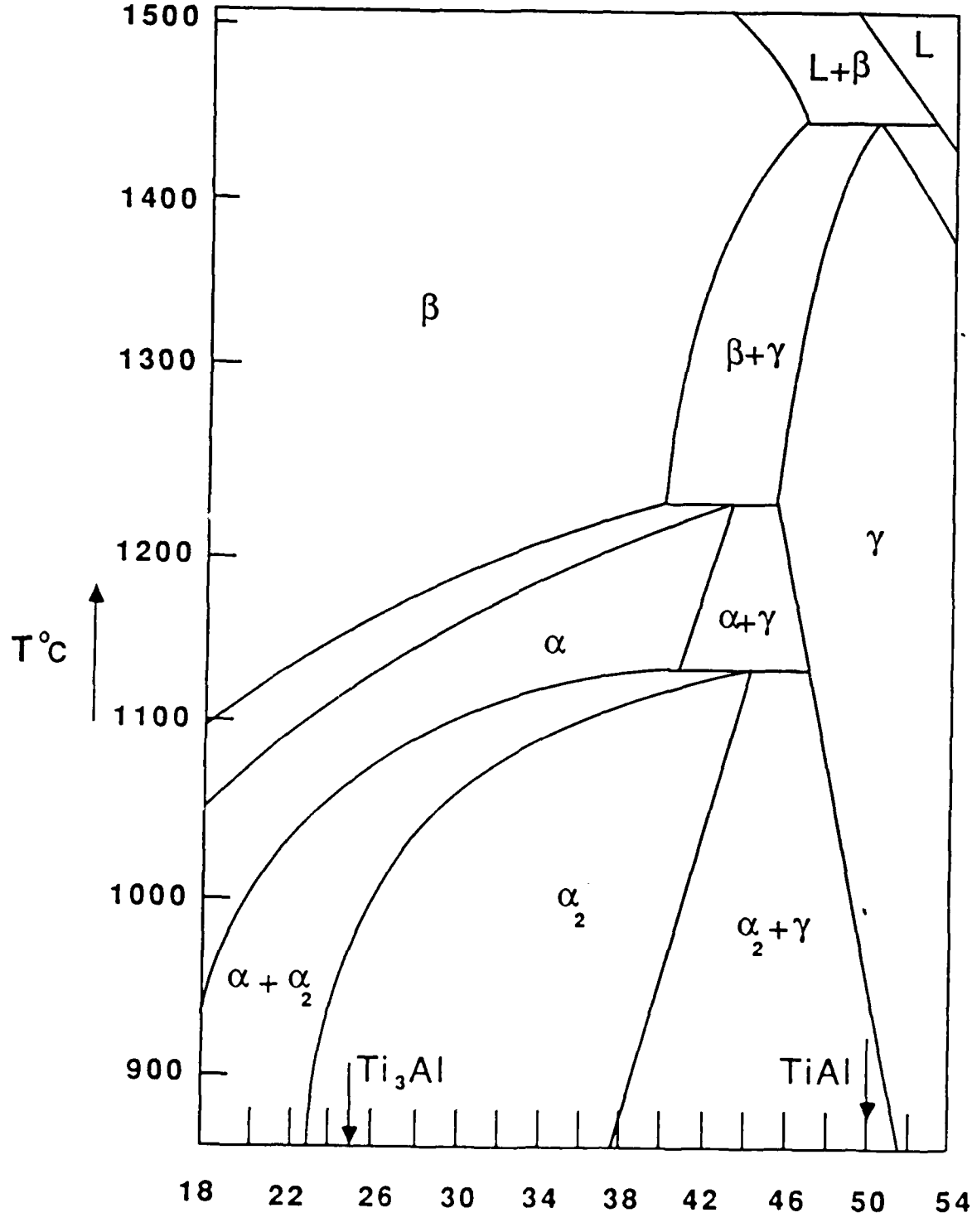

Figure 9. Partial Ti-Al equilibrium phase diagram showing the Ti_3Al and TiAl phase fields.

the TEM, to observe dislocation emission from interface discontinuities and follow defect accumulation as a function of the number of cycles, and

- Perform experimental measurements of stresses around individual fibers as described previously. Although a number of investigators have theoretically predicted the elastic stresses around fibers, no experimental measurements of these stresses have been performed to date.

All of these topics will provide fundamental information that can be utilized not only for understanding the role of interfaces in Al-base matrices, but also for comparison with similar studies in Ti-base matrices and as model experiments for determining the limitations of the experimental techniques employed, such as in the *in situ* studies and lattice parameter measurements being performed to analyze detailed and fundamental aspects of composite microstructures.

Ti-Base Composites

Three investigations are being started in Ti-base composites, all concerned with establishing a fundamental understanding of interfacial structure in these alloys and the role of these interfaces on the mechanical properties of composites. These investigations are:

- Determination of the atomic structure and dislocation configuration of the α_2/β interface in Ti_3Al-base alloys and the behavior of this interface during deformation,

- Determination of the atomic structure and dislocation configuration of the α_2/γ interface in TiAl-base alloys and the behavior of this interface during deformation, and

- Development of an understanding of the atomic structure, crystallography and reaction kinetics of SCS6 continuous fibers in Ti-base matrices, particularly Ti_3Al-base systems.

These areas were selected for three reasons: 1) although current alloy design philosophies indicate that the α_2/β and α_2/γ interfaces are likely to be present in many types of Ti-base composites, their structures and deformation behavior are not well understood, 2) the crystallographic relationships among the phases involved are simple enough to be investigated at the atomic level and are likely to provide fundamental information about the atomic structures of interfaces and the behavior of

these interfaces in technologically important systems, and 3) SCS6 fibers appear to be the primary reinforcement planned for Ti-base matrix composites, although not much is known about the structure of the fibers, their reaction behavior with Ti-alloy matrices and the effects of both on the properties of Ti-base composites. Some initial results from areas 2 and 3 above are discussed in the following.

Atomic Structure of the α_2/γ Interface

As a first step in understanding the atomic structure of the α_2/γ interface, an atomic model of the interface was constructed using current crystallographic information about the structures of Ti_3Al and TiAl. Figure 10 shows a possible interfacial structure, based on a geometric hard-sphere model and preferred bonding between Ti and Al atoms. The most important feature to notice in this model is that if the interface is examined along a $\langle 110\rangle_{Ti3Al}//\langle 11\bar{2}0\rangle_{TiAl}$ direction parallel to the interface plane (arrow in Fig. 10), alternate Ti and Al-rich atomic columns can be distinguished in both phases at the interface, and this same feature should be seen in ARM. Further, regular dislocation structures and ledges have been observed to form at this interface and thermal antiphase boundaries (APBs) in α_2 also intersect the interface. Understanding all of these features at an atomic level in terms of the crystal structures of the two phases will provide substantial insight into the fundamental behavior of interfaces in ordered alloys. The same is expected in studies of the α_2/β interface.

Continuous SCS6 Fibers

The SCS6 fibers are produced by AVCO using a chemical-vapor deposition (CVD) process. These fibers are mainly SiC in the center and possess a number of outer layers containing various proportions of Si and C for bonding to the SiC and wetting with matrix materials. Initial studies of the SCS6 fibers show that the SiC has a columnar grain structure (inset in Fig. 11) which grows radially outward, and that the SiC is enveloped by a layer of amorphous material, thought to be C. Examination of both the conventional TEM image in the inset as well as the accompanying high-resolution TEM image of the SiC/amorphous interface shows that it is rough on both the microscopic and atomic levels. It also appears that the interface is continuous and completely solid at the atomic level. A thick layer of reaction products was observed at the reinforcement/matrix interface in this composite, and elemental analyses of the fiber layers, reaction products and adjacent matrix are being performed.

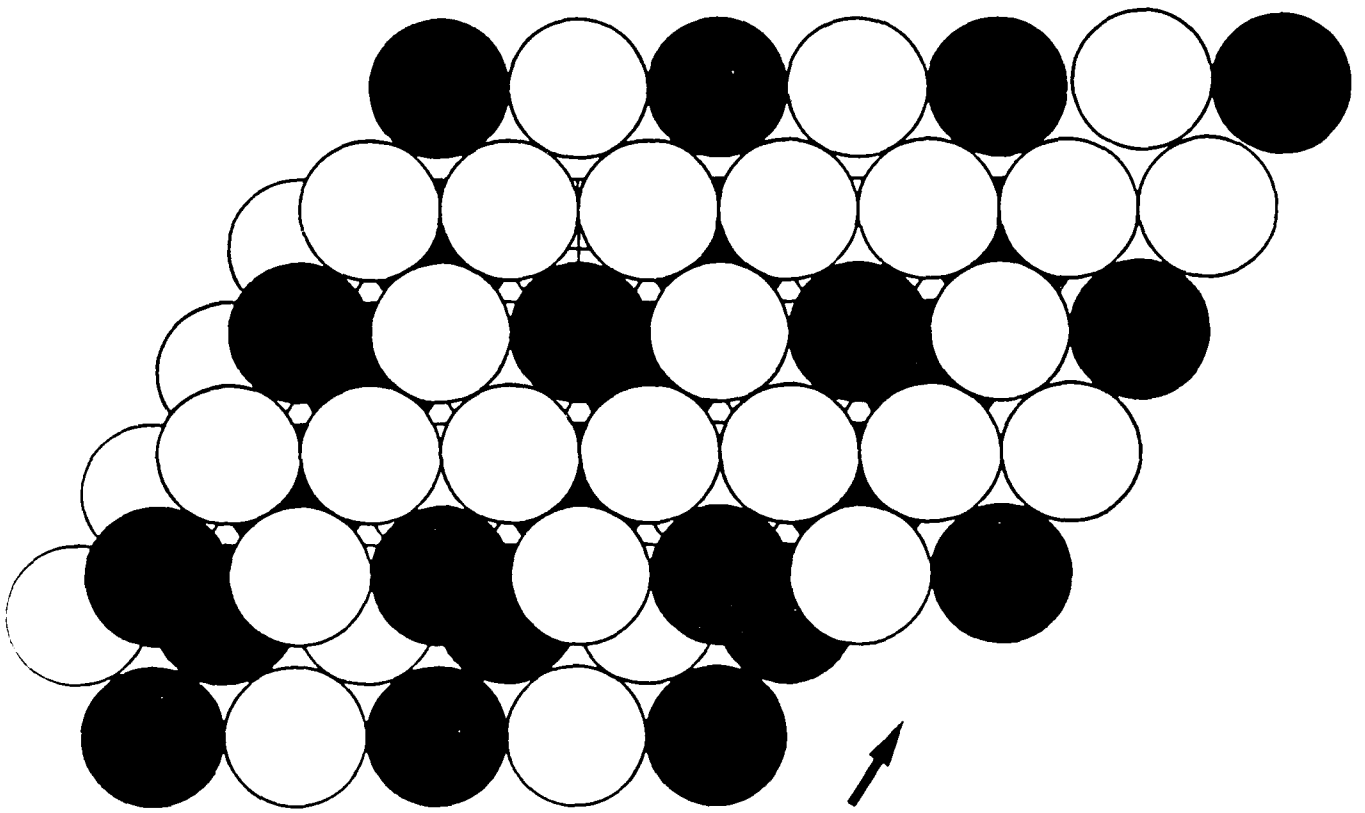

Figure 10. A possible model for the α_2/γ interface seen perpendicular to the interface plane. Open circles represent Ti atoms and filled circles represent Al atoms.

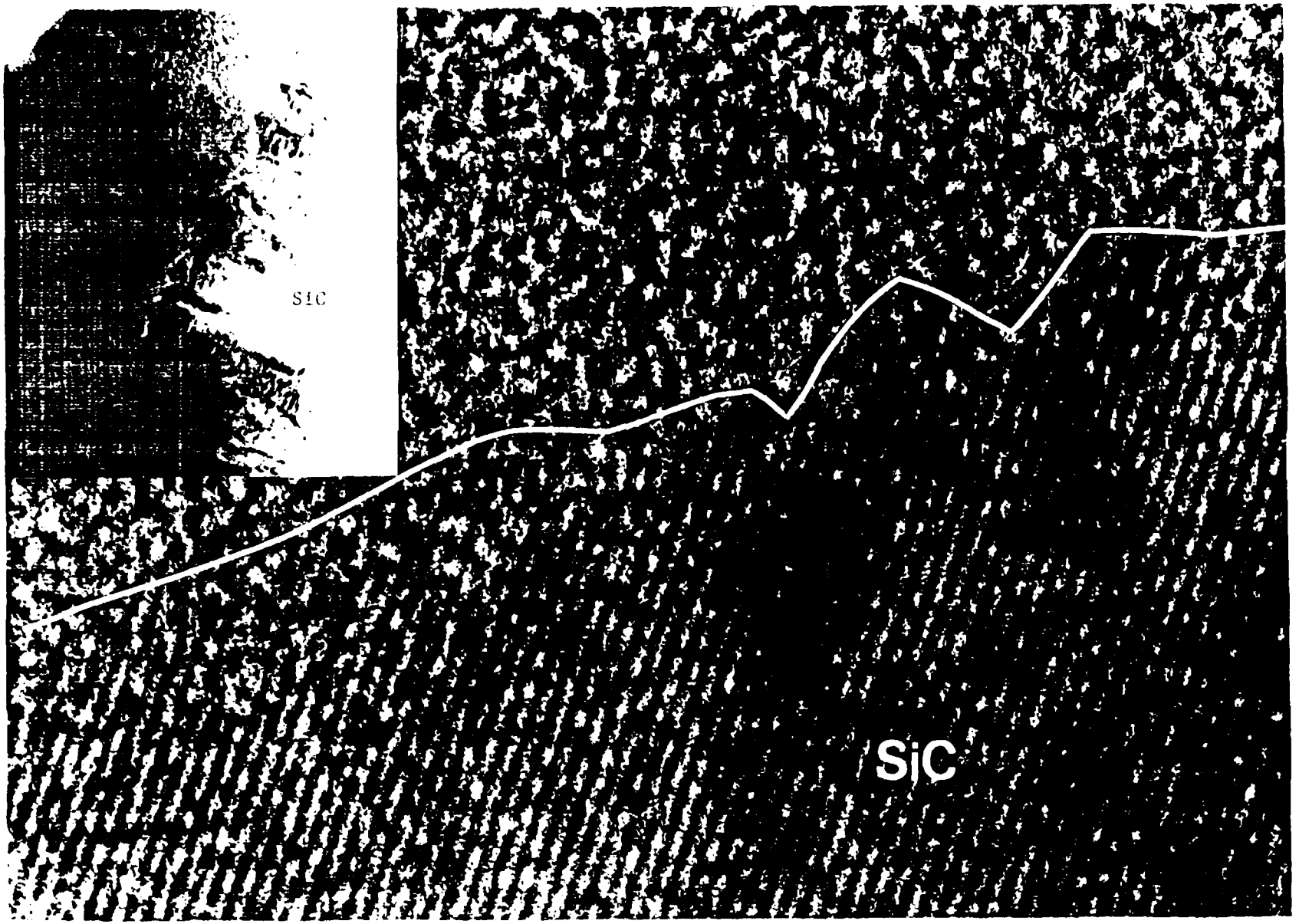

Figure 11 High-resolution TEM image of the SiC/amorphous interface in an as-received reinforcement. A bright field TEM image of the interface is shown in the inset.

Summary

In Year 1, a significant effort was made to understand the local interfacial structure in Al alloy + SiC_w composites and the effect of these interfaces on subsequent deformation and cyclic thermal behavior of the composites. These studies are expected to be completed in Year 2, and the future emphasis of this program will focus on obtaining a fundamental understanding of interfaces in Ti_3Al and TiAl matrix composites with SCS6 continuous-fiber reinforcements. Initial studies are underway to determine the atomic structures of the α_2/β and α_2/γ interfaces and the internal structure and interfacial behavior of the SCS6 fibers.

SECTION 3

MECHANICAL PROPERTIES

Report No. UCB/R/87/A1048

ROLE OF SILICON CARBIDE PARTICLES IN FATIGUE CRACK GROWTH IN SiC PARTICULATE-REINFORCED ALUMINUM ALLOY COMPOSITES

JianKu Shang and R. O. Ritchie

Department of Materials Science and Mineral Engineering,
University of California, Berkeley, CA 94720

October 1987

submitted to Materials Science and Engineering

Work supported by the Air Force Office of Scientific Research
under the University Research Initiative Contract No. F49620-87-C-0017.

ROLE OF SILICON CARBIDE PARTICLES IN FATIGUE CRACK GROWTH IN SiC PARTICULATE-REINFORCED ALUMINUM ALLOY COMPOSITES

JianKu Shang and R. O. Ritchie

Department of Materials Science and Mineral Engineering,
University of California, Berkeley, CA 94720

Abstract--A study has been made of the mechanistic role of silicon carbide particles during fatigue crack propagation in powder-metallurgy 20 vol% SiC-particulate reinforced Al-Zn-Mg-Cu metal-matrix composites, with varying degrees of reinforcement-phase size. Crack growth and accompanying crack-tip shielding (principally by crack deflection, closure and bridging) are examined in peak-aged alloys over a wide spectrum of growth rates from 10^{-12} to 10^{-4} m/cycle, and are compared with corresponding behavior in the unreinforced matrix alloy. Crack growth resistance in the composites is found to be both superior and inferior to that of the unreinforced alloy, depending on how the SiC and SiC/matrix interface fractures. At low stress intensity ranges (ΔK), the predominant fracture of carbides close to the crack tip results in low levels of crack closure and rapid growth kinetics with fine SiC distributions, whereas with coarse SiC distributions the rougher fracture surface promotes crack closure from asperity wedging and improved crack-growth resistance. With increasing ΔK, the fracture of large carbides further ahead of the crack tip leads to the development of non-uniform crack fronts thereby promoting crack bridging via uncracked ligaments and an improvement in crack-growth resistance. At high ΔK levels approaching K_{Ic}, conversely, growth rates are far faster in the composites due to their low toughness. Based on these results, the overall fatigue crack growth performance of the SiC_p/Al composites compared to traditional monolithic aluminum alloys is briefly discussed.

INTRODUCTION

In recent years, the need for lighter materials with high specific strengths and stiffnesses, coupled with major advances in processing, has led to the development of numerous composite materials as serious competitors to traditional engineering alloys. Of particular interest in the aerospace and defense industry are

polymer- or ceramic-reinforced metal-matrix composites, where much effort has been directed toward designing high performance hybrid materials utilizing, in particular, aluminum and titanium alloy matrices (1,2). Where very high strength and modulus are required for specialized applications, especially at temperatures some 100 deg C or so above that normally contemplated for the corresponding monolithic alloy, the use of aligned continuous fibers or laminated sheets has been employed to induce superior, yet highly directional, properties. Conversely, for more general applications where such extreme properties are not required, metal-matrix composites reinforced with a discontinuous phase, in the form of chopped fibers, whiskers, platelets or particles, have been shown to offer essentially isotropic properties with substantially improved strengths and stiffnesses compared to unreinforced alloys (3-6). Of these "short-fiber" materials, composites based on silicon carbide (SiC) reinforced aluminum alloys are particularly attractive as fabrication can be achieved with standard metallurgical processing, such as powder metallurgy, direct casting, rolling, forging, extrusion, drilling and so forth (3). Their reported disadvantages, however, are generally poor tensile ductility, fracture toughness and fatigue resistance compared to that of the constituent matrix (5-7).

Despite the widespread impact of the potential use of metal-matrix composites in the aerospace industry, it is perhaps surprising that few systematic studies of a fundamental nature have been performed to relate mechanistically the role of composite

microstructure in controlling fracture (5,6,8-10) and fatigue (6,8,9,11-15) resistance in these materials. Accordingly, the present work is focused on investigating primary mechanisms governing the role of SiC particles in influencing fatigue crack propagation behavior in SiC-particulate reinforced P/M aluminum alloys over a wide range of growth rates from threshold to instability.

EXPERIMENTAL PROCEDURES

Materials and Microstructures

A powder metallurgy (P/M) Al-Zn-Mg-Cu matrix alloy composition, listed in Table I, was studied in this work. The alloy, which is similar to 7091 and designated ALCOA MB78, was examined in the unreinforced condition and after particulate reinforcement with a nominal 20% by volume of either coarse F-600 grade SiC_p (nominal size 16 μm) or fine F-1000 grade SiC_p (nominal size 5 μm). The composite was fabricated by blending prealloyed atomized aluminum-alloy powders with SiC particles, compacting by cold isostatic pressing, densifying to roughly theoretical density by degassing and vacuum hot pressing, and finally extruding at an extrusion ratio of 12:1 into 25 mm thick plates (10).

The extruded plates were solution treated 4 hr at 530°C, quenched in cold water, and (due to the large difference in the thermal expansion coefficients of the matrix and carbide) immediately compressed 2 to 3% by forging to minimize quenching-induced residual stresses. Subsequent peak aging (T6 condition) was performed for 24 hr at 121°C; the resulting mechanical properties (transverse

Table I. Chemical Composition in wt% of Matrix Al-Zn-Mg-Cu Alloy

Zn	Cu	Mg	Si	P	S	Zr	Al
9.44	2.50	3.33	0.14	0.14	0.17	0.08	balance

Table II. Room Temperature Mechanical Properties of Peak Aged Alloys

Alloy	Yield Strength (MPa)	Tensile Strength (MPa)	Elongation on 13 mm (%)	Reduction in Area (%)	K_{Ic}* (MPa$\sqrt{m}$)
MB78 unreinforced	520	590	10.7	35.2	33
MB78 + 20% coarse SiCp	500	560	1.8	4.9	16
MB78 + 20% fine SiCp	400	470	1.9	13.5	14

*S-T orientation.

orientation) are listed in Table II. Note the sharply decreased ductility and toughness of the composites; strength levels are not increased, however, due to the slower aging kinetics of the unreinforced alloy.

Microstructures and particle-size distributions of the SiC in these alloys are shown in Figs. 1 and 2. Quantitative metallography, using a Zeiss IBAS/SEM-IPS Image Analysis system, indicated that the coarse SiC_p composite shows a more uniform distribution of particle sizes (Weibull modulus of 2.6), with an average size of over 10 um,

as summarized in Table III. In the fine SiC_p composite, which showed a smaller matrix grain size, clustering of particles is more in evidence (Weibull modulus of 1.6), with an average particle size of ~ 6 μm. The aspect ratio of the particles is the order of 3:1. Transmission electron microscopy (Fig. 3) revealed precipitation of η' ($MgZn_2$.$Mg(CuAl)_2$) platelets (less than 50 nm in length) in the matrix and signs of small (≲ 100 nm) equilibrium η ($MgZn_2$) precipitates on SiC/matrix interfaces (16).

Table III. SiC Particle Size Distributions and Grain Sizes

Alloy	Volume Fraction* (%)	Average Size* (μm)	Standard Deviation* (μm)	Maximum Size* (μm)	Minimum Size* (μm)	Grain Size (μm)
MB78 unreinforced	0	-	-	-	-	5.0
MB78 + 20% coarse SiCp	22.5	10.5	3.4	21.8	1.7	4.8
MB78 + 20% fine SiCp	20.9	6.1	2.8	21.1	1.9	2.3

*of carbides

Fatigue and Toughness Testing

Fatigue crack propagation tests were performed at a load ratio ($R = K_{min}/K_{max}$) of 0.1 along the guidelines of ASTM standard E 647-86A, using 6.4 mm thick double-cantilever-beam DB(M_z) specimens machined in S-T orientation. Tests were conducted in controlled room

air ($22^{o}C$, 45% relative humidity) at a sinsuoidal frequency of 50 Hz, using d.c. electrical-potential methods to monitor crack length and crack mouth opening compliance measurements (using a clip gauge) to measure (global) crack closure (17). The latter technique was used *in situ* to determine the closure stress intensity, K_{cl}, defined at first contact of the crack surfaces on unloading. Data were obtained over a wide spectrum of growth rates, from 10^{-12} to 10^{-4} m/cycle, with fatigue thresholds (ΔK_{TH}) approached under automated stress-intensity control at a normalized K-gradient of -0.2 per mm of crack extension. Growth-rate behavior is described both in terms of the nominal and effective stress-intensity ranges, given respectively by $\Delta K = K_{max} - K_{min}$ and $\Delta K_{eff} = K_{max} - K_{cl}$, computed using the K solution of Srawley et al. (18).

Plane-strain fracture toughness K_{Ic} tests were performed on identical DB(M_z) samples, along the guidelines of ASTM standard E 399. Fatigue and fracture morphology was examined in the scanning electron microscope and from crack-path profiles, obtained by metallographic sectioning at specimen mid-thickness on nickel-plated fracture surfaces or cracks previously impregnated with epoxy. Measurements of the size and proportion of cracked and decohered SiC particles involved in crack advance were carried out using X-ray (EDAX) mapping and direct-counting techniques on both fracture surfaces and crack-path profiles.

RESULTS

The variation in fatigue crack growth rates, da/dN, for the two SiC_p/Al composites is shown as a function of ΔK in Fig. 4, and compared with results for the unreinforced alloy. Three distinct regimes of behavior are evident. At near-threshold levels below $\sim 10^{-8}$ to 10^{-9} m/cycle, growth rates are over two orders of magnitude faster, and the threshold $\sim$ 28% lower, in the composite with the fine SiC particle distribution; near-threshold growth rates for the unreinforced alloy and coarse SiC_p/Al composite are similar. With increasing ΔK levels in the intermediate regime, growth rates become progressively slower in the composites, particularly in the coarse SiC_p/Al material, compared to the unreinforced alloy. At high growth rates above $\sim 10^{-6}$ m/cycle, conversely, where ΔK levels approach instability (i.e., as $K_{max} \rightarrow K_{Ic}$), the trend is reversed and growth rates become much faster in the composites.

The corresponding variation in K_{cl} values, plotted in Fig. 5, illustrates far lower crack-closure levels in the fine SiC_p/Al composite, consistent with its low ΔK_{TH} value; closure levels are 2 to 4 times higher in the coarse SiC_p/Al composite and the unreinforced alloy. After correcting for closure, effective fatigue threshold values are actually higher in both composites, namely 0.8 MPa$\sqrt{m}$ in the unreinforced alloy and 1.9 and 1.3 MPa$\sqrt{m}$ in the fine and coarse SiC_p/Al materials, respectively.

Fatigue fracture surface morphologies at low ΔK levels ($\sim$ 3.5-4.5 MPa$\sqrt{m}$) appear similar for the unreinforced alloy and coarse

SiC_p/Al composite, although approximately 13% of the composite surface is covered with either cracked or decohered SiC particles (Fig. 6a,c). Corresponding fatigue surfaces for the fine SiC_p/Al composite are far less rough, and contain a higher proportion ($\sim$ 18%) of SiC particles (Fig. 6e). At higher ΔK levels ($\sim$ 7-10 MPa$\sqrt{m}$), fracture morphologies of both composites appear essentially unchanged (Fig. 6d,f). However, the area fraction of SiC particles is clearly increased with increasing ΔK (to a maximum of $\sim$ 22% at ΔK = 10 MPa$\sqrt{m}$), as illustrated by X-ray mapping of the Si distribution on the fatigue fracture surfaces at different ΔK levels (Fig. 7).

Final (overload) fracture surfaces are shown in Fig. 8. The fracture surface of the unreinforced alloy consists primarily of hollows (of roughly grain-size dimensions), within which small dimples are located. In the composite, conversely, the smaller dimples, which represent ductile fracture in the matrix, are interdispersed between (generally) cracked SiC particles. The area fraction of SiC particles is far higher than in the microstructure and during fatigue (i.e., $\sim$ 31 and 35% in the coarse and fine SiC_p/Al composites, respectively). Thus, in contrast to results reported for SiC-particulate reinforced 2124 alloys (19), this suggests that the crack in the present composites does not follow a random path through the matrix but rather seeks out the carbides during final fracture.

Corresponding crack-path profiles (at mid-thickness) for both fatigue and overload fracture surfaces in the composites are shown in

Fig. 9. Measurements of the line fraction of cracked SiC particles along the fatigue-crack path are compared in Table IV with the area fraction of cracked or decohered particles on the fracture surface and the volume fraction in the microstructure. At low ΔK levels, it is apparent that in the coarse SiC_p/Al composite, the crack shows some tendency to avoid SiC particles with approximately $\sim$ 9% of the crack path associated with the fracture of SiC particles and $\sim$ 4% with decohesion (Fig. 9a,b). In the fine SiC_p/Al composite, again few SiC particles decohere; at both low and high ΔK levels, the majority of particles seen on the fracture surface are cracked by the fatigue process (Fig. 8c,d). In both composites, however, the proportion of cracked SiC particles increases with increasing ΔK and approaches the proportion of SiC in the microstructure, indicating that the SiC has less effect on crack path in this regime. The size distribution of cracked SiC particles along the crack path are compared to the average particle sizes in the microstructure in Table V. In general, there is no preference for the cracking of a particular particle size during fatigue crack growth, except in the fine SiC_p/Al composite at low ΔK levels where the larger SiC particles appear to be cracked preferentially (e.g., see Fig. 9c,d).

Close examination of the fatigue crack-path profiles in the composites additionally revealed the presence of uncracked ligaments along the crack length, primarily at ΔK levels above $\sim$ 5 $MPa\sqrt{m}$ where the main fatigue crack was growing out of broken SiC particles (Fig. 10b). This phenomenon was particularly noticeable in the coarse

Table IV. Quantitative Analysis of SiC Particles

Alloy	% SiC in Microstructure	% Cracked or Decohered SiC on Fracture Surface		% Cracked SiC on Crack Path	
		low ΔK^1	high ΔK^2	low ΔK^1	high ΔK^2
MB78 + 20% coarse SiCp	22.5	12.7	21.3	9.0	17.9
MB78 + 20% fine SiCp	20.9	17.7	21.9	14.0	20.0

$^1\Delta K$ = 3.5-4.5 MPa$\sqrt{m}$
$^2\Delta K$ = 7-10 MPa$\sqrt{m}$

Table V. Quantitative Analysis of Size Distribution of SiC Particles

Alloy	Ave. Size of SiC in Microstructure (μm)	Ave. Size of Cracked SiC on Fracture Surface (μm)	
		low ΔK^1	high ΔK^2
MB78 + 20% coarse SiCp	10.5 $\pm$ 3.4	11.8 $\pm$ 3.4	9.8 $\pm$ 2.8
MB78 + 20% fine SiCp	6.1 $\pm$ 2.8	10.7 $\pm$ 5.6	6.9 $\pm$ 4.9

$^1\Delta K$ = 3.5-4.5 MPa$\sqrt{m}$
$^2\Delta K$ = 7-10 MPa$\sqrt{m}$

SiC_p/Al alloy ($\sim$17% line fraction of uncracked ligaments compared to $\sim$ 13% in fine SiC_p/Al alloy), and appeared to be associated with the development of non-uniform crack fronts due to the fracture of SiC particles ahead of the main crack tip. Although serial sectioning revealed that the main fatigue crack remained continuous in three

dimensions, such uncracked ligaments in any one two-dimensional section clearly tend to inhibit crack opening and thus provide a crack-bridging mechanism for shielding the crack from the externally applied stresses.

DISCUSSION

The results of this work have indicated that the fatigue crack growth performance of 20 vol% SiC-particulate reinforced Al-Zn-Mg-Cu composites, relative to the unreinforced matrix alloy, depends largely on the interaction of the SiC particles with the fatigue fracture process. The nature of this interaction involves whether cyclic crack growth in the softer matrix causes fracture of, or crack deflection around, the harder SiC particles, which in turn depends mechanically on the stress-intensity level and microstructurally on the absolute size and size distribution of the particles (for a constant volume fraction of SiC). The result of this interaction is a series of mechanisms, i) which can decelerate crack growth, such as the high levels of crack closure* induced near ΔK_{TH} by rough fracture surfaces in part from decohesion around large particles (Fig. 10a), and ii) which can both accelerate and decelerate crack growth, such as the mutual competition of the cracking of particles ahead of the crack tip (which enhances growth rates), and the consequent development of crack bridging* from the uncracked ligaments left

*Crack closure and bridging are mechanisms of crack-tip shielding, where crack advance is impeded by mechanisms which act to lower the local "crack driving force" experienced in vicinity of the crack tip (17,20).

behind the tip (which impedes growth rates) (Fig. 10b). We now examine each mechanism in turn.

The brittle fracture of SiC particles in the plastic zone ahead of the growing fatigue crack clearly generates a fast increment of crack extension which provides a contribution to the overall growth rates. Statistically, the process is similar to that described for the fracture of iron carbides ahead of monotonically-loaded cracks (21-23). Essentially, on the assumption that the carbide-particle fracture is (maximum principal) stress-controlled, the "strength" S of each particle is roughly inversely proportional to the square root of its characteristic dimension d_p (23,24):

$$S = [\pi E\, G_{pm}/2(1 - \nu^2)d_p]^{\frac{1}{2}} \qquad (1)$$

where E is Young's modulus, ν is Poisson's ratio, and G_{pm} is the critical strain-energy release rate for dynamic propagation of the carbide microcrack into the matrix. Thus, for a hypothetical distribution of constant-sized particles, the maximum probability of particle fracture is located at the site where the tensile stresses are highest, i.e., <u>at</u> the fatigue crack tip, or more precisely a couple of crack-tip opening displacements (in this case $\sim$ 100 nm) from the tip. For a distribution of particle sizes, conversely, the maximum probability of particle fracture moves <u>ahead</u> of the crack tip, due to the fact that although the highest stresses are at the tip, the probability of finding a larger, more crackable or "eligible", carbide increases with the sampling volume, i.e., with

distance ahead of the crack tip within the plastic zone of the fatigue crack (21). Assuming that the crack-tip stress distribution at K_{max} can be described by the Hutchinson, Rice, Rosengren (HRR) nonlinear-elastic stress distribution (25,26), this distance is given by (20):

$$r^* = \frac{n+1}{2\pi}\left[\frac{\tilde{\sigma}^2}{I_n}\right]\left[\frac{2n+3-m}{2n+3}\right]^{n+1}\left(\frac{K_{max}}{\sigma_o}\right)^2\left(\frac{\sigma_o}{S_u}\right)^{n+1} \qquad (2)$$

where σ_o is the yield stress, n is the strain-hardening coefficient, m is the Weibull modulus, S_u is the lower bound strength (of the largest SiC particle), and I_n and $\tilde{\sigma}$ are dimensionless functions in the HRR solution. Where Eq. (2) has been evaluated, e.g., for the fracture of iron carbides in a ferrite matrix, r^* takes values ranging from several grain diameters to a large fraction of the plastic zone size (21).

At low stress intensities, although the accelerating effect of particle fracture is potentially most potent as the overall fatigue crack growth rates are very low, the sampling volume and r^* are small. The fracture of SiC will thus be inhibited or confined to particles in the immediate vicinity of the crack tip. With increasing K_{max}, however, the increase in plastic-zone size provides a large increase in sampling volume with the result that the fracture of large SiC particles located some distance ahead of the crack tip becomes more probable.

At near-threshold levels below $\sim 10^{-9}$ m/cycle, the extremely small (sub-micron) crack-tip opening displacements associated with fatigue crack advance implies that crack-tip shielding via the wedging of crack-surface asperities (roughness-induced closure (27-29)) may become dominant (Fig. 10a). Accordingly, optimum near-threshold fatigue crack growth properties (for "long cracks" (17)) are generally achieved with coarser microstructures which induce rougher fracture surfaces, as reported for numerous unreinforced alloys (e.g., refs. 29-33). Since fracture-surface roughness will primarily be a function of grain size and to a lesser extent carbide size, it is to be expected that the coarser-grained materials, namely the coarse SiC_p/Al composite and the unreinforced alloy, will develop rougher fracture surfaces (Fig. 6), higher levels of crack closure (Fig. 5) and show correspondingly lower near-threshold growth rates (Fig. 4), than the fine SiC_p/Al composite.

With increasing ΔK, and hence increasing crack-tip opening displacements, the wedging effect must diminish, leading to smaller differences in crack-closure levels and corresponding growth rates (20), consistent with results in Figs. 4 and 5. Above $\sim 10^{-8}$ m/cycle, however, growth rates again diverge, with the composites (especially the coarse SiC_p/Al) showing progressively slower growth rates compared to the unreinforced alloy. As the sampling volume is increasing with a consequent increase in the incidence of carbide fracture (Table IV), this might appear inconsistent. However, with increasing r^*, the generation of microcracks in SiC particles some

distance ahead of the crack tip, and the propagation of these cracks into the adjacent matrix, can result in non-uniform crack fronts and uncracked ligaments in the wake of the crack tip. This is illustrated in Fig. 10b, where segments of the major crack growing out of the broken SiC particles are separated by unbroken ligaments. The ligaments act as crack bridges which oppose crack opening, thereby generating a potent source of crack-tip shielding. Other examples of ligament bridging have been reported for brittle fracture in steels and alumina (34,35).

At high growth rates above typically 10^{-6} m/cycle, rates of crack propagation now become faster in the composites compared to the unreinforced alloy. However, such behavior represents the acceleration in growth rates characteristic of stress-intensity levels approaching instability or K_{Ic} (36), and reflects the far lower fracture toughness values of the composite alloys.

Thus, it is apparent that the fatigue crack growth properties of SiC-particulate reinforced Al-Zn-Mg-Cu composites are generally superior to the unreinforced matrix alloy, but depend critically on the range of growth rates of interest. It is therefore imperative to characterize the fatigue performance of such materials over a broad spectrum of growth rates (unlike many previous studies) before conclusions can be drawn. Compared to traditional monolithic high strength I/M aluminum alloys, however, the composites show comparable properties to 7150-T651, yet apart from behavior at near-threshold

levels, they are far inferior to the more fatigue-resistant alloys, namely 2124-T351 and the lithium-containing 2090-T8E41 (Fig. 11).

CONCLUSIONS

Based on an investigation of the mechanistic role of SiC particles during fatigue crack growth (at R = 0.1) in 20 vol% SiC-particulate reinforced P/M Al-Zn-Mg-Cu metal-matrix composites, the following conclusions can be made:

1. The fatigue crack growth performance of SiC_p/Al composites with either fine or coarse SiC particle distributions, relative to that of the unreinforced constituent matrix alloy, depends critically on interaction between cyclic crack growth in the softer matrix and the decohesion, or more importantly brittle fracture, of harder SiC particles. This interaction varies with stress-intensity level and the size distribution of the carbides.

2. Whereas at low ΔK levels the fatigue crack path in either composite shows some tendency to avoid SiC particles (i.e., area fraction of SiC on fracture surface is less than volume fraction in microstructure), at higher ΔK levels these fractions are similar indicating that the carbides have less influence on crack path. SiC particle fractures exceed SiC/matrix decohesions by at least 2.5:1 along the crack path at low ΔK, rising to ~10-15:1 with increasing stress-intensity range.

3. At low, near-threshold, stress-intensity ranges ($da/dN \leq 10^{-9}$ m/cycle), crack growth rates in the fine SiC_p/Al composite are faster, and ΔK_{TH} values ~ 28% lower, compared to the unreinforced

alloy and the coarse SiC_p/Al composite. This is attributed to far lower levels of (roughness-induced) crack closure in the fine SiC_p/Al composite, consistent with experimental K_{cl} measurements, sub-micron CTOD levels and observations of smoother fracture surfaces.

4. At higher stress intensity ranges ($10^{-8} \leq da/dN \leq 10^{-6}$ m/cycle), growth rates become progressively slower in the composites compared to the unreinforced alloy. This is attributed to the mutual competition of SiC particle fracture ahead of the crack tip (which enhances crack growth), and crack bridging from the resulting uncracked ligaments behind the crack tip (which retards crack growth). As statistically larger carbides are involved in the coarse Si_p/Al composite, ligament bridging is more effective in this microstructure.

5. At high stress intensities approaching instability or K_{Ic} ($da/dN \gtrsim 10^{-6}$ m/cycle), growth rates are far faster in both composites compared to the unreinforced alloy, due to their much lower fracture toughness values.

6. In general, the SiC_p/Al composites show comparable fatigue crack growth properties to unreinforced I/M 7150-T651 aluminum alloy, yet apart from behavior at near-threshold levels, they are far inferior to unreinforced I/M 2124-T351 and 2090-T8E41 alloys.

Acknowledgments--This work was supported by the Air Force Office of Scientific Research under the University Research Initiative Contract No. F49620-87-C-0017 to Carnegie-Mellon University. The authors would like to thank Dr. A. H. Rosenstein for his support,

W. H. Hunt, Jr. and Dr. R. J. Bucci of ALCOA for supplying the alloys and for many helpful discussions, Dr. W. Yu, A. Nguyen and L. H. Edelson for experimental assistance, and Madeleine Penton for help in preparing the manuscript.

REFERENCES

1. A. K. Dhingra, J. Met., **38** (1986) 17.

2. R. C. Forney, J. Met., **38** (1986) 18.

3. A. K. Dhingra, S. G. Fishman and S. D. Karmarkar, J. Met., **33** (1981) 12.

4. R. J. Arsenault, Mater. Sci. Eng., **64** (1984) 171.

5. C. R. Crowe, R. A. Gray, and D. F. Hasson, in W. Harrigan, J. Strife and A. K. Dhingra (eds.), Proc. 5th Intl. Conf. on Composite Materials, The Metallurgical Society of AIME, Warrendale, PA, 1985, p. 843.

6. S. V. Nair, J. K. Tien and R. C. Bates, Int. Met. Rev., 30 (1985) 275.

7. D. L. McDanels, Metall. Trans. A, **16A** (1985) 1105.

8. W. A. Logsdon and P. K. Liaw, Eng. Fract. Mech., **24** (1986) 737.

9. D. L. Davidson, "Fracture Characteristics of Al-4% Mg Mechanically Alloyed with SiC", Southwest Research Institute, San Antonio, TX (1986).

10. J. J. Lewandowski, C. Liu and W. H. Hunt, in M. Kumar, K. Vedula and A. M. Ritter (eds.), Powder Metallurgy Composites, The Metallurgical Society of AIME, Warrendale, PA, 1987.

11. C. R. Crowe and D. F. Hasson, in R. C. Grifkins (ed.), Strength of Metals and Alloys - V, Pergamon Press, Oxford, U.K., vol. 2, 1982, p. 859.

12. D. F. Hasson and C. R. Crowe, in W. Harrigan, J. Strife and A. K. Dhingra (eds.), Proc. 5th Intl. Conf. on Composite Materials, The Metallurgical Society of AIME, Warrendale, PA, 1985, p. 147.

13. D. R. Williams and M. E. Fine, in W. Harrigan, J. Strife and A. K. Dhingra (eds.), Proc. 5th Intl. Conf. on Composite Materials, The Metallurgical Society of AIME, Warrendale, PA, 1985, p. 639.

14. S. S. Yau and G. Mayer, Mater. Sci. Eng., **82** (1986) 45.

15. T. E. Steelman, A. D. Bakalyar and L. Konopka, "Aluminum Matrix Composite Structural Design Development", Technical Report AFWAL-TR-86, Rockwell Intl. Corp., Los Angeles, CA (1986).

16. L. H. Edelson, unpublished work, University of California, Berkeley, CA, (1987).

17. R. O. Ritchie and W. Yu, in R. O. Ritchie and J. Lankford (eds.), Small Fatigue Cracks, The Metallurgical Society of AIME, Warrendale, PA, 1986, p. 167.

18. J. E. Srawley and B. Gross, Mat. Res. Stand., **7** (1967) 155.

19. C. P. You, A. W. Thompson and I. M. Bernstein, Scripta Met., **21** (1987) 181.

20. R. O. Ritchie, in M. G. Yan, S. H. Zhang and Z. M. Zheng (eds.), Mechanical Behavior of Materials - V, Pergamon Press, Oxford, U. K., 1987.

21. Tsann Lin, A. G. Evans and R. O. Ritchie, J. Mech. Phys. Solids, **34** (1986) 477.

22. Tsann Lin, A. G. Evans and R. O. Ritchie, Acta Met., **34** (1986) 2205.

23. Tsann Lin, A. G. Evans and R. O. Ritchie, Metall. Trans. A, **18A** (1987) 641.

24. D. Curry and J. F. Knott, Met. Sci., **12** (1978) 511.

25. J. W. Hutchinson, J. Mech. Phys. Solids, **16** (1968) 13.

26. J. R. Rice and G. R. Rosengren, J. Mech. Phys. Solids, **16** (1968) 1.

27. N. Walker and C. J. Beevers, Fat. Eng. Mat. Struct., **1** (1979) 135.

28. K. Minakawa and A. J. McEvily, Scripta Met., **6** (1981) 633.

29. S. Suresh and R. O. Ritchie, Metall. Trans. A, **13A** (1982) 1627.

30. J. L. Robinson and C. J. Beevers, Met. Sci. J., 7 (1973) 153.

31. S. Suresh and R. O. Ritchie, in D. L. Davidson and S. Suresh (eds.), Fatigue Crack Growth Threshold Concepts, The Metallurgical Society of AIME, Warrendale, PA, 1984, p. 227.

32. G. T. Gray, A. W. Thompson and J. C. Williams, Metall. Trans. A, **14A** (1983) 421.

33. J. E. Allison and J. C. Williams, in G. Lütjering, U. Zicker and W. Bunk (eds.), Titanium Science and Technology, DGM Publishers, vol. 4, 1984, p. 2243.

34. A. R. Rosenfield and B. S. Majumdar, Metall. Trans. A, **18A** (1987) 1053.

35. Y.-W. Mai and B. R. Lawn, J. Amer. Cer. Soc., **70** (1987) 289.

36. R. O. Ritchie and J. F. Knott, Acta Met., **21** (1973) 639.

37. E. Zaiken and R. O. Ritchie, Mater. Sci. Eng., **70** (1985) 151.

38. K. T. Venkateswara Rao, W. Yu and R. O. Ritchie, Metall. Trans. A, **18A** (1987).

39. R. O. Ritchie, W. Yu, A. F. Blom and D. K. Holm, Fract. Fat. Eng. Mat. Struct., **10** (1987) in press.

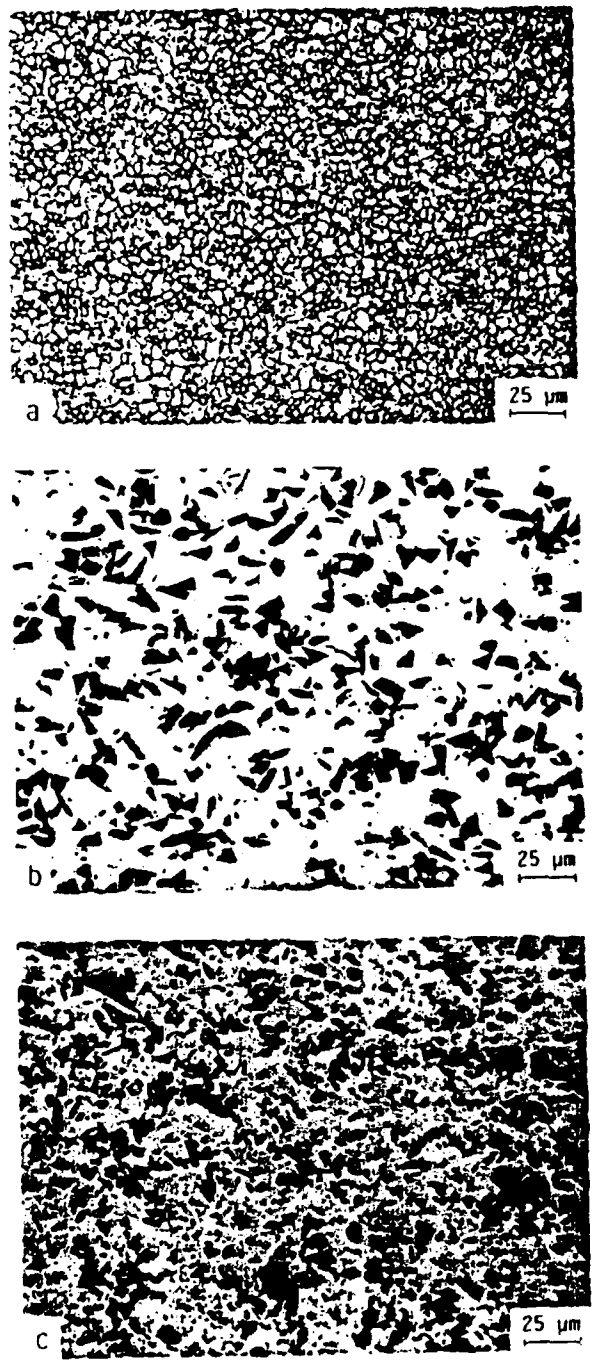

Fig. 1: Optical micrographs of the peak-aged microstructures of a) unreinforced matrix alloy, b) coarse SiC_p/Al composite, and c) fine SiC_p/Al composite.

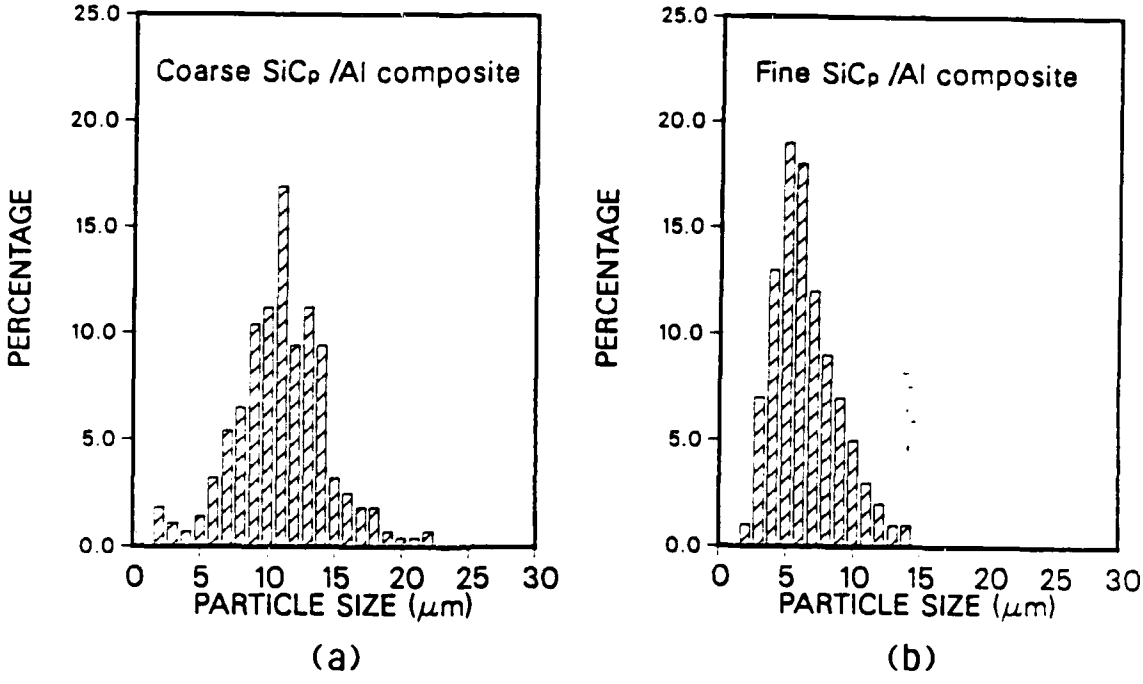

Fig. 2: Distribution of SiC particle sizes in the microstructure of a) coarse SiC_p/Al and b) fine SiC_p/Al composites.

Fig. 3: Transmission electron micrograph of the microstructure of coarse SiC_p/Al composite in the peak-aged condition (courtesy of L. H. Edelson).

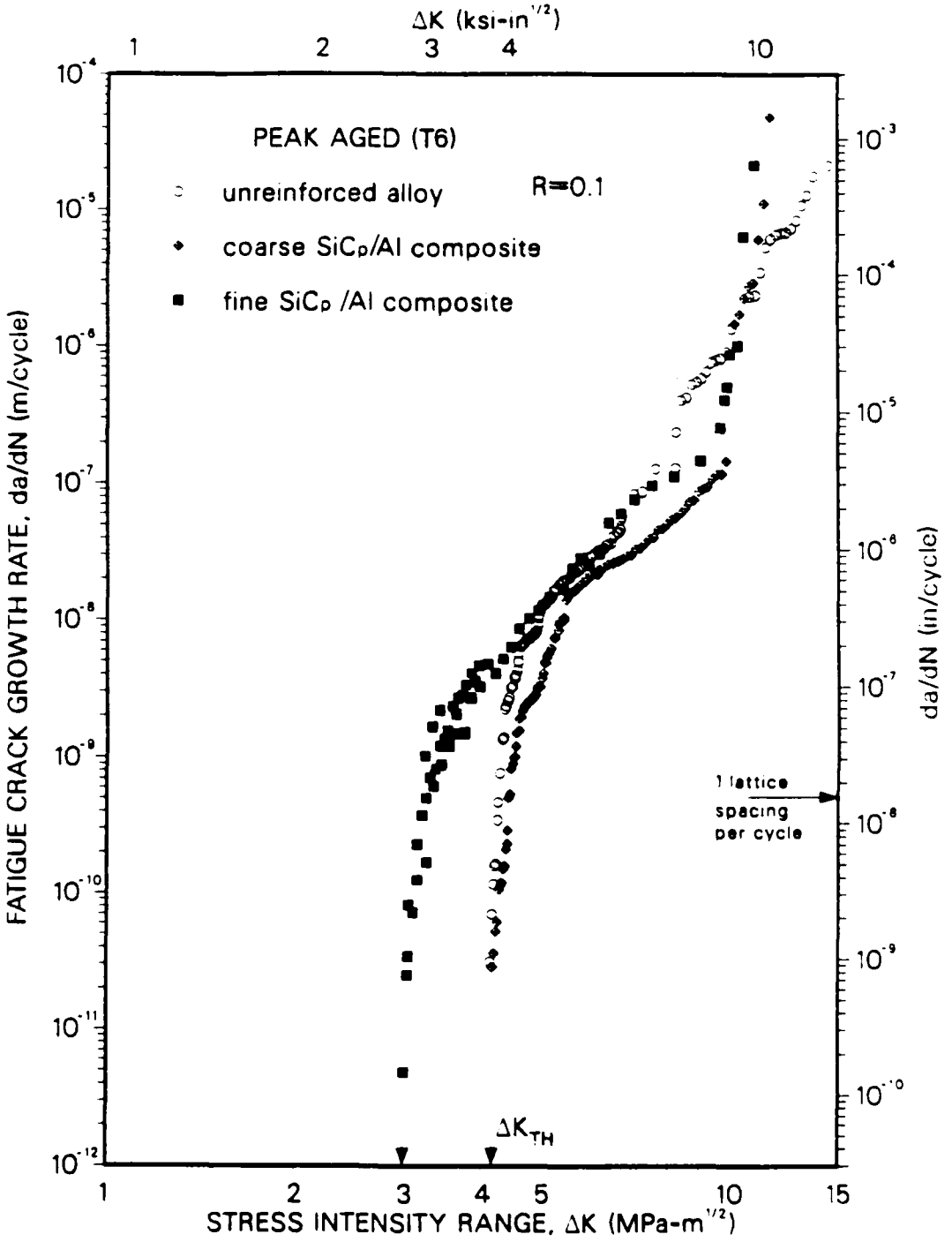

Fig. 4: Variation in fatigue crack propagation rates (da/dN) with nominal stress-intensity range (ΔK) at R = 0.1 for the fine and coarse SiC_p/Al composites and unreinforced matrix alloy in the peak-aged condition.

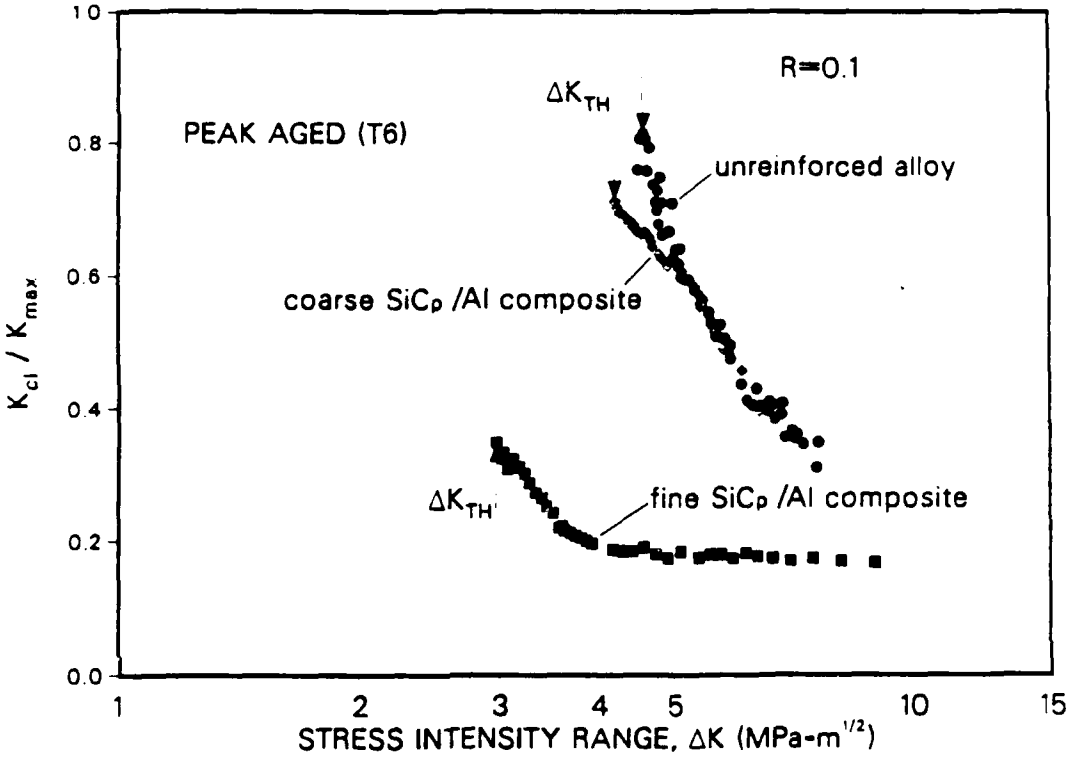

Fig. 5: Variation in crack closure, in terms of the ratio of closure to maximum stress intensity (K_{cl}/K_{max}), as a function of ΔK for peak-aged fine and coarse SiC_p/Al composites and unreinforced matrix alloy, corresponding to the growth-rate data in Fig. 3.

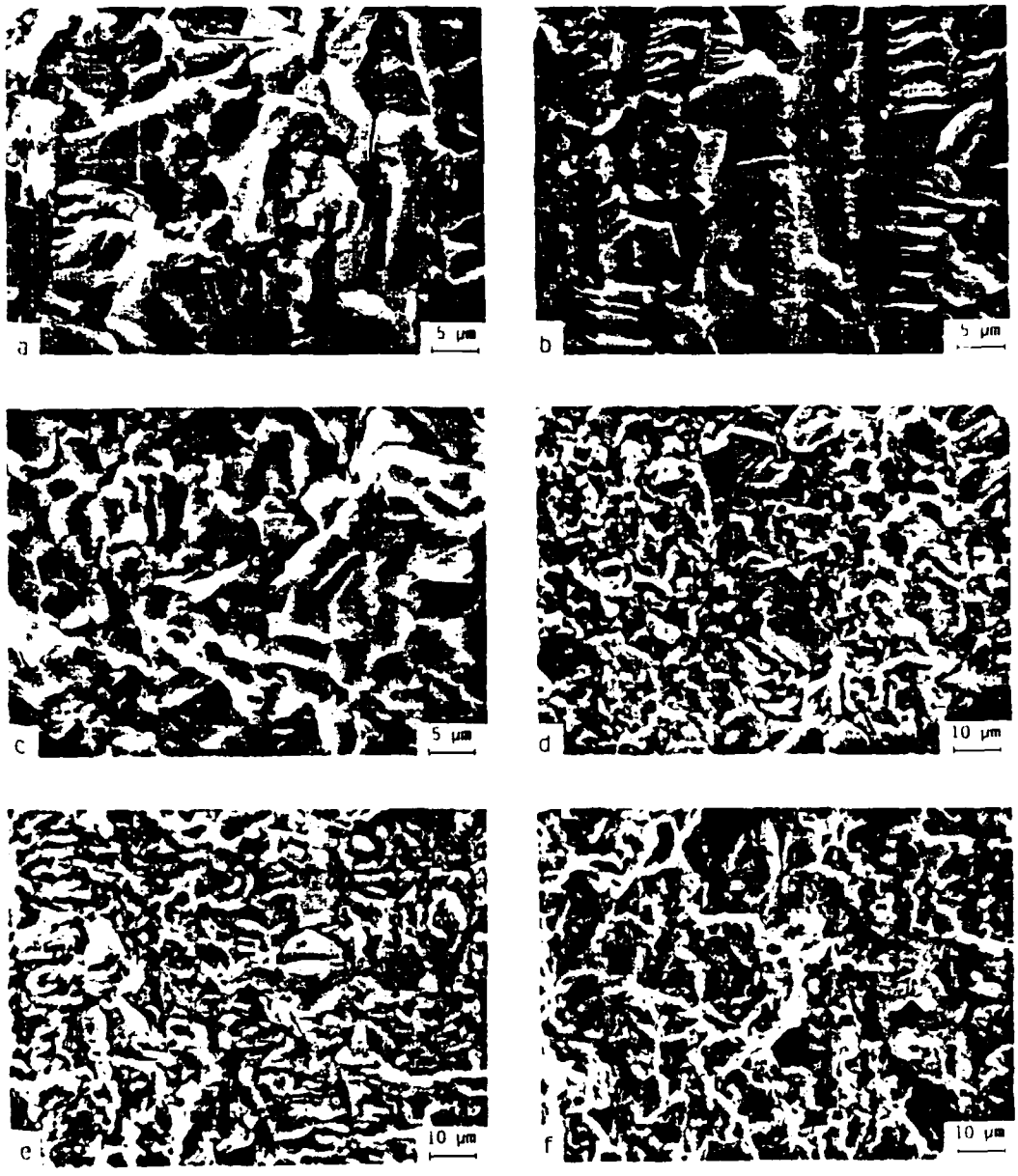

Fig. 6: Scanning electron micrographs of fatigue fracture surfaces in a,b) unreinforced matrix alloy, c,d) coarse SiC_p/Al composite, and e,f) fine SiC_p/Al composite. Fractographs a,c,e) refer to behavior at low ΔK levels (~ 3.5-4.5 MPa,$\sqrt{m}$); b,d,f) to high ΔK levels (~ 7-10 MPa,$\sqrt{m}$).

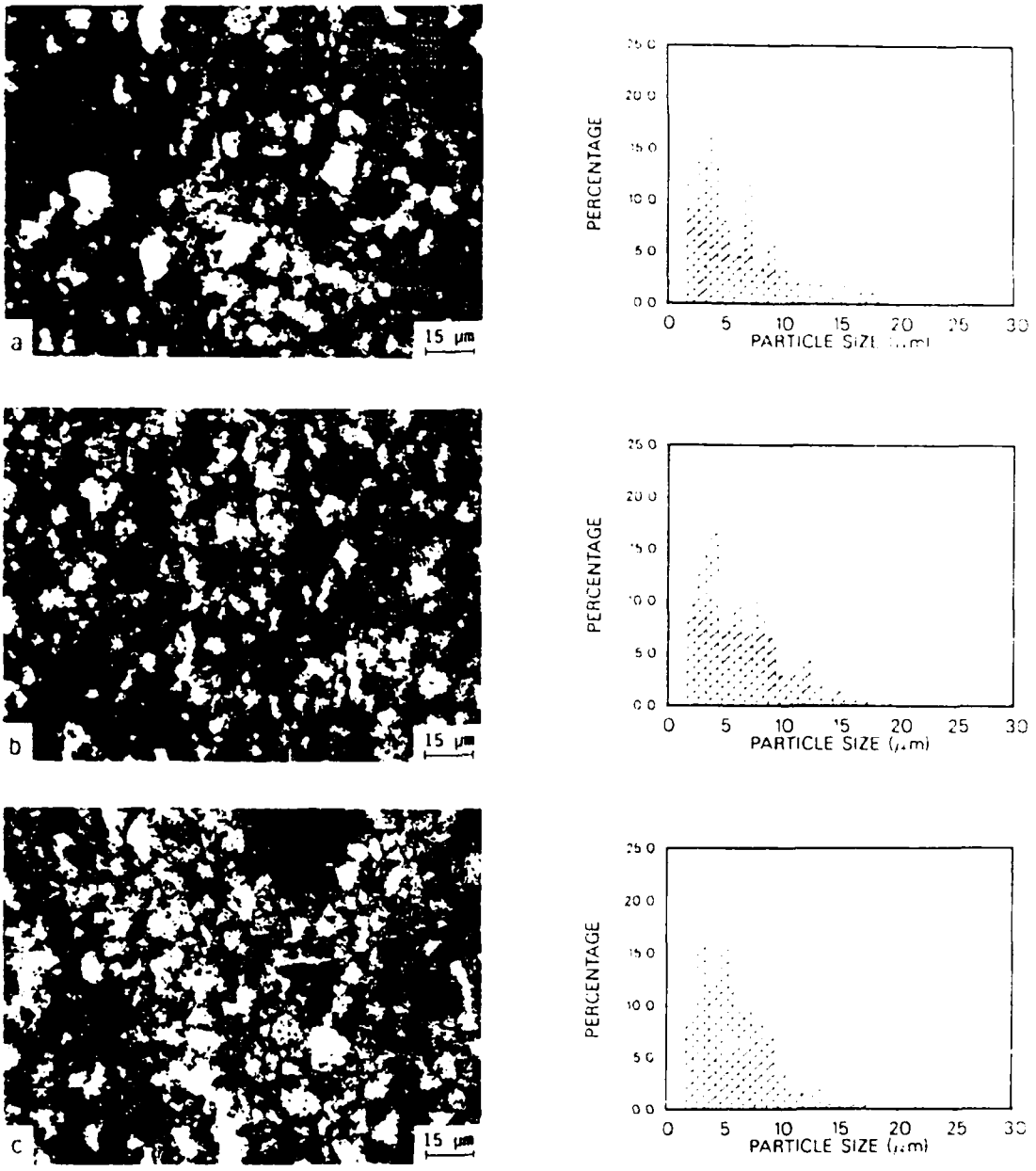

Fig. 7: Distribution of SiC particles on fatigue fracture surface of fine SiC_p/Al composite at ΔK levels of a) 3.5 MPa$\sqrt{m}$, 7 MPa$\sqrt{m}$, and c) 10 MPa$\sqrt{m}$, as illustrated by X-ray mapping of Si on fracture surface and histograms of particle size measured from scanning electron micrographs.

AD-A189 516 HIGH-TEMPERATURE METAL MATRIX COMPOSITES(U) CARNEGIE 2/2
MELLON UNIV PITTSBURGH PA DEPT OF METALLURGICAL ENGI
A W THOMPSON ET AL 30 NOV 87 AFOSR-TR-88-0089
UNCLASSIFIED F49620-87-C-0017 F/G 11/4 NL

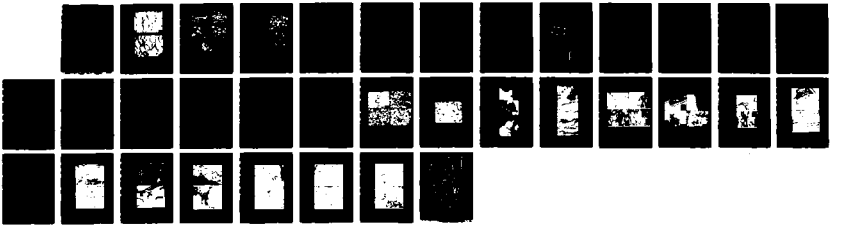

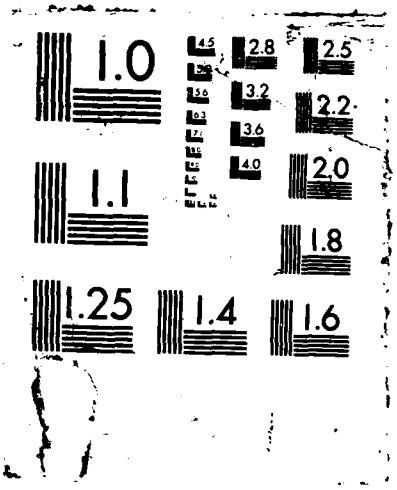
1.0
1.1
1.25
1.4
1.6
1.8
2.0
2.2
2.5
2.8
3.2
3.6
4.0

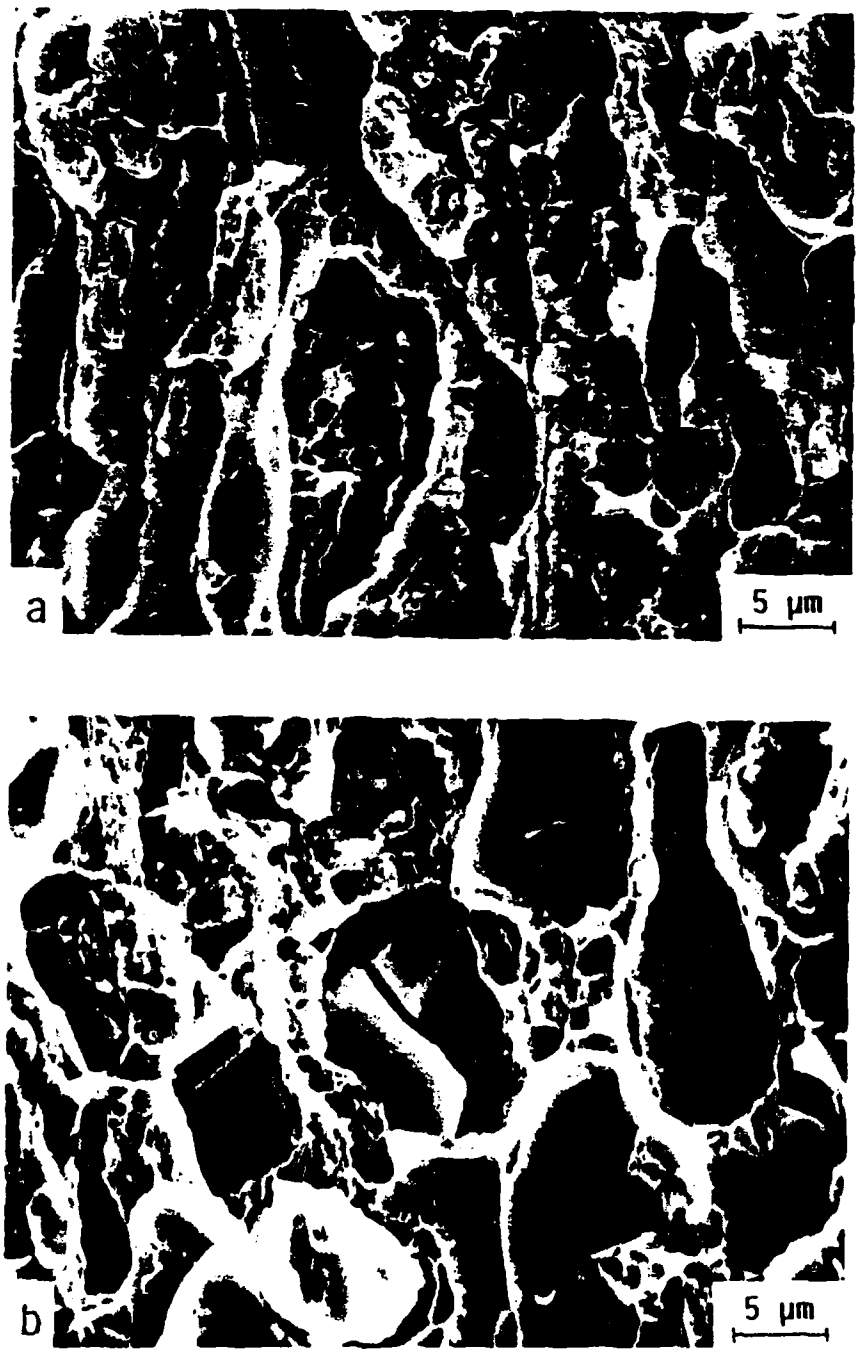

Fig. 8: Scanning electron micrographs of final overload fracture surfaces in a) unreinforced matrix alloy and b) coarse SiC_p/Al composite.

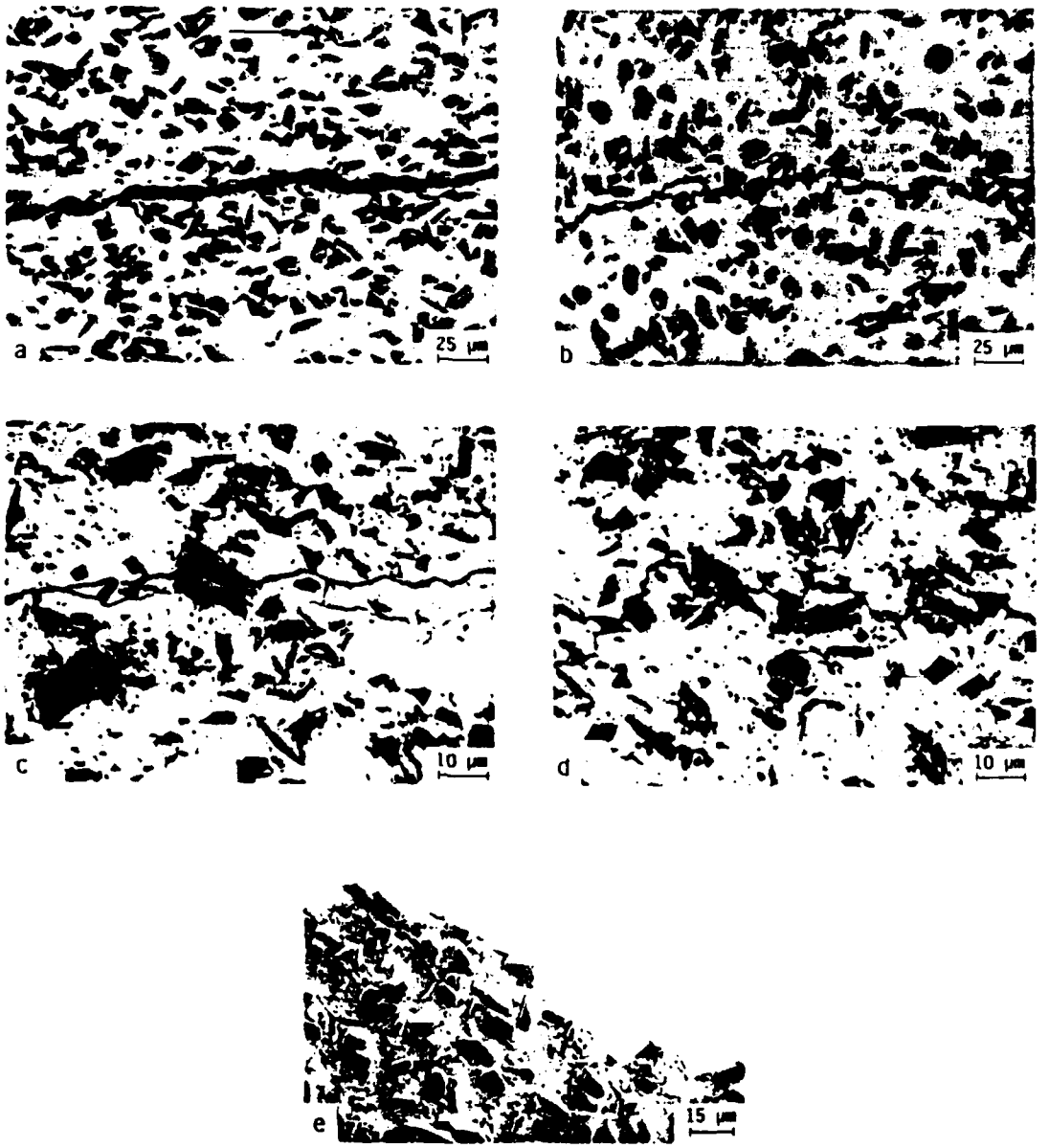

Fig. 9: Optical micrographs of crack-path profiles of fatigue cracks in coarse SiC_p/Al composite at ΔK levels of a) ~ 4.5 MPa$\sqrt{m}$, and b) ~ 9 MPa$\sqrt{m}$; of fatigue cracks in fine SiC_p/Al composite at ΔK levels of c) ~ 3.5 MPa$\sqrt{m}$, and d) ~ 9 MPa$\sqrt{m}$; and of final overload fracture in coarse SiC_p/Al composite. Arrow indicates general direction of crack growth.

a) Crack closure
via asperity wedging

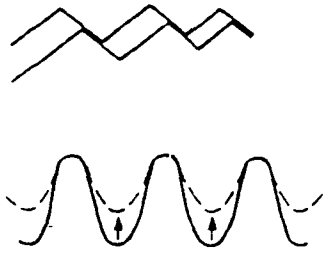

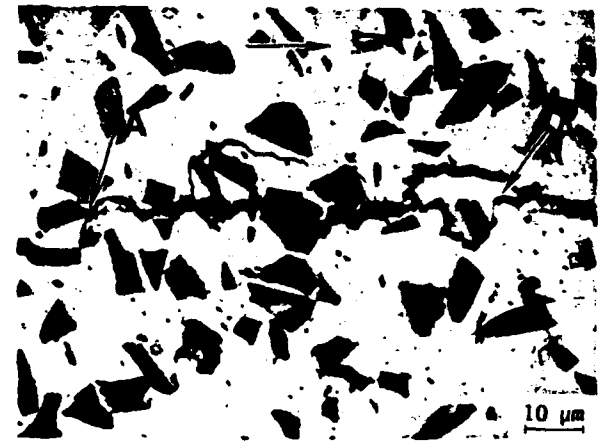

b) Crack bridging
via uncracked ligaments

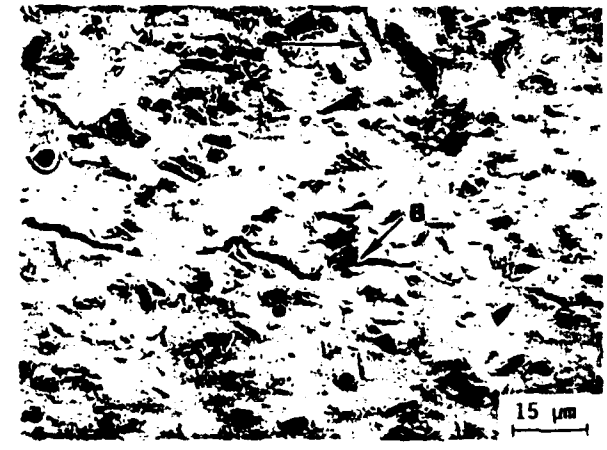

Fig. 10: Prominent mechanisms of crack-tip shielding during fatigue crack growth in SiC_p/Al composites, showing a) crack closure via asperity wedging (marked at locations A) in coarse SiC_p/Al composite at $\Delta K = 4.5$ MPa$\sqrt{m}$, and b) crack bridging via uncracked ligaments (location B) associated with cracked SiC particles in fine SiC_p/Al composite at $\Delta K = 7$ MPa$\sqrt{m}$. Horizontal arrows indicate general direction of crack growth.

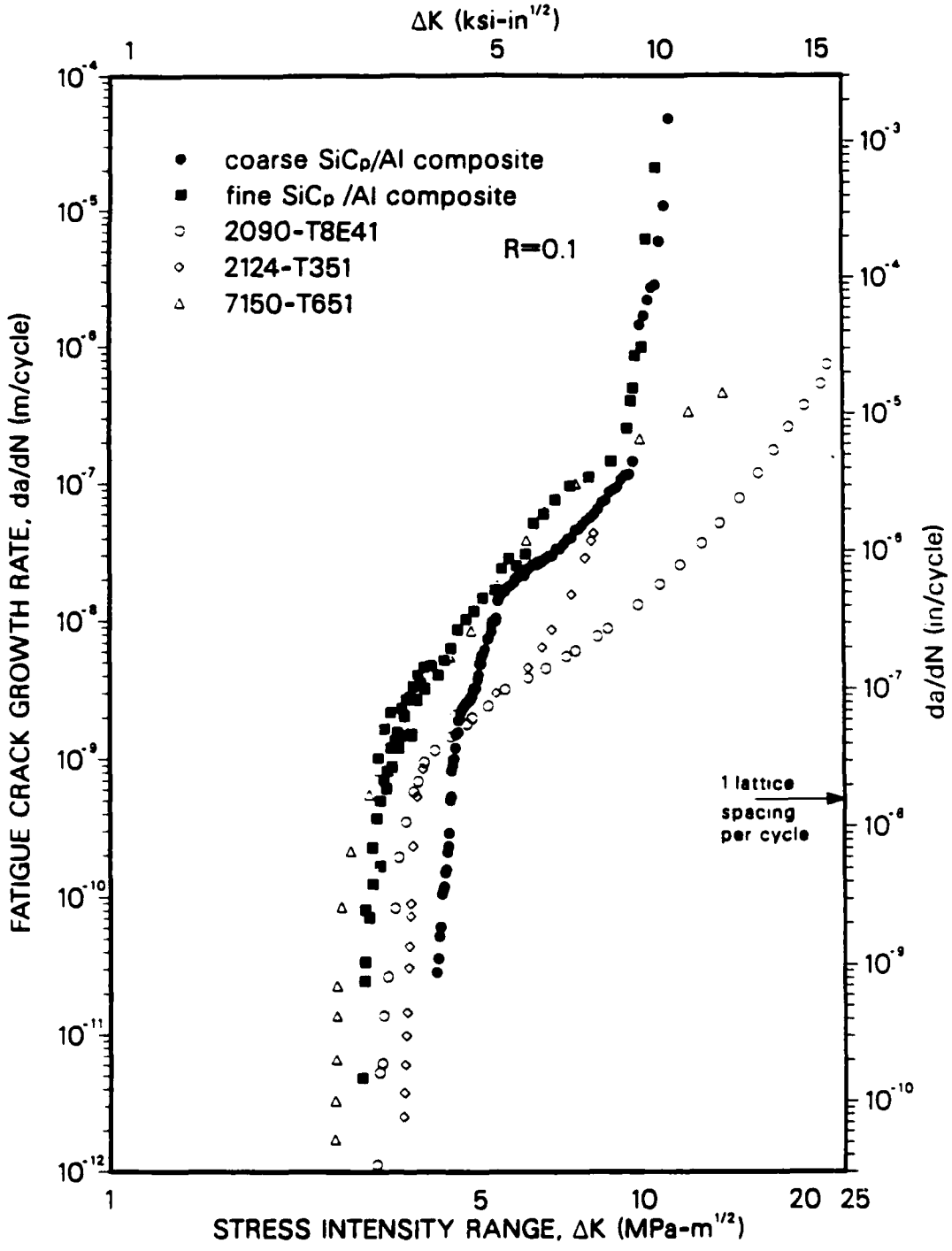

Fig. 11: Comparison of the fatigue crack growth behavior of present peak-aged coarse and fine SiC_p/Al composites with traditional 2124-T351, 7150-T651 and 2090-T8E41 high-strength aluminum alloys. Data for the monolithic I/M alloys taken from refs. 37-39.

HIGH-TEMPERATURE MECHANICAL BEHAVIOR OF COMPOSITES

TASK 5 - - A.W. THOMPSON, J.C. WILLIAMS

Understanding of high-temperature mechanical response of metal matrix composites, in terms of processing history and microstructural variables, especially the characteristics of the reinforcement-matrix interface, is essential to development of these materials for structural use. This task addresses the mechanical behavior from a micromechanistic modeling perspective, using information from the processing and characterization tasks as well as from mechanical tests within the work of Task 5. Of particular interest are residual stresses, microstructural changes during deformation, localization of deformation, fracture nucleation in either reinforcement or matrix constituent, and the development of the deformed dislocation structures in the matrix. Utilization of transmission electron microscopy, complementing the work done in Tasks 3 and 6, is essential to this work, together with the detailed mechanical testing of conventional specimens and also *in situ* tests in the scanning electron microscope (SEM) to permit observation of fracture initiation and propagation in the composite microstructure. Tasks 3 and 6 are also expected to make use of this SEM capability.

The existing evidence on mechanical performance of metal matrix composites at high temperature indicates that ductility is a strong function of local as well as macroscopic response to imposed stress or stress amplitude. To interpret this response in terms of creep rate requires detailed understanding of both composite microstructure and also of the development of dislocation structures during deformation, and neither of these is yet available except in broad outline. However, Fig. 1 shows an indication of what can be expected. The size and character of dislocation cell structures can be controlled by dispersoid spacing and distribution, in the case of the conventional dispersion-strengthened materials containing sub-micron reinforcements, and this in turn controls the mean free slip length and the flow behavior. Whether the same kind of cell structure control will occur with much larger and more widely-spaced particle or fiber reinforcements is not clear, but it seems unlikely to affect flow behavior in nearly the same fashion, since the relevant dimensions are typically tens of microns or more. The shape (or aspect ratio) of fibers, as well as the size, spacing and volume fraction of particulate reinforcement, are expected to be primary variables, along with the character of the reinforcement-matrix bond (assumed to be best if well bonded).

The 'threshold stress", if one exists for these materials, gives a stress-strain rate behavior which is strongly curved and steepens as stress nears the the threshold. This can be conceptually represented as in Figure 2, as two linear regions. For fine spacings, this is an accepted picture, and the threshold stress can be interpreted as being the same as, or derived from, the Orowan stress for dislocation bowing between

obstacles. However, when particle or fiber spacings are several to several tens of microns, the Orowan stress is negligible, and a threshold stress, if one occurs, must have other origins. It can be speculated, however, that increasing volume fraction of reinforcement would act to move the threshold stress upwards, and thereby move the creep curve to the right in Fig. 2.

Figs. 1 and 2 also suggest the further question as to the creep mechanism which operates in these materials. Mechanics analysis has suggested that the matrix, yielding first, will creep until load is transferred fully to the reinforcement phase, in the situation of creep in the matrix giving rise to a vanishingly-small tangent modulus of the matrix. However, that tangent modulus can only be small if the matrix continues to creep. Intermediate conditions of partial load transfer can be envisaged, in which a significant tangent modulus remains associated with the matrix. In that case, load would remain on the matrix, but the matrix may well be below its creep threshold (if one exists). Again, creep could cease, provided the reinforcement itself does not creep under the imposed conditions. However, experimental work is clearly necessary to examine the behavior in detail, not only to establish whether a threshold exists and whether reinforcement creep, reinforcement-matrix boundary sliding, or some other creep process takes place even in a regime in agreement with the mechanics analysis, but more importantly to establish whether some more complex phenomenon, such as matrix creep within the stress gradient near the reinforcement, can also occur. The role of thermal, mechanical or combined cycling on behavior also needs to be addressed.

As a concluding topic, the toughness of these materials at ambient and elevated temperatures is of considerable interest, particularly for intermetallic matrix composites which are expected to be limited in performance by their room-temperature toughness. For "conventional" metal matrix composites, the normal experience is that addition of reinforcement volume fraction (to accomplish increases in elastic modulus, strength, or other property of interest) tends to diminish toughness, in a competition between the increasing strength and the decreasing ductility. This occurs whether or not the reinforcement phase is well-bonded to the matrix, because of the relatively tough behavior of the matrix material. When matrix toughness is low, however, as in ceramic matrix composites, weak or zero bonding between reinforcement and matrix may provide superior toughness performance. The question then arises, as summarized in Fig. 3, whether intermetallic matrix composites will perform better with weak or with strong bonds between reinforcement and matrix. The issue may be complex if creep resistance is part of the property requirement, since there are few if any reasons to expect creep resistance to be enhanced by very low bond strength (though a low to moderate bond strength could be advantageous in some circumstances). Accordingly, the reinforcement-matrix bond strength will be a variable of considerable interest in the performance of intermetallic matrix composites. It will also be addressed for relatively more conventional metal matrix composites, though in that case the expectation is that a strong bond will be beneficial.

With appropriate metal and intermetallic matrix composite material, as well as monolithic matrix material, becoming available for test, and the development of our high temperature testing equipment proceeding to completion, it is expected that significant amounts of data of interest will be generated in the near future. However, material acquisition problems as well as testing equipment development have slowed experimental progress to date.

CREEP RESISTANCE

'Old' Notion

Closely spaced, stable, 'hard' dispersoids

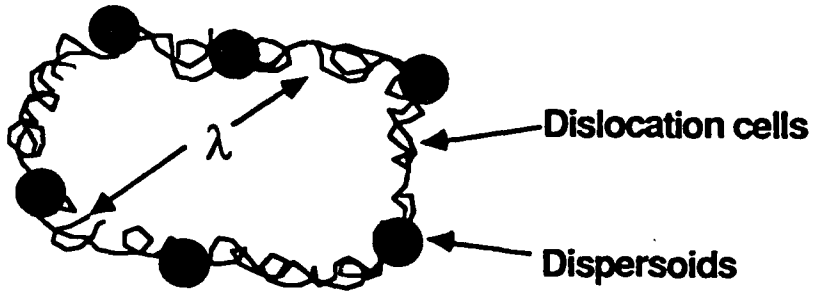

Additional Considerations

large reinforcement used to affect toughness, also to benefit creep resistance

factors:

- **shape (l/d)**
- **volume fraction**

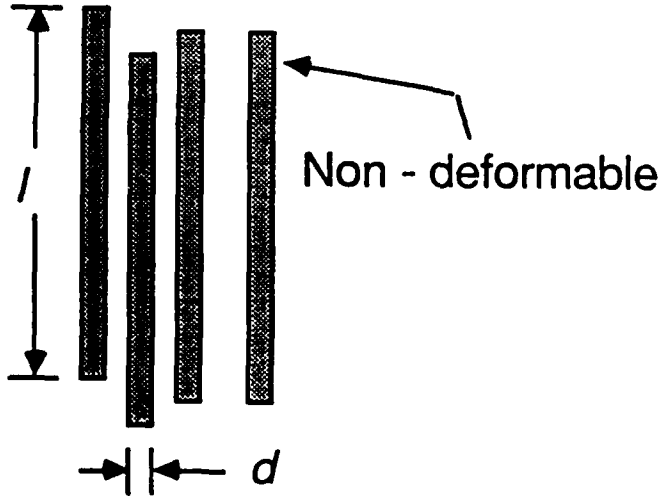

FIG. 1. Creep Resistance and Microstructure.

CREEP OF COMPOSITES

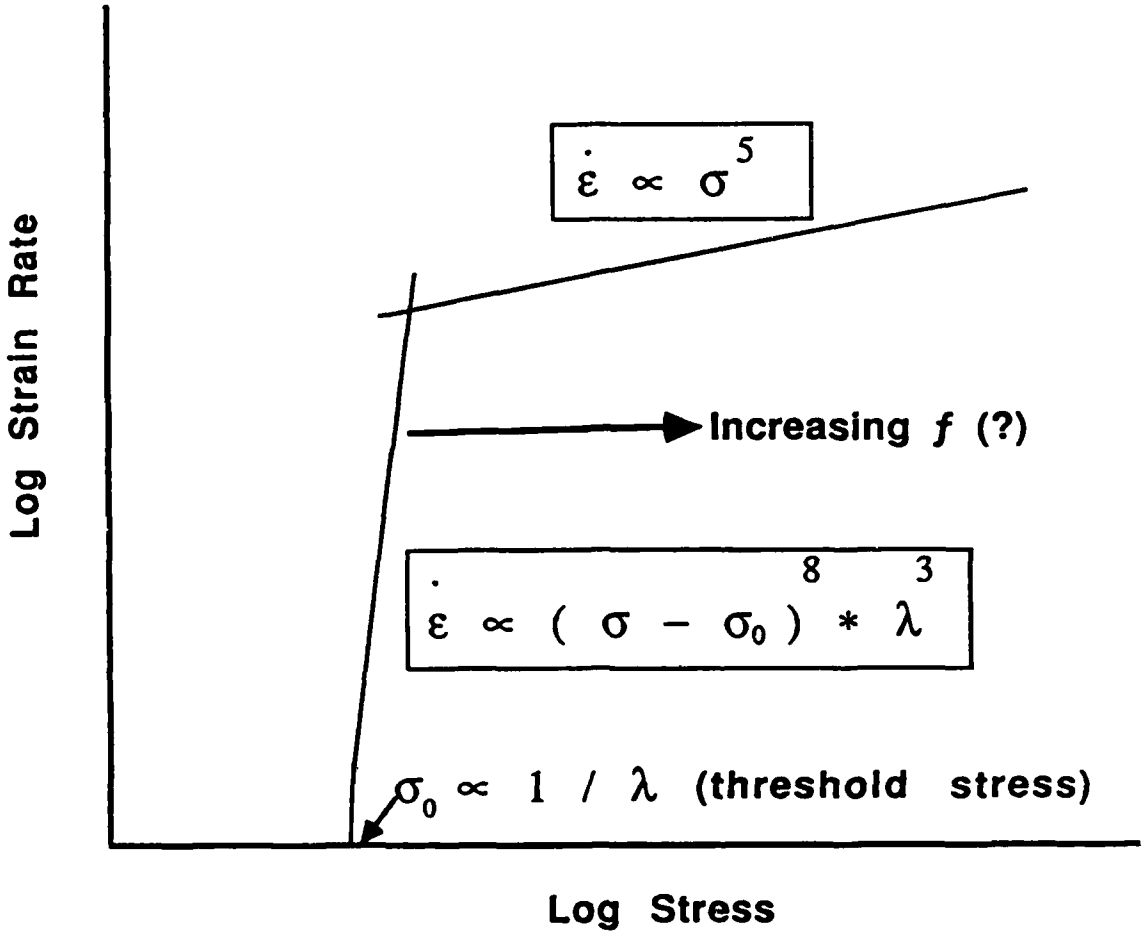

FIG. 2. Composite Creep Curve Behavior.

TOUGHNESS OF COMPOSITES

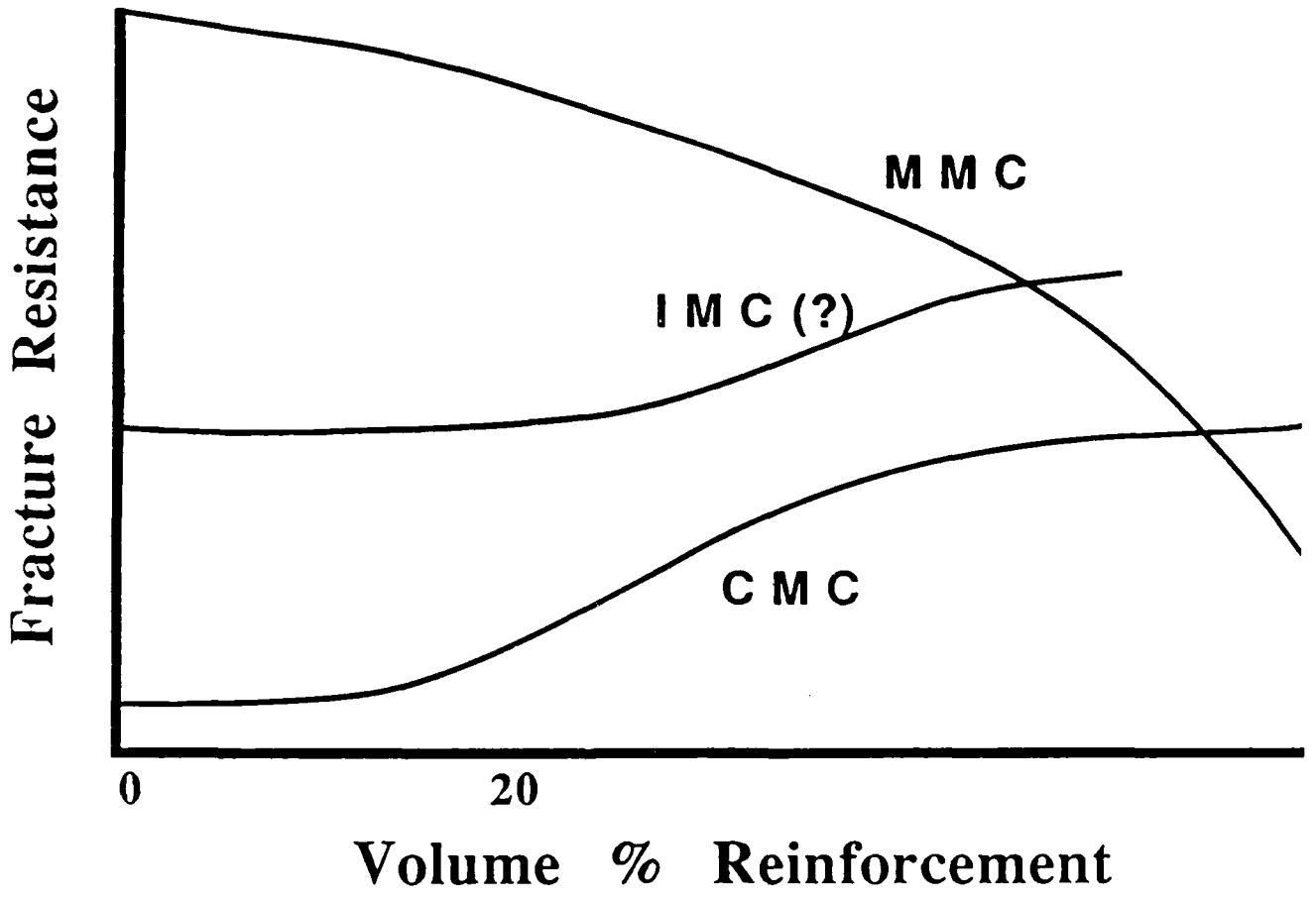

FIG. 3. Toughness Relations in Composites.

TASK 6 - W.M. Garrison

PROJECT SUMMARY

I. Introduction

The use of particles or fibers to reinforce a metal-matrix normally results in a material whose toughness and ductility are markedly inferior to those of the monolithic matrix alloy. Factors which could be of importance in determining the fracture properties of particle reinforced metal matrix composites include the particle volume fraction, the particle size, particle clustering, the matrix microstructure and the nature of the particle-matrix interface. Here, the particle-matrix interface includes microstructural features unique to the reaction zone around the interface, in addition to the interface itself.

To determine how the reinforcing particles influence the fracture properties of particle reinforced metal-matrix composites, two sets of experiments would be desirable. The first is to vary the particle volume fraction and the particle size in two comparable alloy systems. In one system the particles would be regarded as preexisting voids. In the other the particles would be strongly bonded to the matrix. The second set of experiments are those designed to establish the micromechanisms of the fracture process. The work reported here is a study of the micromechanisms of fracture in a SiC particle reinforced aluminium composite. The work had two goals. The first was to determine whether or not classic methods of observing and studying the fracture process could be employed with materials of limited ductility. The second was to investigate the micromechanisms of a particular material for which a specific hypothesis regarding the fracture mechanism have been advanced.

II. Fracture of SiC Reinforced Aluminium Composites

The conventional picture one has of the fracture of SiC composites is one normally envisioned in ductile fracture. First the SiC particles fracture or there is decohesion of the SiC-matrix interface. Thus by one of these two mechanisms voids are initiated at the SiC particles and fracture occurs by a coalescence mechanism in which the voids initiated at the particles either grow to impingement or there is fracture of the matrix material between the voids. Most fractographs of SiC reinforced aluminium alloys are consistent with this image. However, if void

nucleation at SiC particles by matrix-particle decohesion does occur, it is not clear if the decohesion is precisely at the SiC-matrix interface. EDS studies of unfractured SiC particles on fracture surfaces have shown the surface is essentially aluminium and not SiC (1). This suggests decohesion occurs in the matrix, not at the particle-matrix interface. Further, You *et al.* (2) have studied a SiC particle-aluminium matrix composite where fracture was associated almost wholly with the fracture of the SiC particles. They suggested that for this material, fracture of the matrix preceded the fracture of the SiC particles. These results suggest that it would be premature to translate our conventional notions of ductile fracture to particle reinforced metal-matrix composites.

The purpose of this work has been to determine the micromechanisms of fracture of a particle reinforced aluminium matrix composites. Several methods have been employed and the interest includes determining whether the matrix failure precedes fracture of the SiC particles and if matrix particle decohesion is observed, does it occur *in* a manner consistent with our conventional image of void decohesion.

III. Materials and Processing

The materials investigated were supplied by ALCOA and produced by a powder process. The matrix alloy composition was 7 wt% Zn, 2 wt% Mg, 2 wt% Cu and 0.14 wt% Zr with balance aluminium. The reinforced materials contained particles of SiC of F-600 grade (average size $\cong$ 16 μm) and F-1000 (average size $\cong$ 7 μm) at volume volume fractions of 15% and 20%. The average size of the powder of the matrix alloy was about 23 μm. Thus there were five materials, a control containing no SiC and four reinforced materials.

After blending, the powders were cold compacted to approximately 75%-80% of theoretical density and subsequently degassed and vacuum hot pressed to near (i.e., 99%) theoretical density. All of the compaction processes were carried out at temperatures below the solidus temperature of the matrix. The billets were subsequently fabricated by direct extrusion to a rectangular bar of cross section 25.5 mm x 76.2 mm at an extrusion ratio of 21:1.

The as-extruded materials were subsequently solution heat treated at 526°C for 1.5 hrs and then water quenched. Samples were held in liquid nitrogen until they were aged. All material reported here was aged at 160°C for 8 hours. This corresponds to the peak hardness at this aging temperature.

IV. Mechanical properties

The tensile properties of the five alloys considered are summarized in Table I. The samples used to obtain these data were smooth axisymmetric tensile specimens of gage diameter and length of 0.25" and 1" respectively. The initial strain rate was .008/min. In all cases the yield strengths and ultimate tensile strengths of the reinforced materials were about 12 and 7 ksi less, respectively, than those of the monolithic matrix alloy. The reduction of areas of the reinforced materials were 4 to 5% as opposed to 33.3% for the unreinforced matrix alloy.

V. Microstructure

The extruded alloys were examined by light microscopy, both transverse to and parallel to the extrusion direction (Fig. 1). The sections parallel to the rolling direction indicate substantial banding with long regions essentially free of SiC particles. The same section, at higher magnification indicates that the matrix grain size is about 5-10 μm. However the grains do not appear to be randomly oriented. Rather, the grain structure is suggestive of long narrow grains aligned in the extrusion direction which have been divided along their length into small grains. Thus long continuous interfaces parallel to the extrusion direction appear to be inherent to the microstructure. The tendency for the segregation of SiC particles and the occurence of regions devoid of SiC particles is less apparent in the transverse section.

The materials contain particles in addition to the SiC reinforcement. These include inclusions such as that shown in Fig. 2. Various types of inclusions were observed. The elements most commonly observed in the inclusions were Fe, Mg, Si, Cu and Zn. Inclusions most commonly reported for the matrix system are Al_7Cu_2Fe and Mg_2Si. In addition there are dispersoids and precipitates. The dispersoids were about .1 μm in size and contained Mg and Si or Cu and Zn. They are often

observed at grain boundaries as shown in Fig. 3. Precipitation on aging resulted in additional particles at the grain boundaries, slightly smaller particles within the matrix and a precipitate free zone adjacent to the grain boundaries (Fig. 3).

VI. Fractography

Fractographs of the tensile fractures of the control material are shown in Fig. 4. The fractures are characterized by long parallel striations in the plane of fracture. The tensile specimen was of the transverse longitudinal orientation. Therefore these striations are parallel to the extrusion direction and are parallel to the "elongated grains" seen in the micrograph in Fig. 1. At higher magnification, these striations correspond to relatively featureless planar fractures (Fig. 4b). Elsewhere on the fracture surface there are regions of very fine dimples (Fig. 4c).

The fracture surface of the reinforced material differs from that of the control in that SiC particles are clearly visible on the surface (Fig. 5). Except for this, the fracture surface is similar to that of the control. The parallel striations are not as visible at low magnification but at higher magnification, as in the SEM micrograph (Fig. 5b) and the TEM micrograph of an extraction replica (Fig. 6a), they are clearly visible. Again it is believed that these striations correspond to the boundaries of the elongated grains discussed earlier. The importance of these interfaces to the fracture process is reinforced by the fracture surface of a longitudinal specimen shown in Figs. 5c and d. Here long columnar facets directed in the tensile direction (the extrusion direction) are clearly visible. Thus the fractography suggests that the boundaries associated with these elongated grains are relatively brittle. Fracture replicas show, at higher magnification, that the fractures at these interfaces are extremely flat and devoid of detail (Figs. 6c and d). Finally there are regions on the fracture surfaces of the reinforced material, as on those of the control, which are ductile in nature (Figs. 5b and 6d).

Thus the fractography suggests that the mechanisms of fracture are similar for both the control and for the matrix in the reinforced materials.

VII. Fracture Mechanisms

The SiC particles dramatically reduce the tensile ductility of the composite material. Moreover the fractures of the matrix in the composites and of the control appear to be very similar in nature. The only difference between the composites and the monolithic alloy are that the fracture surfaces of the composite contain fractured SiC particles (Fig. 7a) and an occasional SiC particle which has separated from the matrix without fracturing (Fig. 7b). The question then is how do the SiC particles influence the fracture process and reduce tensile ductility.

First, examining Fig. 8 it is clear that the site of fracture initiation for tensile specimens of the reinforced materials is most often a large SiC particle which is close to the surface. Moreover, fracture occurs just at the onset of necking. Necking leads to tensile stresses which have a maximum close to the surface. If it is accepted that the largest SiC particles are most prone to fracture (as for example Ti(C,N) particles in steel) the observed behavior is consistent with our expectations.

To complement these fractographic observations of fracture initiation and to determine how fracture propagates through the material we have attempted two different experiments. The first experiments used double notched bend specimens and double notch tensile specimens. The purpose of these specimens was to deform the specimen until fracture occurred at one of the notches. Then it was hoped that the material at the other notch would be close to fracture and cross-sectioning of this material would permit observation of the initiation of fracture. The double notch bend specimens were as shown in Fig. 9 and the specimen and the notches were of the size and geometry of the usual Charpy specimen. However, cross sections revealed no damage below the notch at which fracture did not occur. This is probably due to both the extremely low ductility of this material and the difficulty in maintaining equal loading conditions at the two notches.

The double notch tensile specimens were more successful. These specimens, schematically illustrated in Fig. 9, were axisymmetric specimens of a one inch gage section and a 1/4" gage diameter prior to machining of the notches. The centers of the two notches were 3/16" from the center of the tensile specimen. The notches

were of a .08" radius and after machining the minimum diameter at the notch was 3/16".

Results of cross-sectioning of the double notched tensile specimen are seen in Fig. 10. In Fig. 10a there is evidence of SiC particle fracture at points labelled F and decohesion at the point labelled D. Fracture through the matrix is seen connecting the three points. In Fig. 10b, fractured particles are clearly visible and the voids thus generated are seen linking up by a crack growing through the matrix. In Figure 11a is seen the cross section of a nickel plated fracture surface which has been etched. Grain boundaries are clearly visible. In Fig. 11b is an SEM image of the region just adjacent to the intact notch in a double notched tensile specimen. Here we see that fracture of the matrix has clearly preceded fracture of the SiC particles. The matrix fracture is of a pattern which is consistent with failure at grain boundaries.

The second experiment was the examination of tensile specimens deformed in the SEM. The specimens were nominally as shown as in Fig. 9. These specimens were flat tensile specimens about 1.75" long overall, 1" long in the gage and .015" thick. The width in the gage was .125" with the width at the notch .0938" and the radius of the notch .012".

Shown in Fig. 12a is the specimen prior to deformation. As shown in Fig. 12b, fracture initiated at an inclusion marked I and then propagated by going around the SiC particle next to the inclusion (marked SiC #1), through the matrix and then by fracture of the SiC particle marked #2. Also shown in Fig. 12b are two SiC particles below the fracture which were initially unbroken and have fractured. Other examples of fractured SiC particles just below the fracture surface of *in situ* specimens are shown in Figs. 13a and b. Note the intense plastic deformation in the region connecting the fractured particles in both pictures. Shown in Fig. 14a and b are a fractured inclusion and the decohesion of a SiC particle from the matrix, both occurring prior to visible matrix fracture. Finally, a side branch of the fracture of an *in situ* specimen is seen in Fig. 15. The matrix fracture of the fracture path in Fig. 15 seems to follow grain boundaries. The crack advance is also associated with the fracture of particles and by decohesion of the SiC particle matrix interface. The

fracture associated with the SiC interface (SiC #1 in Fig. 15) follows the interface but appears to actually be through the matrix very close to the interface.

VIII. Conclusions

These results indicate that fracture initiation can take place by either the fracture of inclusions or of SiC particles or by the decohesion of grain boundaries close to SiC particles. In all cases fracture initiates close to the specimen surface, the region of highest tensile stress.

Regarding propagation the results suggest that crack advance can lead to fracture of a silicon carbide particle or the crack can move around the SiC particle through the matrix very close to the matrix particle interface. The crack moving around a SiC particle in such a fashion would on a fractograph give the appearance of classic void nucleation by decohesion. However this is not the case. First the "interfacial" fracture is not precisely at the interface. Second the "interfacial" fracture does not encompass the SiC particle.

REFERENCES

1. C.R. Crowe, R.A. Gray and D.F. Hasson, in *Proceedings of the Fifth International Conference on Composite Materials* (ICCMV), eds. H.C. Harrigan, Jr., J. Strife, A.K. Dhingra, The Metallurgical Society, Warrendale, PA, 843-866 (1986).

2. C.P. You, A.W. Thompson and I.M. Bernstein, *Scripta Met.* **21**, 181-185 (1987).

TABLE I

TENSILE PROPERTIES

Material	yield strength (ksi)	ultimate tensile strength (ksi)	reduction in area (%)
control (f = 0)	83.5	86.5	33.3
f = .15 R_0 = 7μm	71.8	78.8	4.3
f = .15 R_0 = 16μm	74.9	80.3	5.3
f = .20 R_0 = 7μm	69.5	77.7	3.6
f = .20 R_0 = 16μm	72.8	78.4	4.7

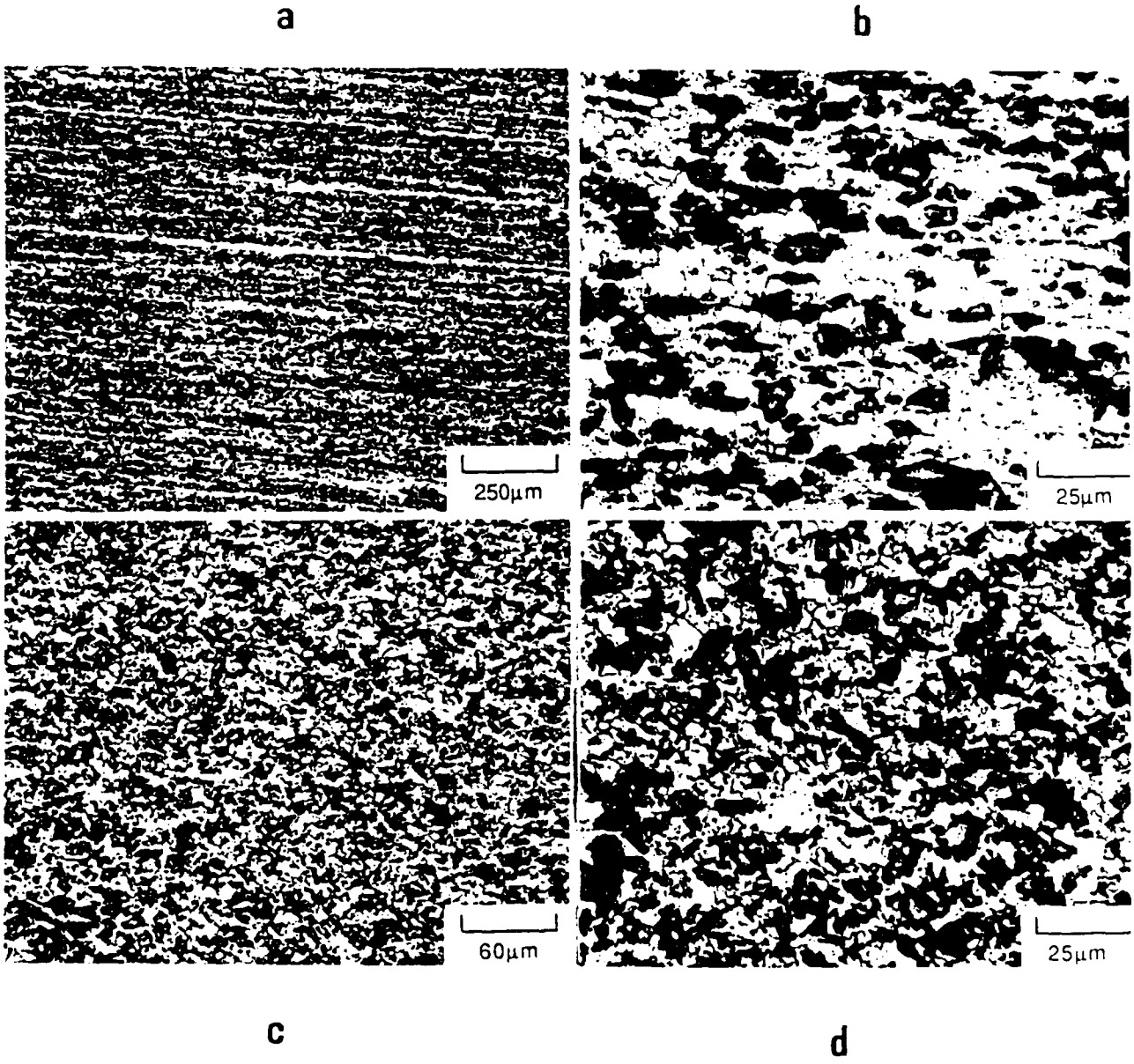

Fig. 1. Optical micrographs of the reinforced material containing 20 vol.% of 7μm SiC particles. The micrographs in a and b are of planes parallel to the extrusion direction. The micrographs in c and d are perpendicular to the extrusion direction.

Fig. 2. An SEM micrograph of a typical inclusion. This inclusion was rich in Al, Cu and Fe.

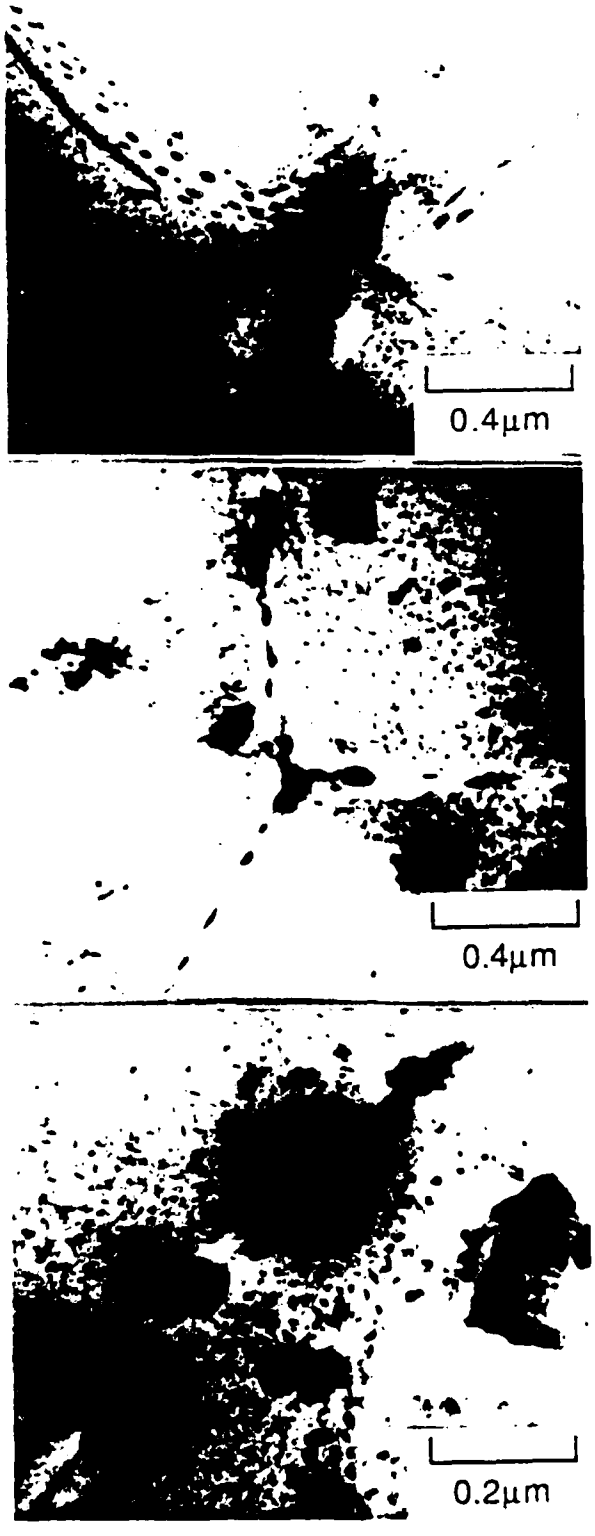

Fig. 3. TEM bright fields showing precipitates within the matrix and at grain boundaries, a precipitate-free zone and dispersoids at the grain boundaries.

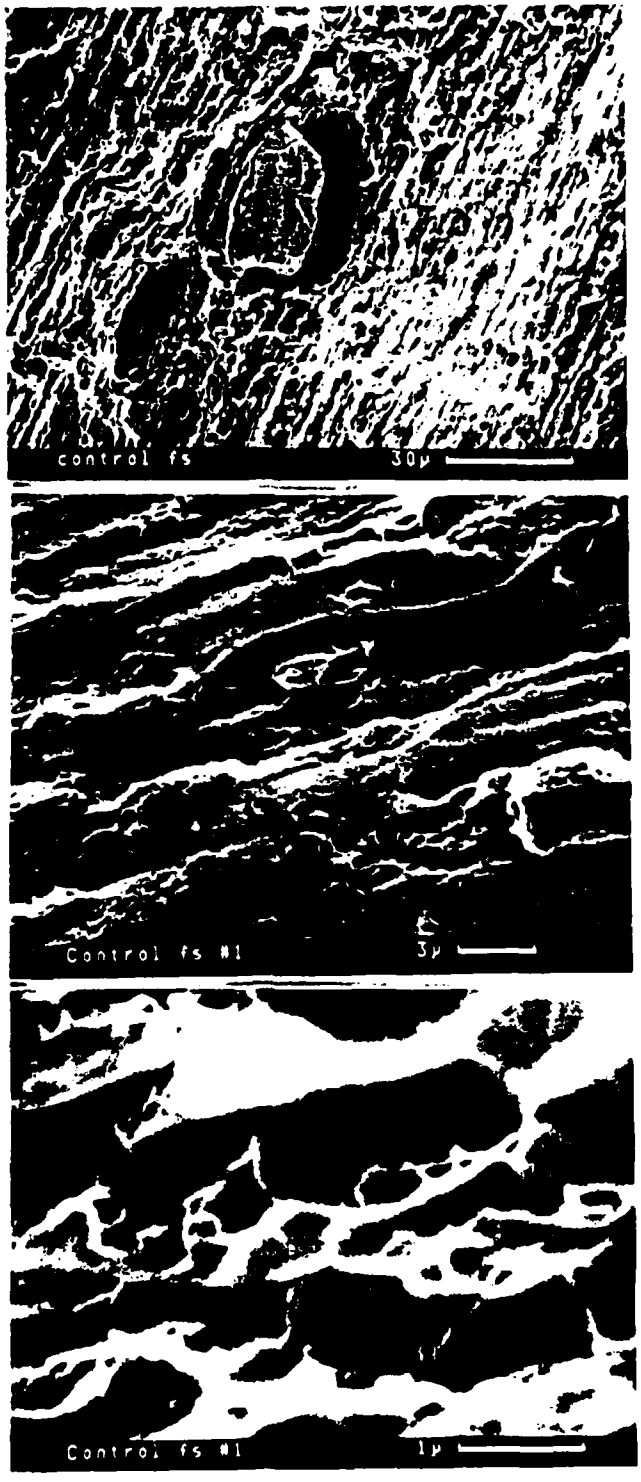

Fig. 4. SEM fractographs of tensile fractures of the monolithic base alloy.

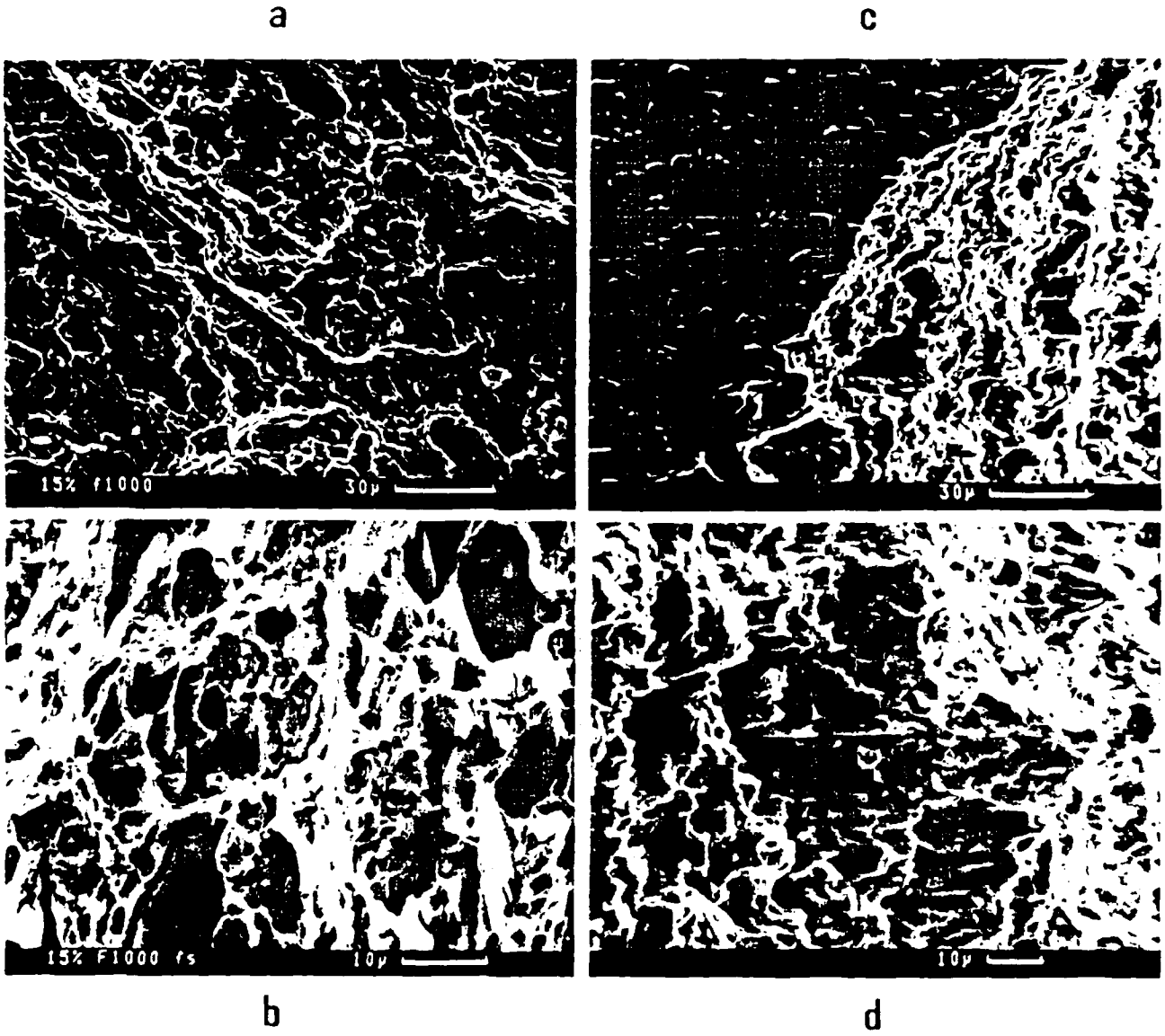

Fig. 5. SEM fractographs of the reinforced material contain 15 vol.% of 7μm SiC particles. Figures a and b are of fractures of transverse tensile specimens. Figures c and d are fractures of longitudinal tensile specimens.

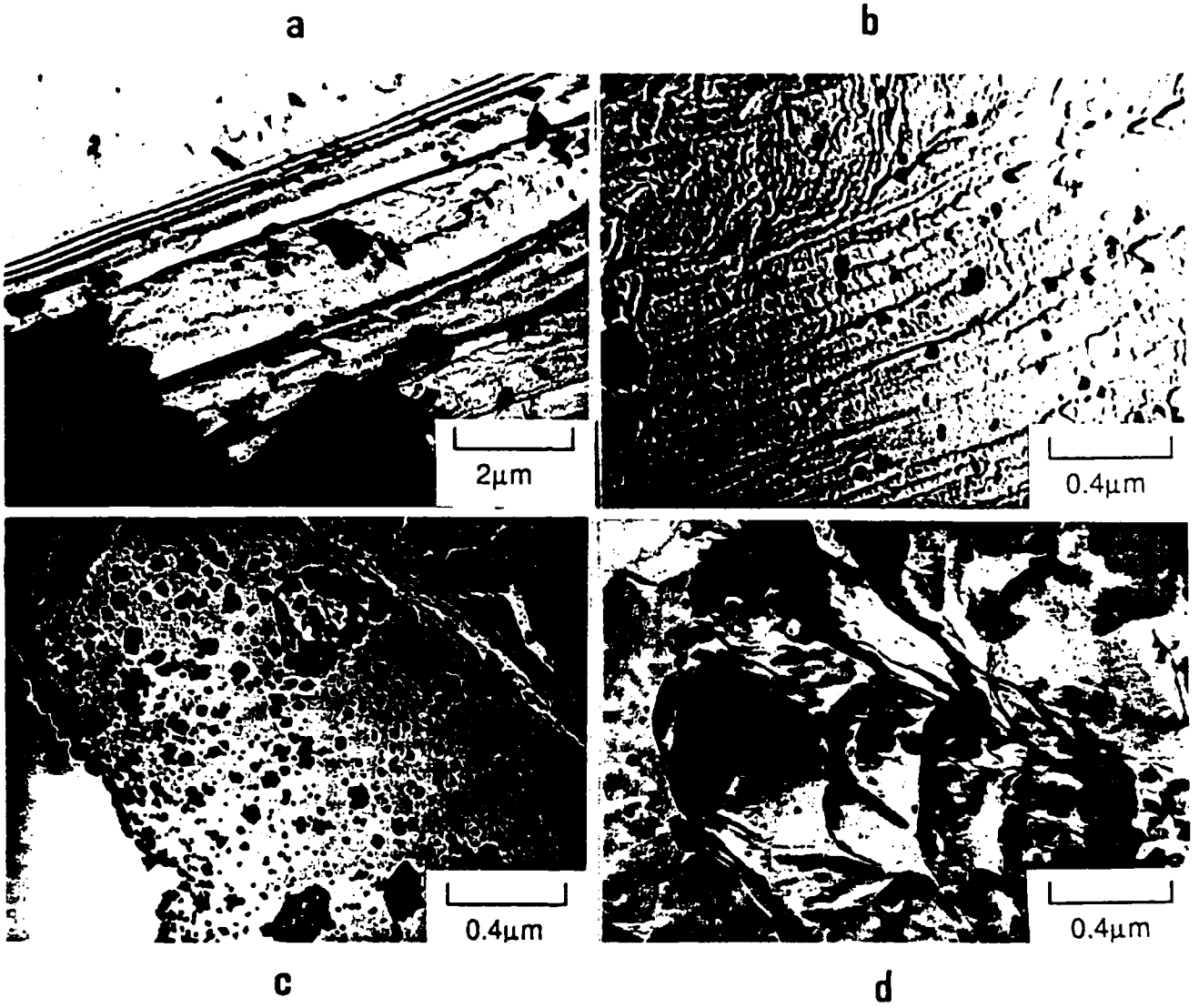

Fig. 6. TEM extraction replicas of fracture surfaces of tensile specimens of the reinforced material containing 20 vol.% 7μm SiC particles.

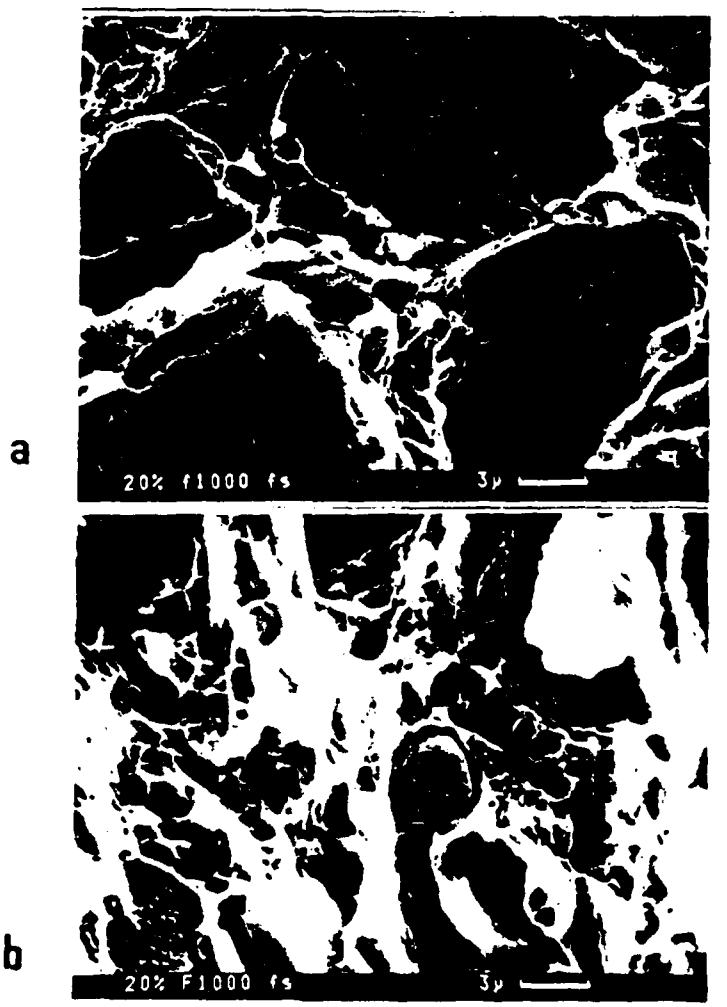

Fig. 7. SEM fractographs of the tensile fractures of the reinforced material containing 20 vol.% 7μm SiC particles.

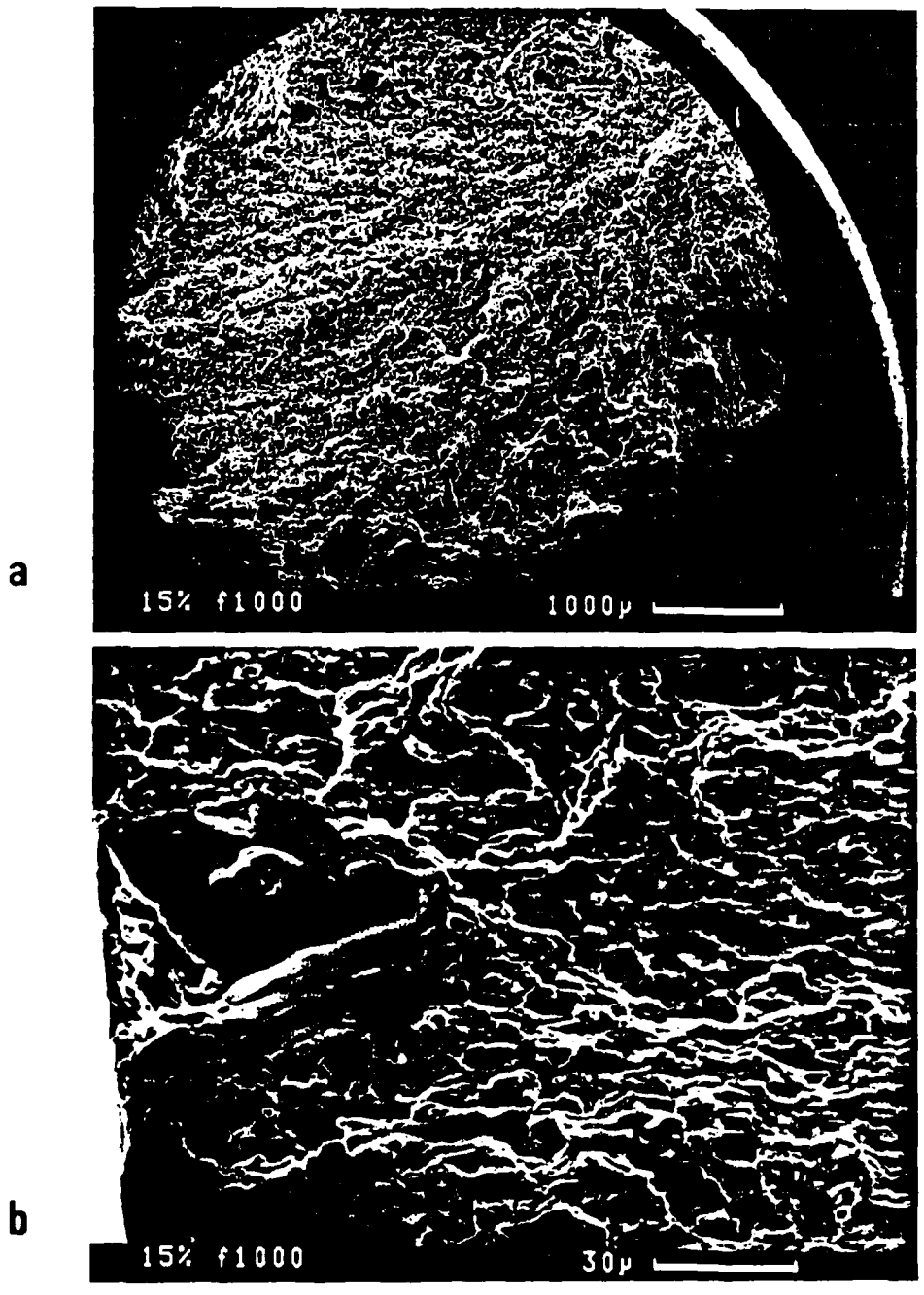

Fig. 8. SEM fractographs of a tensile fracture of the reinforced material containing 15 vol.% 7μm SiC particles. Fig. 8b shows the fracture initiation site (marked I in Fig. 8a) at higher magnification.

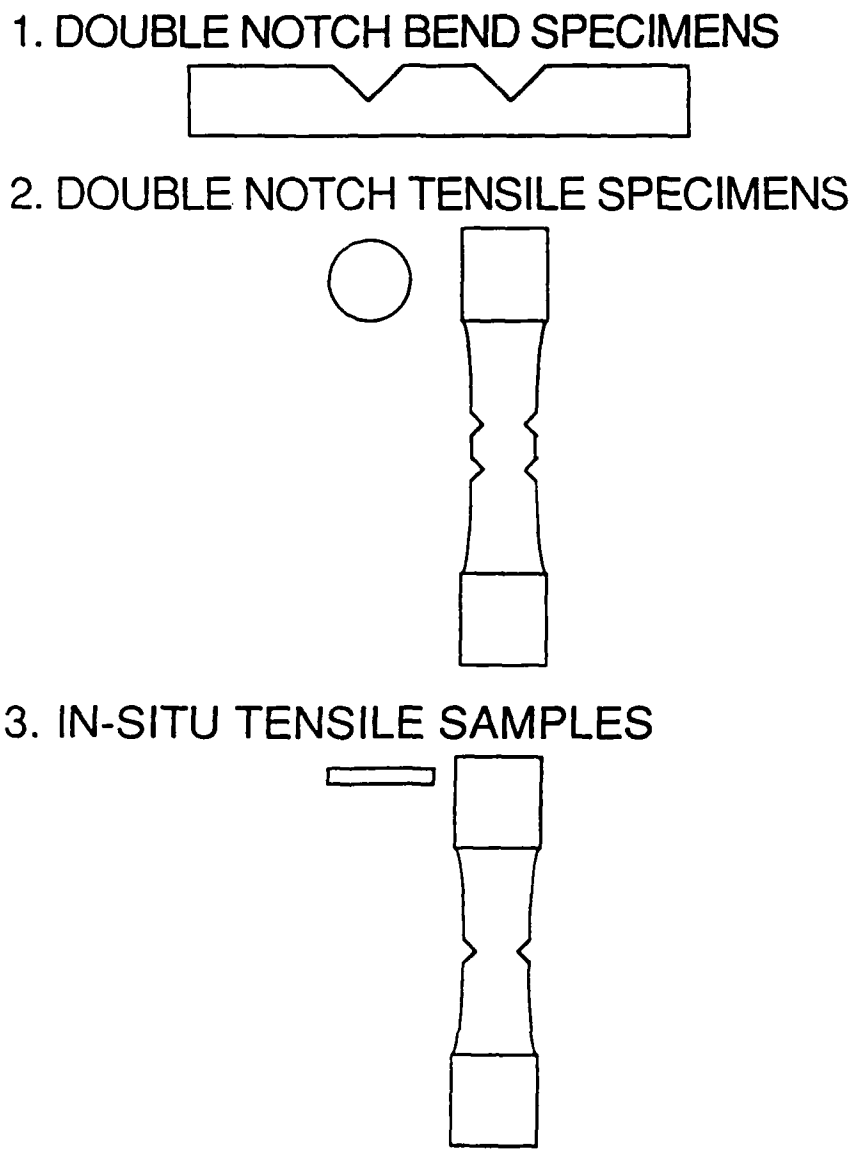

Fig. 9. A schematic of the three specimens used to study fracture initiation.

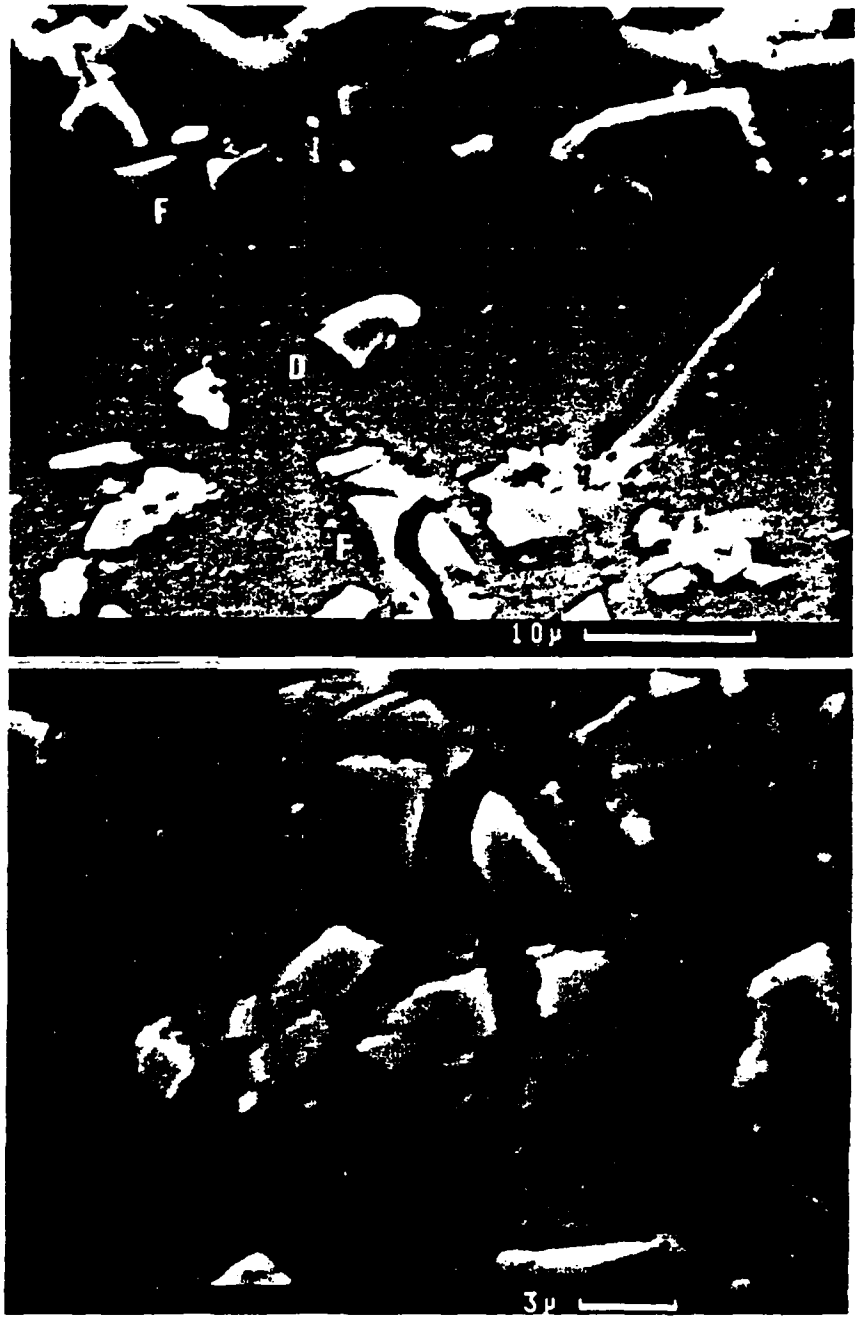

Fig. 10. SEM micrographs of a double notched tensile specimen of the reinforced material containing 20 vol.% 7μm SiC particles. The notch is at the top in both pictures.

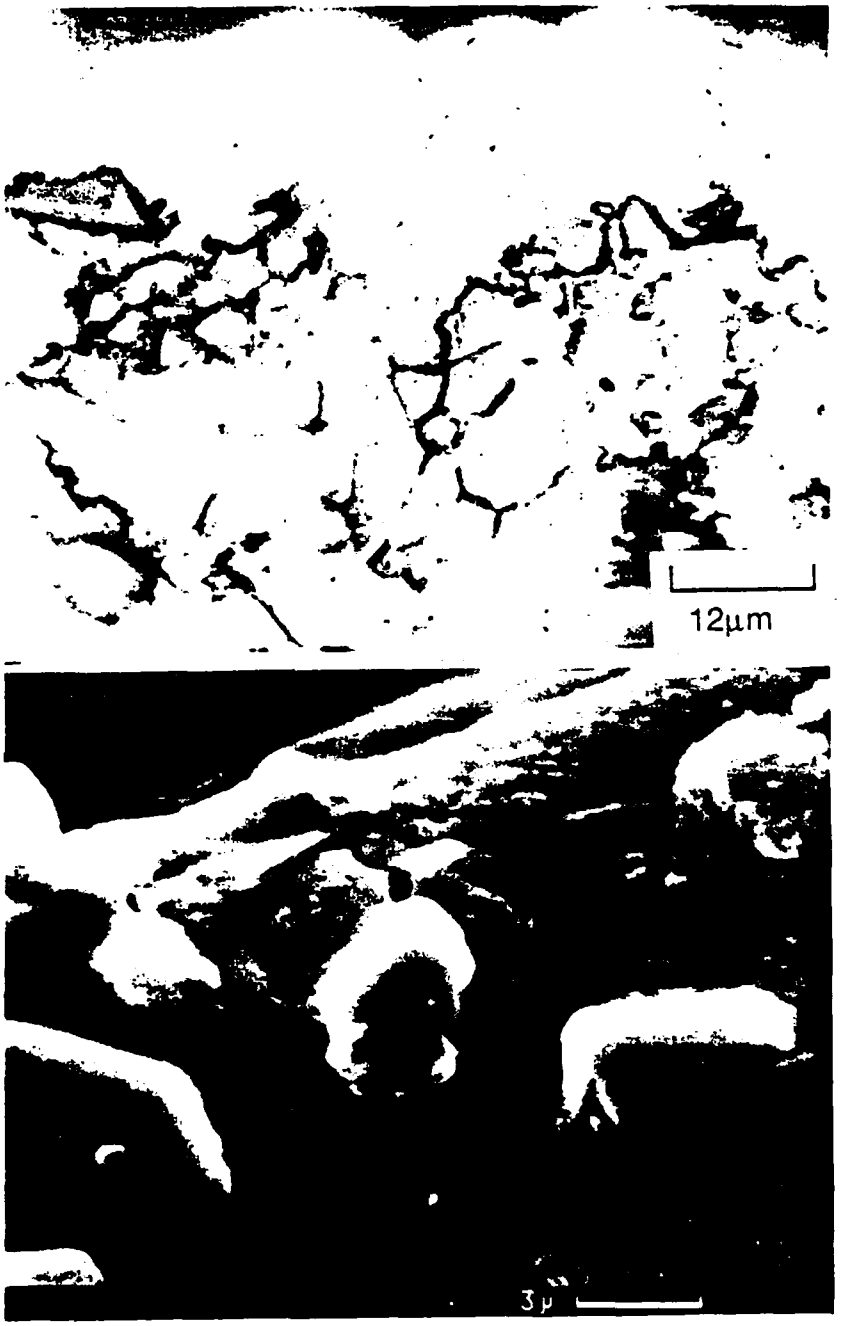

Fig. 11. SEM micrographs of (a) the cross section of a nickel plated fracture surface and (b) a double notched tensile specimen. The material for both was reinforced by 20 vol.% 7μm SiC particles.

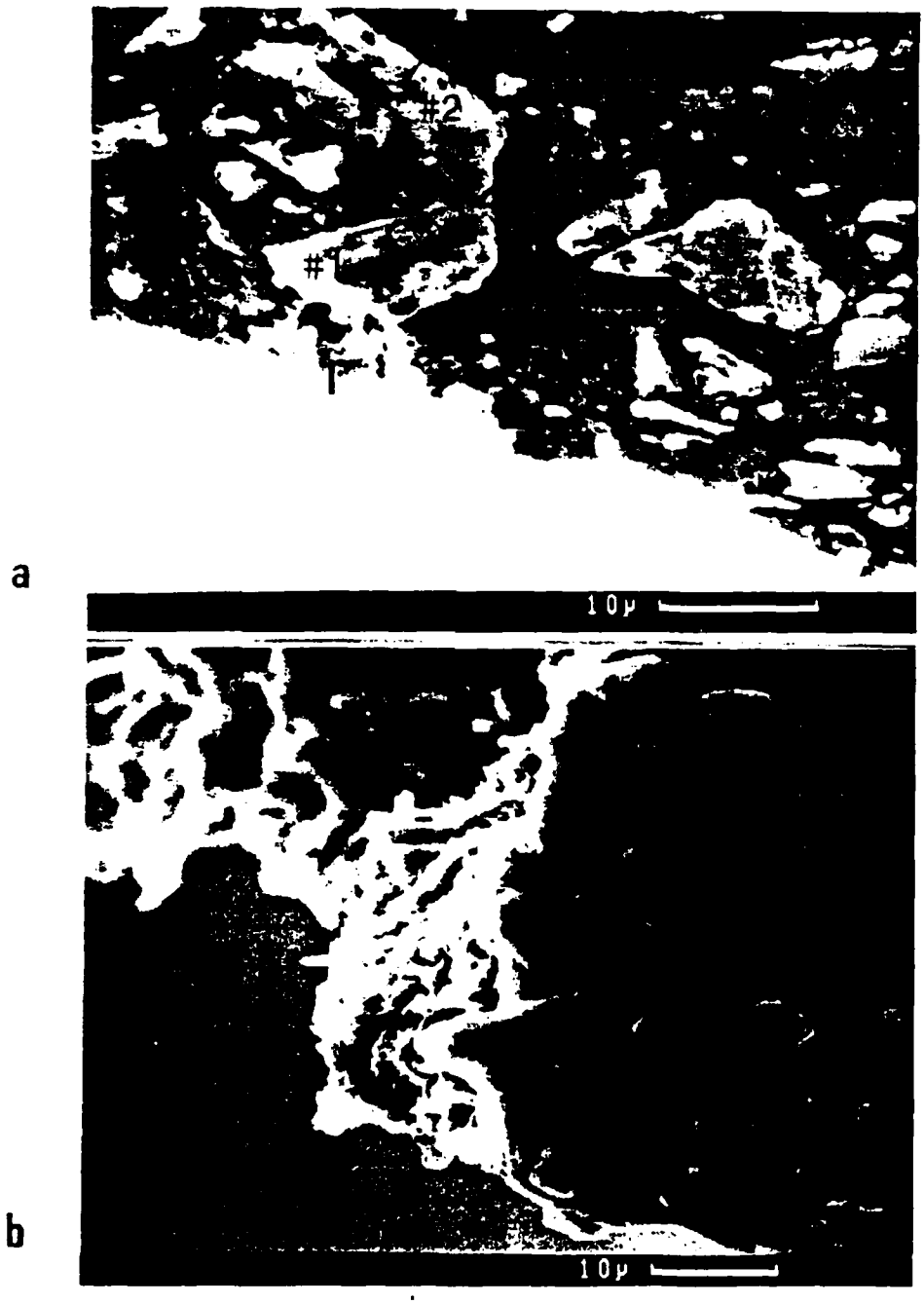

Fig. 12. SEM micrographs of an *in-situ* tensile specimen of the 20 vol.% 7μm SiC material before (a) and after (b) fracture.

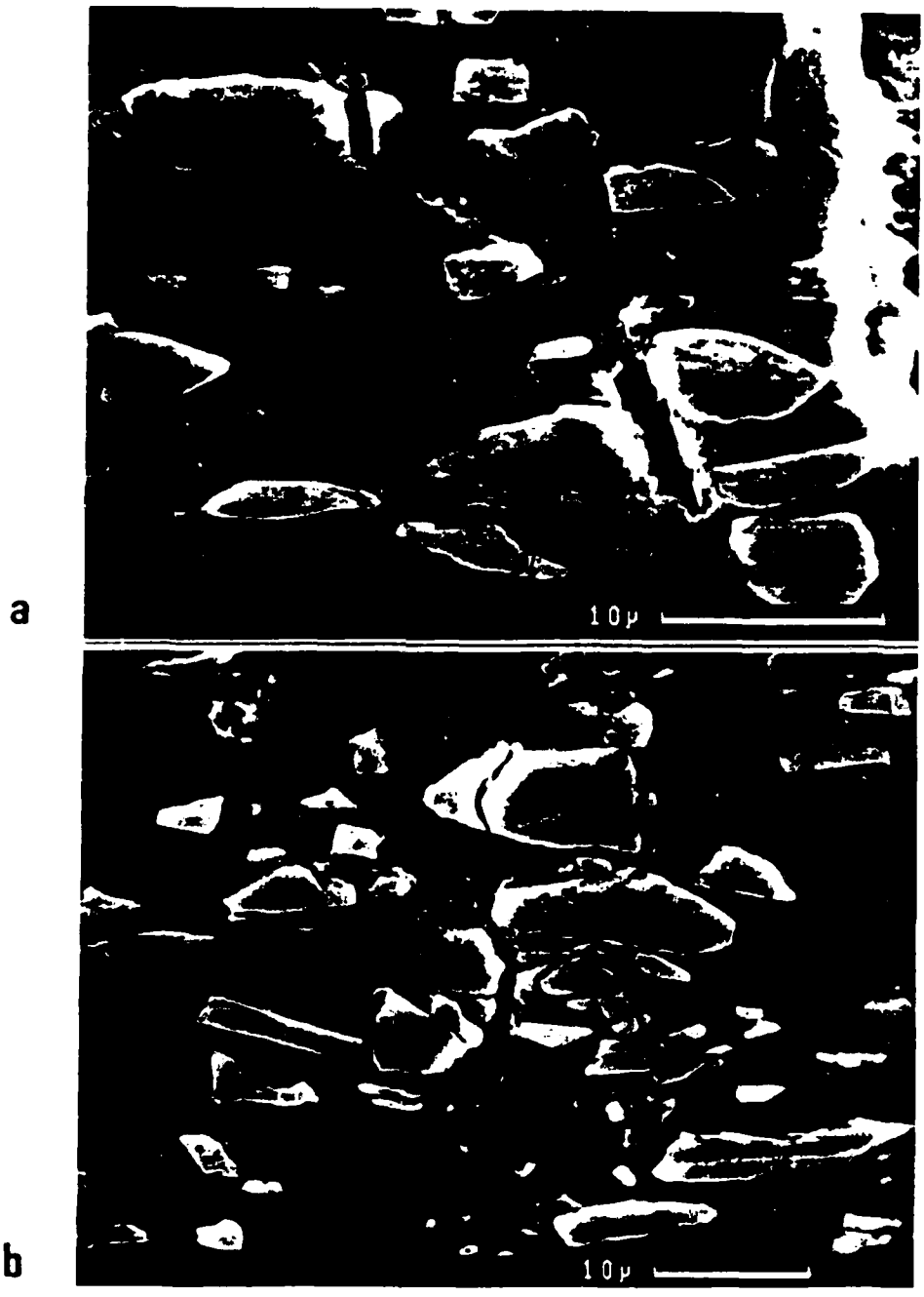

Fig. 13. Damage just below the fracture surface of an *in-situ* tensile specimen of the reinforced material containing 20 vol.% 7μm SiC particles.

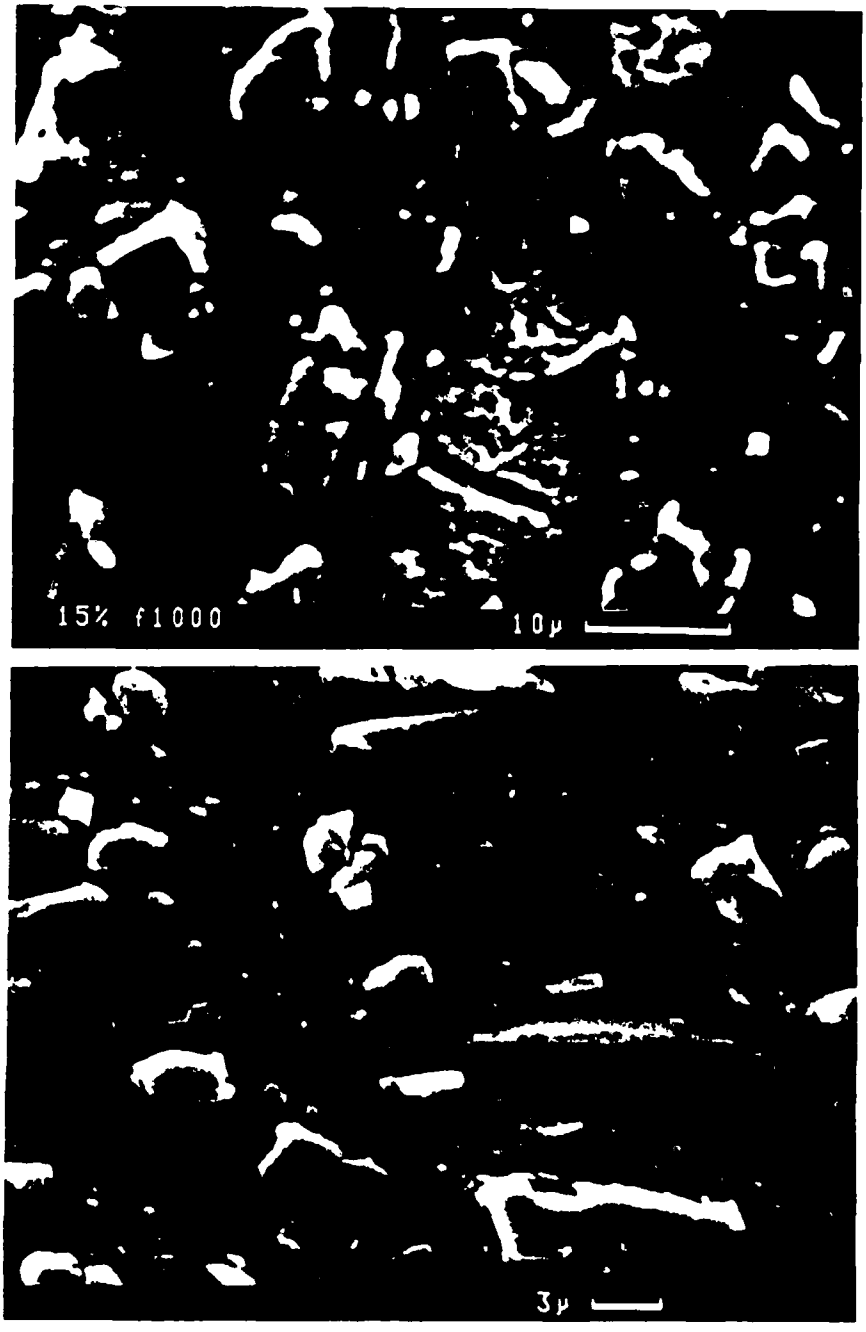

Fig. 14. SEM micrographs of damage prior to fracture of an *in-situ* tensile specimen of the reinforced material containing 16 vol.% 7μm SiC particles.

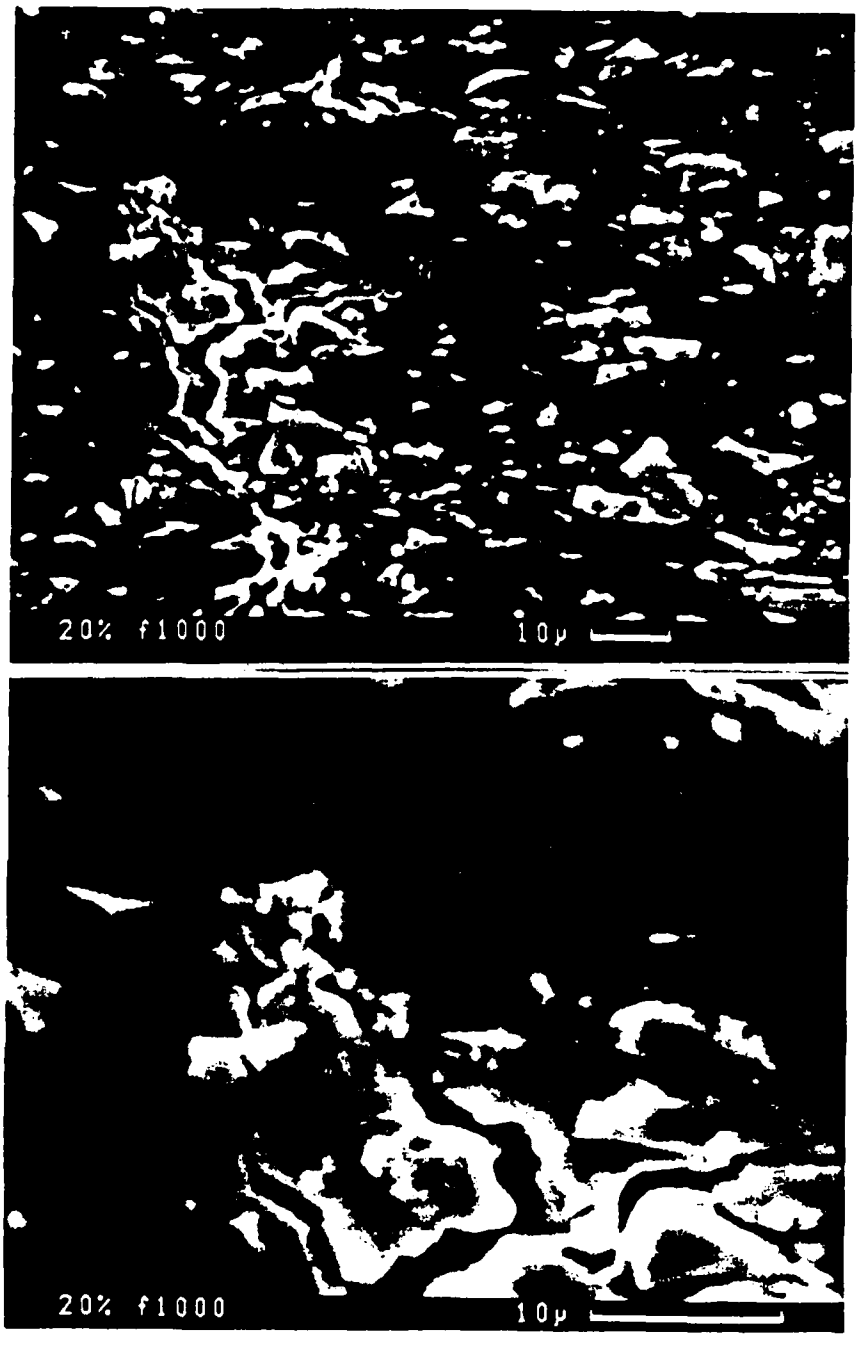

Fig. 15. A secondary crack associated with the fracture of an *in-situ* tensile specimen of a reinforced material containing 15 vol.% 7μm SiC particles.

END
DATE
FILMED
3-88
DTIC